STUDY OF ORDERED MACROPOROUS POLYMER FILMS BY TEMPLATING BREATH FIGURES

A Thesis
Presented to
The Academic Faculty

By

Lulu Song

In Partial Fulfillment
Of the Requirements for the Degree
Doctor of Philosophy in the
School of Polymer, Textile and Fiber Engineering

Georgia Institute of Technology
January 2005

STUDY OF ORDERED MACROPOROUS POLYMER FILMS BY TEMPLATING BREATH FIGURES

Approved by:

Dr. Mohan Srinivasarao, Advisor
School of Polymer, Textile & Fiber Engineering
Georgia Institute of Technology

Dr. Uwe Bunz
School of Chemistry & Biochemistry
Georgia Institute of Technology

Dr. G. Paul Neitzel
School of Mechanical Engineering
Georgia Institute of Technology

Dr. Anselm C. Griffin
School of Polymer, Textile & Fiber Engineering
Georgia Institute of Technology

Dr. Jung O. Park
School of Polymer, Textile & Fiber Engineering
Georgia Institute of Technology

Dr. David G. Bucknall
School of Polymer, Textile & Fiber Engineering
Georgia Institute of Technology

Date Approved: January 14, 2005

ACKNOWLEDGEMENTS

I wish to take this opportunity to thank all of the people who made this study a valuable experience.

First of all, this appreciation goes to my advisor, Dr. Mohan Srinivasarao. He has given me much helpful advice on my study and research. Without him, this thesis will not be possible. More importantly, in his own way, he has introduced me to the beauty of science and guided me to grow as a researcher and scientist. What I have learned during my study in his group is far more than this thesis itself, which I believe will be beneficial to me in a long way.

Secondly, I wish to thank all the other committee members: Dr. G. Paul Neitzel, Dr. Jung O. Park, Dr. Uwe Bunz, Dr. Anselm C. Griffin and Dr. David G. Bucknall. They are very kind to be my committee members and have given valuable suggestions on this thesis. Especially, I need to thank Dr. Uwe Bunz for providing me the lab space and several polymers which are very helpful for my research. I am very thankful to Dr. G. Paul Neitzel for the correction of my thesis proposal and the early version of this thesis, for the helpful suggestions on my research and for the introduction to fluid mechanics. I am also grateful to Dr. Jung O. Park for her helpful suggestions on my research and on using confocal microscope, and for the correction of the early version of this thesis.

Thirdly, I would like to thank all the group members. I really enjoy the time with them. I have learned many from them as well. In particular, I need to thank Dr. David Jenkins who worked as a post-doc in the group. He helped me with the apparatus set-up when I started my research.

Besides, I am very thankful to Dr. Qiang Hu and Dr. Tao Liu for their help with my research and their valuable suggestions as the seniors. Dr. Qiang Hu has given me several suggestions on my research. The discussion with him has always been encouraging. Dr. Tao Liu has always been a kind person to go to when I have trouble. He has helped me with the programming language for the orientational-correlation-function calculation and with the infrared measurements. I am also thankful to W. Philip Watson for his help on measuring molecular weight of the polystyrenes I used in my experiments.

I own a special thank-you to Mr. Dan Dyar from Vashaw Scientific, Inc. He is a very kind gentleman. Whenever there was a problem with the polarized optical microscope in our lab, I can always get help from him.

I am indebted to my two families. One is Dr. Bor Z. Jang and his family. Without Dr. Jang's encouragement and help, I may not even start the study at Georgia Tech. During my stay in US, he and his family looked at me as their own daughter or sister. Their care and support have made my stay much easier. The other is my parents and brother in China. With time going by, I have been able to appreciate the so-many things they have given me more and more. I feel so lucky to have care and support from two families. Their care and love are the most precious things in my life, which have supported me to go through every step of the way.

Finally, I thank NSF, DARPA and PRF for financial support.

TABLE OF CONTENTS

LIST OF TABLES

LIST OF FIGURES

SUMMARY

Macroporous films with highly ordered pore patterns have many potential applications. Some examples include microstructured electrode surfaces, photonic band gap materials and filters for cell sorting and bio-interfaces. In this dissertation we discuss a “moist-casting” method to prepare hexagonally-ordered macroporous films with pore sizes in the range of sub-micron to several microns, where condensed water droplets (“breath figures”) work as templates. Compared with other templating methods, this one is fast and simple. Well-ordered porous films can be obtained in tens of seconds and the pore size can be easily tailored and dynamically controlled by adjusting the casting conditions. More importantly, there is no need to remove the templates; water droplets just evaporate when the casting processes are finished.

This study was carried out with the intention of characterizing the structures, understanding film-formation processes and exploring special properties and possible applications. For the structural characterization, film morphology was studied in detail by normal optical microscopy and laser scanning confocal microscopy (LSCM). Several interesting features have been revealed. Meanwhile, the degree of the order of the porous structures were characterized both in real space via Voronoi diagram and bond-orientational correlation function, and in reciprocal space via Fraunhofer diffraction pattern. To further understand the mechanism, the evaporation of the polymer solutions during the film formation was studied by monitoring their mass over time. Besides, the evolution of breath figures formed on the evaporating polymer solutions was in-situ recorded via a high-speed camera coupled to an optical microscope. Combined with the

information on the film structures obtained via LSCM, explanations for some detailed features have been attempted. Wetting property of these films was studied in some detail. The films exhibited “lotus effect”, mimicking natural non-wetting surfaces. To improve the solvent stability and mechanical properties of the macroporous films for possible applications, crosslinking of the polymer matrix was tried by heating. Crosslinked structures with hexagonal arrays of cone-like air holes were obtained, which might find use as “micron-sized beakers” for small-quantity analysis.

CHAPTER 1

INTRODUCTION AND LITERATURE REVIEW

According to IUPAC (International Union of Pure and Applied Chemistry), pores with dimensions exceeding about 50 nm are called macropores [1]. Macroporous films with highly ordered pore-patterns have received increased attention because of their potential applications in chemistry, biology, optics and electronics. One way to prepare such films is the top-down engineering techniques such as conventional photo-lithography [2] used in the semiconductor industry and “soft lithography” [3,4] for patterning organic materials.

The materials and processes of semiconductor lithography are adopted from graphic-arts industry, where printing plates are prepared via lithography [2]. The basic idea of semiconductor lithography is to first coat (generally via spin-coating) the substrate to be patterned (e.g., a silicon wafer) with a radiation-sensitive material (called a photoresist [2]), and then, through a mask with the desired pattern, expose the coated wafer to high-energy radiation such as ultraviolet (UV) light or electron beam (e-beam). Depending on the properties of the resist, either the exposed region (positive resist) or the unexposed region (negative resist) can be dissolved away [2]. Then the patterned coating serves as a stencil for structuring the underneath silicon wafer by etching. Both wet liquid etching (mainly via electro-chemical reaction) and dry plasma (gas-phase) etching have been developed [2]. Finally, the resist can be stripped from the now structured silicon wafer. Generally, the whole process needs to be repeated several times to obtain the desired structures, especially for three-dimensional (3D) ones. Besides, there are detailed

technical requirements at each step to make sure the accuracy of the final structures. For example, the mask needs to be stable (without deformation or deformation being less than the feature sizes) under high-energy radiation and the lift-off of the resist should not damage the substrate surface. Therefore, it is a tedious, complicated and expensive process to form highly-ordered macroporous films using the conventional lithographic method.

In addition to the conventional lithography, some relatively simple and technically-expedient lithography methods have been developed, especially for preparing micron- to nanometer-sized features in polymeric materials. They are sometimes called “soft lithography”, where micro-sized patterns are printed into materials. One such procedure is micromoulding via capillary action [3]. In brief, a patterned elastomeric master is placed in intimate contact with a substrate to form a continuous network of channels. Then a low-viscosity polymer precursor is brought into contact with one end of the channels which spontaneously fills the channels via capillary action. Finally the polymer precursor is crosslinked and the master is removed, leaving a patterned polymer layer [3]. Another one utilizes nanotip arrays which are fabricated on the distal faces of coherent fiber-optic bundles [4]. The array can be brought either into contact with a layer of photopolymerizable monomer and appropriate photo-radiation is directed through the optical-fiber arrays to polymerize the monomer (photoimprint lithography) or into contact with a layer of heated polystyrene (imprint lithography). In both case, the surfaces are patterned with arrays of micro-wells whose shape is the inverse of the nanotips [4]. These novel lithographic methods do have some advantages, but it is still a challenge for highly-ordered macroporous films in large areas to be prepared using such methods. Besides, it

is difficult to prepare spherical pores with the larger diameter inside the film via these methods.

Recently, bottom-up approaches using self-assembly of materials as templates have attracted much research attention because, in this way, highly-ordered macroporous films can be prepared in large areas coupled with (possibly) low cost. The self-assembled templates can be composed of colloidal particles [5-22] and emulsions [23,24], providing ordered structures with the pore size on the order of tens nanometers to tens microns. The pores prepared by these templating methods are spherical and interconnected.

Colloidal crystals consisting of close-packed, monodispersed spheres are the most widely used template to prepare three-dimensional (3D) ordered macroporous materials. Many research papers are devoted to it [5-18] and a number of review papers have appeared in the literature [19-22]. It mainly consists of four steps. First, colloidal particles are self-assembled into close-packed arrays via a method such as gravity sedimentation and solvent evaporation. The colloidal spheres used are generally made from silica, polystyrene (PS) and poly(methylmethacrylate) (PMMA). Secondly, fluid precursors of desired materials are infiltrated into the interstices among the close-packed colloidal particles. Then the precursors in the interstices are subsequently converted to solids. Finally, the templating spheres are removed by heating (i.e., calcinations) or solvent extraction. A variety of methods utilizing sol-gel processes, polymerization, salt precipitation, nanocrystal infiltration, electrochemical deposition and chemical vapor deposition have been developed to deposit desired materials into the interstitial voids in the colloidal crystals. Highly-ordered macroporous films of polymers, metal oxides or metals have been prepared using this templating method.

Similarly to the packing of colloidal particles, where solid spheres are used, liquid drops stabilized in an immiscible liquid (emulsions) have also been utilized to prepare macroporous films [23,24]. In this method, an emulsion (e.g. oil-in-formamide [23]) with nearly monodisperse droplets (which was done by fractionation [25]) is added into a sol of the desired material (e.g., a metal oxide) and then the volume fraction of the oil droplets is increased (> 50%) so that they self-assemble into a colloidal crystal. Subsquently a small amount of ammonia is added into the sol to increase the pH and induce gelation. Finally the oil template was washed away by alcohol and residual organics were removed via a heat treatment. Macroporous titania, silica and zirconia with pore size ranging from 50 nm to several microns in a large area were prepared by this method. Similarly, polymerization can be used instead of the sol-gel process to prepare macroporous polymer materials [24].

In this dissertation, we discuss a simple approach to making macroporous films with hexagonally packed arrays of spherical pores (referred to as “air bubbles” [26]). As shown in Figure 1.1, a film is prepared simply by casting a polymer solution under moist ambience. The whole process takes only tens of seconds, without the multiple steps necessary for all the methods described above. This phenomenon, first reported by Widawski et al. [27] in 1994, has attracted much attention [26-45,59,68-70], both because of its intriguing scientific nature and many potential applications. In the following section, we review the results of this “moist-casting” method reported in the literature and discuss its advantages and potential applications.

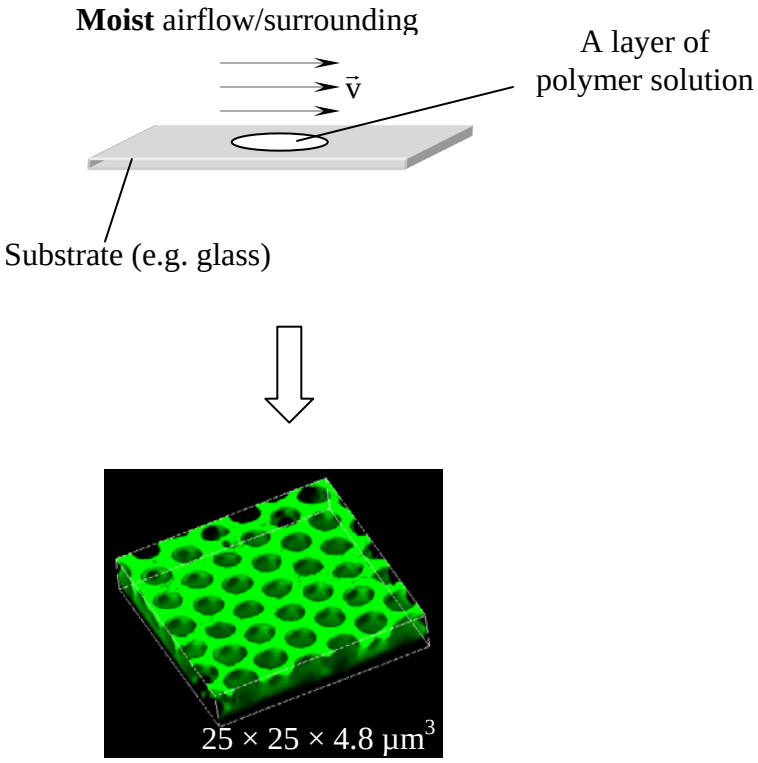

Figure 1.1 A polymer film with ordered array of pores ("air bubbles") can be made by a simple casting process: spreading a layer of dilute polymer solution (in a volatile solvent) on a substrate and letting the solvent evaporate under moisture. The air bubbles are almost uniform in size, on the order of several microns, and hexagonally packed. The polymer used here is poly[*p*-(phenylene)ethynylene]s (PPEs) with hexoxy side chains (see Figure 2.3).

1.1 Literature Review

1.1.1 Material Systems Applicable

A variety of polymers have been reported to be able to form ordered macroporous structures by this "moist" casting method with appropriate solvents. The polymers include linear homopolymers [26,28-32], rod-coil or coil-coil block copolymers [27,29,30,33-36], star-like homopolymers or copolymers [27,33,37,38], and amphiphilic polyion complexes [29,39,40]. Interestingly, most of the polymers have polystyrene as a component (see also Figure 2 in Ref. 41). In addition to polymers, a mixture of a TiO_2 precursor with a low-molar-weight amphiphile [29] and ligand-capped nanocrystals such as perfluoropolyether-thio- (PFPE-) coated gold nanocrystals [42,43] were found to be applicable to this method as well.

Generally, the solvents used in making the porous films are highly volatile and water-immiscible. The reported solvents include carbon disulfide (CS_2), benzene, toluene, chloroform, dichloromethane, 1,2-dichloroethane ($C_2H_4Cl_2$), and 1,1,2-trichlorotrifluoroethane (freon). Among them, CS_2 is the one that was most commonly used.

1.1.2 Film Morphology, Pore Sizes, and Affecting Factors

1.1.2.1 Film Morphology and Pore Sizes

The macroporous films are composed of spherical pores which are hexagonally arranged. In many cases [26-45], only two-dimensional (2D) (i.e., single-layer) arrays of pores were obtained at the film surface. Three-dimensional (3D) structures, however, composed of several layers of air-bubble sheets, can also be prepared [26,27,34,42]. The

air bubbles at the top layer generally have the larger diameter inside the film with the top open at the film surface.

Although in the same arrangement (hexagonal), the pores in a layer were found to be interconnected by some researchers, and isolated by others. Srinivasarao et al. [26] found their air bubbles in the polystyrene films to be open by back-filling the structures with a liquid and by Scanning Electron Microscopy (SEM) [26]. Similarly, by SEM, de Boer et al. [33] found the spherical cavities in their poly(2,5-dioctyloxy-*p*-phenylene vinylene)-*b*-polystyrene films were mutually connected. However, the SEM image of a single-layer macroporous film (made of a polystyrene-*b*-isoprene block copolymer) by Hayakawa and Horiuchi [34] showed that the empty spheres were separated by a thin wall of thickness less than 100 nm. Also, the macroporous films (polystyrene with Cadmium-Selenium nanoparticles) by Böker et al. [28] showed isolated pores under a Transmission Electron Microscope (TEM). The different results by different researchers are probably because of different material systems and preparation conditions used.

Different pore sizes from 0.2 to 20 μm in diameter have been reported in the literature [26-45]. One must be careful when referring to the reported values because two measurements have been used to represent the pore diameter. One is the diameter of the top opening of the pores [29,39,42-44], and the other is the maximum diameter (which is below the film surfaces) of the pores [26-28,30-35,41,45].

1.1.2.2 Factors Affecting Film Morphology and Pore Sizes

In summary, two factors have been found to affect the formation of the hexagonally packed, macroporous morphology. One is casting conditions, including solution concentration; the other is the nature of material systems.

Casting conditions such as humidity and airflow speeds have effects on the size of the air pores and the morphology of the cast films. Generally, increased humidity and reduced airflow lead to large air bubbles [30,39,41]. It was found that the relative humidity in the casting chamber had to be larger than 25% [30] or even 50% [29,39] to prepare porous films. A featureless film devoid of air pores was obtained when cast under dry atmosphere [26-30]. It was reported that increasing the airflow speed from 30 m/min to 300 m/min led to decreasing pore size from 6 μm to 0.5 μm [26]. Also, the pore size can be adjusted by changing the concentration of the prepared polymer solutions. Generally, the solutions should be dilute [26-45], and lowering the concentration led to larger pores [39]. When the concentration was too low, however, irregular patterns were obtained [39].

One argument about the nature of the polymer and solvent systems is that the polymer has to be star-like or to form star-like micelles in solution [27,35,45], e.g. polystyrene-polyparaphenylene (PS-PPP) block copolymer in CS_2 [27]. In their experiments, Widawski et al. [27] found that the morphology was affected by the length of polystyrene sequences in PS-PPP copolymer, or the length of polystyrene arms in star-like polystyrene (star-PS). They observed regular morphologies when the relative molecular mass (M_r) of the polymers was between 1,500 and 50,000. The size of the pores was found to increase with M_r. If the value of M_r was further increased, the

regularity of the pore arrays decreased and finally disappeared [27]. Also, it was found [35] that the pore size of a film made of a polystyrene star with a lower molecular weight was less influenced by the concentration variation than that of a star-PS with a higher molecular weight. Not only was the molecular weight found to affect the morphology of the porous films, the number of arms and the nature of end groups of star-shaped PS were also found [27,38] to have an effect. Widawski et al. [27] found that the structure regularity increased with the number of arms. In addition, the pore size was found [38] to decrease from 750 nm to 450 nm by changing the end groups. Furthermore, porous films with very small pores (250 nm) were prepared when the number of arms was increased [38].

Another argument about the nature of the polymer and solvent system is that the interfacial activity of the polymer at the water/polymer-solution interface dictates the stability and the dimension of the pattern [30]. Mourran et al. [30] measured the interfacial activity by the pendant droplet method and found the pattern morphology was directly related to the variation of the interfacial tension ($\Delta\gamma = \gamma_{water/solvent} - \gamma_{water/(polymer + solvent)}$). For example, their measurements [30] showed that a P(MMA-co-$(HFPO)_3$MA) solution, with 1, 1, 2-trichlorotrifluoroethane (freon) as a solvent, had a much larger $\Delta\gamma$ value (14 mN/m) than a solution with dichloromethane as a solvent ($\Delta\gamma$ = 1 mN/m). When the two solvents were used to prepare macro-porous P(MMA-co-$(HFPO)_3$MA) films, the P(MMA-co-$(HFPO)_3$MA)-in-freon solution gave films with regular arrays of air pores, while the dichloromethane solution did not.

Whether 2D or 3D air-bubble arrays can form was found [26] to be dictated by the density of the solvents. Three-dimensional networks formed when benzene or toluene

was used, which is less dense than water; whereas only 2D structure was obtained when CS_2 was the solvent, which is denser than water [26]. Also, it was reported [27] that experimental conditions (i.e., the solution thickness and concentration) had effects on the formation of one or several layers of air-bubble arrays. For their polymer/solvent system, Hayakawa and Horiuchi [34] found that the macroporous structures changed from a single layer of pores open on both sides to multiple layers ordered in three-dimensions when the solution concentration changed from 0.1 wt. % to 1.0 wt. %.

1.1.3 Mechanism of the Film Formation

Widawski et al. [27] first obtained the macroporous, honeycomb-like films (with the pore size two- or three- orders larger than the molecule size) when preparing PS-PPP block copolymer films from CS_2 for radiation scattering experiments. At first, from their experimental results, they related the film formation to the classical "phase inversion" process [27], which is normally used in producing porous polymer membranes, and suggested that a gelation process of PS in CS_2 may play a role [27]. However, as François et al. pointed out later [35], in a "phase inversion" process [46], a non-solvent diffused into a polymer solution (generally concentrated) to induce a phase separation, while in the current film formation process the solvent was water-immiscible so that the non-solvent cannot diffuse into the polymer solution and the concentration of the polymer solution was generally low. Also, their later sol/gel temperature measurements [45] revealed that the thresholds of polymer concentrations at which gelation processes started were not very different between solutions producing well-structured films and those producing disordered films. In particular, the finding of another solvent, 1,2-

dichloroethane ($C_2H_4Cl_2$), in which no gel phase had been observed, suggested that gelation may not play any role in the film formation process [45].

Now an outline about how the ordered structures form has been established, although some details are still not clear.

1.1.3.1 How Do the Spherical Cavities (or Air Bubbles) Arise?

Several experimental facts have shown that the air pores in a macroporous film result from condensed water droplets on the solution surface, due to the evaporative-cooling of the volatile solvent; these water droplets are then trapped in the polymer matrix after most of the solvent evaporates, and finally the residual solvent and condensed water droplets evaporate when the temperature of the film returns to the surrounding temperature [26,28-34,36,38-45].

One of the experimental facts was the direct observation of the formation of the porous films under an optical microscope. The water droplets were seen to condense quickly on the surface of the polymer solutions and form the same patterns as found in the films [26,29,45]. Secondly, the temperature of the evaporating solution surface was measured to be near 0 °C [26], or even less (around –6 °C [33]). For an airflow at room temperature (T ~ 21 °C) with relative humidity equal to 50%, the dew point is around 10 °C. Condensation of water should take place when the humid air contacts the cold surface. In addition, when films were cast under dry or low-humidity atmosphere (without water vapor or with low water-vapor content), only transparent films, devoid of macroporous structure, were formed, which was additional evidence that water was responsible for the structure formation [26-45].

1.1.3.2 Why Are the Pores Uniform in Size and Hexagonally Packed?

Since the air bubbles in the porous films are imprints of condensed water droplets, the order of an array of air pores should come from the order of the pattern of condensed water droplets.

Water condensing on a cold surface is commonly observed and the detailed mechanisms of the condensation and pattern formation are important for many scientific and industrial activities [47]. Depending on the wetting properties of the surface, a film or drop of water forms [47]. Under partial wetting conditions, the condensed water droplets form patterns, which are historically called “Breath Figures” [47-58]. Studies of breath figures on solid substrates have been carried out as early as 1911 by Rayleigh [48,49] and Aitken [50]. Baker [51], and, more recently, Beysens, Knobler et al. [47,52-55], and Briscoe and Galvin [56,57] have continued this research. It was found that, at the very early stage of the condensation process, the water droplets were isolated, and grew as a function of time, without interaction. Later, when the size of droplets increased so that some of them contacted each other, coalescence took place and dominated, leading to an essentially constant polydispersity in the droplet size [47,52,53].

Beysens, Knobler and co-workers [47,53-55], have also performed some experiments in which droplets of water were condensed onto the surface of a non-volatile liquid (paraffin oil). In contrast to droplets on solid surfaces, two water droplets on oil did not coalesce immediately when they touched each other. Rather, they interacted as though they were hard spheres [47,53-55]. That is because they were separated by a thin film of oil. Coalescence occurred only after the oil film in between had been depleted, which took a relatively long time [47,53,55]. In this case, at an earlier stage before

coalescence dominated, they observed a “hexatic” phase [47,55], at which water droplets were almost in the same size and hexagonally packed, quite similar to what were seen in the ordered macroporous films.

For the breath-figure study discussed above, the substrates (solid or liquid) were all externally cooled. Following Beysens and Knobler’s work, Limaye et al. [58] examined the dynamics of breath-figure formation on volatile liquid surfaces, where the cooling of the surfaces was realized by solvent evaporation. They added a small quantity (about 5 wt. %) of polystyrene to the volatile liquids (benzene and chloroform) so that the profiles of breath figures were kept in the polymer matrices after water evaporated. For their study with benzene, they did get porous films with hexagonally packed air pores [58].

Thus, the ordered arrays of air bubbles are imprints of ordered breath figures on the volatile polymer solution surface [26,28-34,36,38-45]. Since the polymer solution provides a very uniform surface, nucleation starts simultaneously at various places across the surface [29]. As long as there is no coalescence, these droplets will grow like isolated objects, as in the first stage of breath figures forming on solid or liquid surfaces, resulting in a very uniform size of the water droplets [26,29,30,45]. Light scattering experiments performed during the formation of the ordered structures by Pitois and François [59] and Karthaus et al. [29], respectively, did show that the growth of the water droplets condensed on the surfaces of their polymer solutions was smooth and consistent with the 1/3 growth law obtained with a solid or paraffin oil as a substrate [47,52,53], indicating that no coalescence between the water droplets occurred.

About how the droplets get closely packed, several opinions exist. One is that the airflow and convection currents on the solution surfaces closely pack the water droplets into hexagonal 2D array [26,45]. Secondly, it is argued [39] that during a solvent-evaporation process, some of the condensed water droplets are dragged into the solution by convection and some float on the solution surface. With the solution drying from the edge to the center, water droplets are close packed by capillary forces generated at the solution front [39]. In addition, for the local rearrangements of the droplets, an attractive-repulsive interaction potential between contact droplets is emphasized [45] and short-range capillary forces combined with Brownian motions are suggested to erase small irregularities as well [41].

1.1.3.3 Why Do the Water Droplets Not Coalesce?

Non-coalescence is the key to the formation of the highly ordered structures with a uniform size. The reason that the water droplets do not coalesce in the film-formation processes, however, is still not clear. Several mechanisms have been proposed to explain the non-coalescence.

One is that the polymer (or ligand-coated nanocrystals) precipitates at the solution/water interfaces. This precipitation creates a solid envelope around an isolated water droplet [41-43,45]. This droplet envelope inhibits droplet-to-droplet coalescence but still allows the growth of the water droplet by further condensation. Further, this precipitation property is related to a star polymer or polymer which can form star-like micelles in solution [45]. The experiment used to support this argument is that a solid layer seemed to form at the interface of a drop of the polymer solution (PS-PPP/CS_2) in

water [45]. Contrary to PS-PPP and star-PS, usual linear PS did not precipitate at the solution/water interface. Besides, spreading experiments [45] (by depositing an one-cm^3 solution on water and measuring the area of the resulting lens) showed that the initial lens area remained unchanged in the case of linear-PS/CS_2 (C_0 = 0.02 g/cm^3, $M_{w,PS} = 10^6$), while it was increased by a factor of 6 for the PS-PPP/CS_2 solution (C_0 = 0.02 g/cm^3, $M_{w,PS\text{-}PPP}$ = 30,000-3000) and the spreading speed increased with the solution concentration. This was explained to be due to the precipitation of the PS-PPP at the solution/water interface [45].

A similar suggestion is that the polymer prevents coalescence of neighboring droplets due to its adsorption at the water-solvent interface [30]. The surface activity of the polymer at the water/solvent interface is emphasized. It is concluded that the polymer plays a role which is similar to that of the surfactant in the emulsion [30].

Another opinion is that the coalescence of water droplets is prevented either thermodynamically or kinetically [29]. In the thermodynamic case, surface-active compounds keep the water droplets from coalescing. For less-amphiphilic polymers, like PS, the coalescence is kinetically prevented by a rapid evaporation (e.g., using a highly volatile solvent) so that the solvent is totally evaporated before the coalescence starts [29].

A different explanation is proposed by Srinivasarao et al. [26]. They suggest that it is a layer of air between the neighboring water droplets that results in the non-coalescence phenomenon between the apparently contact droplets. This consideration results from noticing the temperature difference between the evaporative solution surface, which is colder due to the evaporation of the solvent, and the condensed water droplets,

which are hotter because of the phase transition of the water from the gas phase to the liquid phase. It is proposed [26] that a thermocapillary convection induced by the temperature gradient is responsible for the stabilization of the condensing water droplets on or at the polymer solution surface. And the non-coalescence between water droplets is also explained by a similar temperature gradient between the drops [26].

Non-coalescence between drops of the same liquid brought into contact can be achieved by applying a large enough temperature gradient [60]. This phenomenon has been studied in detail and successfully explained by Dell'Aversana and Neitzel [60]. Thermocapillary convection (also called thermal Marangoni convection) is bulk fluid motion driven by temperature-induced variations of surface tension [60]. For most liquids, surface tension decreases with increasing temperature. When two drops of the same liquid with a temperature difference exceeding a certain minimum value are pressed against each other in air, the induced surface motion will drive bulk fluid motion within the surrounding air as well as within the drops. Therefore, the two apparently contact drops are actually kept apart by a layer of lubricating air. Within certain range of the applied pressure, the pressure in the air film increases with the applied pressure.

In addition, Srinivasarao and co-workers [26] give another hypothesis: the vapor of the solvent escaping from the solution surface can keep the condensing water droplets apart. There is a time competition: the time the droplets are in apparent contact and the time the solvent vapor requires to flow away from the area where the droplets are in apparent contact. The two droplets will not coalesce as long as the time the droplets are in apparent contact is less than the time required for the solvent vapor to escape the interstices [26].

1.1.4 Advantages and Applications

We can see that, for the simple casting approach we discuss above, arrays of hexagonally packed water droplets (breath figures) work as templates for the formation of the honeycomb-like porous structures. This is quite a simple procedure in the sense of templating methods. First, the templates are easily prepared and removed in tens of seconds. Secondly, the size of these structures can be easily adjusted and dynamically controlled within a certain range simply by changing the cast conditions or polymer/solvent systems [26].

Many potential applications of these films have been proposed and still remain to be explored. Firstly, they can be used in many places where porous materials are required, such as light-weight materials and thermal- or acoustic-insulators. At the same time, the highly ordered nature of the pore arrays brings about many new possible applications. One is the use as photonic-band-gap materials [61,62], which have attracted much research attention recently. Another is the use in biology for cell culturing and tissue engineering and in optoelectronics such as solar cells. Moreover, as suggested by Srinivasarao et al. [26], the macroporous films can work as arrays of picoliter beakers for small-quantity and parallel analysis [63,64], can be used for optical devices such as beam-steering devices and microlens arrays [65], and to prepare porous metals. Finally, they may be of interest as catalytic surfaces and sorption media, size- or shape-selective membranes, sensors, absorbents, etc [66,67].

Several trials have been made to utilize this simple method to make suitable macroporous films for different applications. Arrays of micron-sized aluminum cups

were prepared by depositing aluminum onto the honeycomb-like film of a rod-coil polymer which has been photo-crosslinked [33]. Macroporous films made of amphiphilic copolymers containing lactose units or carboxyl groups as side-chains and polyion complexes composed of anionic polysaccharides have been used as cell adhesive sites [68]. Nishikawa et al. [69,70] are working to put them into practical applications such as artificial basal membranes for blood vessels. More recently, self-supporting films for tissue repair [44] and viscoelastic honeycomb mesh [70] for cell culturing have been made with water as the substrate. Anisotropy is introduced into the viscoelastic mesh via mechanical stretching [44]. It is also expected to obtain some anisotropic optical properties from the deformed mesh [44]. To increase the chemical and thermal stabilities, macroporous polyimide films are made by a chemical treatment of patterned polyion complex films which are prepared by this simple casting method on water [70].

1.2 Challenges

Although much work has been done on the porous films made by the simple casting method discussed above, a number of issues still remain. First, one of the reasons that the films are interesting is their highly ordered structure, so characterizing the order is indispensable, but it does not appear to have been done. Secondly, as discussed above, the details about the formation processes are still not clear. Where do the water nuclei form and how does a droplet grow? What is the decisive driving force for the close packing of isolated droplets? Most importantly, what prevents the coalescence when water droplets come into contact? Also, what is the flow pattern inside a polymer solution during the evaporation of the solvent? What is the flow pattern inside the condensed

water droplets? What is the role of the polymer and solvent during the casting process? To understand these details is very important because we can then predict the capability of polymer/solvent system to form ordered array of air bubbles under certain conditions and further design suitable materials and optimal conditions to tailor the ordered porous structure for different application.

Finally, the application of these films is largely unexplored. For a lot of purposes, it will be necessary to prepare films with high solvent stability and robust mechanical properties. So, how to engineer macroporous films to satisfy different application requirements is also an issue for the study of this kind of films.

1.3 Thesis Outline

The objective of this dissertation is to characterize the structure of the macroporous films, to obtain a better understanding the mechanism of the film-formation processes, and to explore properties and potential applications of the porous films. In Chapter 2, macroporous films were made from two kinds of polymers: i) linear polystyrenes with various end-groups; and ii) semi-conducting conjugated polymers with carbon disulfide or benzene as a solvent. The morphologies of these films were studied via optical microscopy. Using confocal microscopy, three-dimensional structures of the films were studied in detail. Many interesting features were revealed, which are helpful for conjecturing the film-formation processes. Following the morphology characterization, in Chapter 3, the degree of hexagonal order was characterized statistically in the direct space via Voronoi diagram and bond-orientational correlation function, and in the reciprocal space via Fraunhofer diffraction pattern. To further

understand the film-formation processes, during macroporous film formation, evaporation of polymer solutions was measured in Chapter 4 and growth of breath figures on the polymer solutions was *in situ* recorded via a high-speed camera in Chapter 5. The data were analyzed, combined with the morphology (i.e., final image of the breath figures) studies in Chapter 2. Several interesting phenomena were seen and explanations are attempted. Then, in Chapter 6, wetting property of the macroporous films by water was studied in some detail. Analogues were drawn between these macroporous surfaces with "lotus-effect" surfaces. To increase chemical/solvent stability and mechanical properties of the cast films, in Chapter 7, crosslinking of the polymer matrix was tried by heating and tuned structures were obtained which can be used for small quantity analysis.

References:

[1] K. S. W. Sing, D. H. Everett, R. A. W. Haul, L. Moscou, R. A. Pierotti, J. Rouquerol and T. Siemieniewska, "Reporting physisorption data for gas/solid systems with special reference to the determination of surface area and porosity", *Pure Appl. Chem.* **57**, 603 (1985).

[2] W. M. Moreau, *Semiconductor lithography: principles and materials* (Plenum, New York, 1988).

[3] E. Kim, Y. Xia and G. M. Whitesides, "Polymer microstructures formed by moulding in capillaries", *Nature* **376**, 581 (1995).

[4] T. H. Dam and P. Pantano, "Nanotip array photoimprint lithography", *Rev. Sci. Instrum.* **70**, 3982 (1999).

[5] O. D. Velev, T. A. Jede, R. F. Lobo and A. M. Lenhoff, "Porous silica via colloidal crystallization", *Nature* **389**, 447 (1997).

[6] B. T. Holland, C. F. Blanford and A. Stein, "Synthesis of macroporous minerals with highly ordered three-dimensional arrays with spheroidal voids", *Science* **281**, 538 (1998).

[7] H. Yan, C. F. Blanford, B. T. Holland, M. Parent, W. H. Smyrl and A. Stein, "A chemical synthesis of periodic macroporous NiO and metallic Ni", *Adv. Mater.* **11**, 1003 (1999).

[8] A. Blanco, E. Chomski, S. Grabtchak, M. Ibisate, S. John, S. W. Leonard, C. Lopez, F. Meseguer, H. Miguez, J. P. Mondia, G. A. Ozin, O. Toader and H. M. van Driel, "Large-scale synthesis of a silicon photonic crystal with a complete three-dimensional bandgap near 1.5 micrometres", *Nature* **405**, 437 (2000).

[9] J. E. G. J. Wijnhoven and W. L. Vos, "Preparation of photonic crystals made of air spheres in titania", *Science* **281**, 802 (1998).

[10] P. Jiang, K. S. Hwang, D. M. Mittleman, J. F. Bertone and V. L. Colvin, "Templated-directed preparation of macroporous polymers with oriented and crystalline arrays of voids", *J. Am. Chem. Soc.* **121**, 11630 (1999).

[11] Y. Ye, S. Badilescu and V. Truong, "Large-scale ordered macroporous SiO_2 thin films by a template-directed method", *Appl. Phys. Lett.* **81**, 617 (2002).

[12] F. Sun, W. Cai, Y. Li, B. Cao, F. Lu, G. Duan and L. Zhang, "Morphology control and transferability of ordered through-pore arrays based on electrodeposition and colloidal monolayers", *Adv. Mater.* **16**, 1116 (2004).

[13] Z. Zhou, X. Bao and X. S. Zhao, "Synthesis, characterization and optical properties of ordered macroporous organosilicas", *Chem. Commun.*, 1376 (2004).

[14] T. Sen, G. J. T. Tiddy, J. L. Casci and M. W. Anderson, "Synthesis and characterization of hierarchically ordered porous silica materials", *Chem. Mater.* **16**, 2044 (2004).

[15] P. V. Braun and P. Wiltzius, "Electrochemically grown photonic crystals", *Nature* **402**, 603 (1999).

[16] P. N. Bartlett, P. R. Birkin and M. A. Ghanem, "Electrochemical deposition of macroporous platinum, palladium and cobalt films using polystyrene latex sphere templates", *Chem. Commun.*, 1671 (2000).

[17] T. Sumida, Y. Wada, T. Kitamura and S. Yanagida, "Electrochemical preparation of macroporous polypyrrole films with regular arrays of interconnected voids", *Chem. Commun.*, 1613 (2000).

[18] Y. Lee, T. Kuo, C. Hsu, Y. Su and C. Chen, "Fabrication of 3D macroporous structures of II-VI and III-V semiconductors using electrochemical deposition", *Langmuir* **18**, 9942 (2002).

[19] K. M. Kulinowski, P. Jiang, H. Vaswani and V. L. Colvin, "Porous metals from colloidal templates", *Adv. Mater.* **12**, 833 (2000).

[20] Y. Xia, B. Gates, Y. Yin and Y. Lu, "Monodispersed colloidal spheres: old materials with new applications", *Adv. Mater.* **12**, 693 (2000).

[21] A. Stein and R. C. Schroden, "Colloidal crystal templating of three-dimensionally ordered macroporous solids: materials for photonics and beyond", *Curr. Opin. Solid State Mater. Sci.* **5**, 553 (2001).

[22] V. V. Guliants, M. A. Carreon and Y. S. Lin, "Ordered mesoporous and macroporous inorganic films and membranes", *J. Membr. Sci.* **235**, 53 (2004).

[23] A. Imhof and D. J. Pine, "Ordered macroporus materials by emulsion templating", *Nature* **389**, 948 (1997).

[24] A. Imhof and D. J. Pine, "Uniform macroporous ceramics and plastics by emulsion templating", *Adv. Mater.* **10**, 697 (1998).

[25] J. Bibette, "Depletion interactions and fractionated crystallization for polydisperse emulsion purification", *J. Colloid. Interface Sci.* **147**, 474 (1991).

[26] M. Srinivasarao, D. Collings, A. Philips, and S. Patel, "Three-dimensionally ordered array of air bubbles in a polymer film", *Science* **292**, 79 (2001).

[27] G. Widawski, M. Rawiso and B. François, "Self-organized honeycomb morphology of star-polymer polystyrene films", *Nature* **369**, 387 (1994).

[28] A. Böker, Y. Lin, K. Chiapperini, R. Horowitz, M. Thompson, V. Carreon, T. Xu, C. Abetz, H. Skaff, A. D. Dinsmore, T. Emrick and T. P. Russell, "Hierarchical nanoparticle assemblies formed by decorating breath figures", *Nat. Mater.* **3**, 302 (2004).

[29] O. Karthaus, N. Maruyama, X. Cieren, M. Shimomura, H. Hasegawa and T. Hashimoto, "Water-assisted formation of micrometer-size honeycomb patterns of polymers", *Langmuir* **16**, 6071 (2000).

[30] A. Mourran, S. S. Sheiko and M. Möller, "Vitrified condensation pattern in thin polymer films: New approach for micropatterning", *PMSE Proceedings of the Am. Chem. Soc.* **81**, 426 (1999).

[31] J. Peng, Y. Han, J. Fu, Y. Yang and B. Li, "Formation of regular hole pattern in polymer films", *Macromol. Chem. Phys.* **204**, 125 (2003).

[32] J. Peng, Y. Han, Y. Yang and B. Li, "The influencing factors on the macroporous formation in polymer films by water droplet templating", *Polymer* **45**, 447 (2004).

[33] B. de Boer, U. Stalmach, H. Nijland and G. Hadziioannou, "Microporous honeycomb-structured films of semiconducting block copolymers and their use as patterned templates", *Adv. Mater.* **12**, 1581 (2000).

[34] T. Hayakawa and S. Horiuchi, "From angstroms to micrometers: self-organized hierarchical structure within a polymer film", *Angew. Chem. Int. Ed.* **42**, 2285 (2003).

[35] B. François, O. Pitois and J. François, "Polymer films with a self-organized honeycomb morphology", *Adv. Mater.* **7**, 1041 (1995).

[36] X. Zhao, Q. Cai, G. Shi, Y. Shi and G. Shen, "Formation of ordered microporous films with water as templates from poly(D,L-lactic-*co*-glycolic acid) solution", *J. Appl. Polym. Sci.* **90**, 1846 (2003).

[37] B. François, Y. Ederlé and C. Mathis, "Honeycomb membranes made from $C_{60}(PS)_6$", *Synth. Met.* **103**, 2362 (1999).

[38] M. H. Stenzel-Rosenbaum, T. P. Davis, A. G. Fane and V. Chen, "Porous polymer films and honeycomb structures made by the self-organization of well-defined macromolecular structures created by living radical polymerization techniques", *Angew. Chem. Int. Ed.* **40**, 3428 (2001).

[39] N. Maruyama, T. Koito, J. Nishida, T. Sawadaishi, X, Cieren, K. Ijiro, O. Karthaus and M. Shimomura, "Mesoscopic patterns of molecular aggregates on solid substrates", *Thin Solid Films* **327-329**, 854 (1998).

[40] H. Yabu, M. Tanaka, K. Ijiro and M. Shimomura, "Preparation of honeycomb-patterned polyimide films by self-organization", *Langmuir* **19**, 6297 (2003).

[41] M. H. Stenzel, "Formation of regular honeycomb-patterned porous film by self-organization", *Aust. J. Chem.* **55**, 239 (2002).

[42] P. S. Shah, M. B. Sigman, Jr., C. A. Stowell, K. T. Lim, K. P. Johnston and B. A. Korgel, "Single-step self-organization of ordered macroporous nanocrystal thin films", *Adv. Mater.* **15**, 971 (2003).

[43] A. E. Saunders, P. S. Shah, M. B. Sigman, Jr., T. Hanrath, H. S. Hwang, K. T. Lim, K. P. Johnston and B. A. Korgel, "Inverse opal nanocrystal superlattice films", *Nano Lett.* **4**, 1943 (2004).

[44] T. Nishikawa, R. Ookura, J. Nishida, T. Sawadaishi and M. Shimomura, "Honeycomb film of an amphiphilic copolymer: fabrication and characterization", *RIKEN Review* **37**, 43 (2001).

[45] O. Pitois and B. François, “Formation of ordered micro-porous membranes”, *Eur. Phys. J. B* **8**, 225 (1999).

[46] R. E. Kesting, in *Synthetic Polymer Membranes* (Wiley, New York, 1985), Ch. 7.

[47] D. Beysens, A. Steyer, P. Guenoun, D. Fritter and C. M. Knobler, “How does dew form”, *Phase Transitions* **31**, 219 (1991).

[48] Lord Rayleigh, “Breath figures”, *Nature* **86**, 416 (1911).

[49] Lord Rayleigh, “Breath figures”, *Nature* **90**, 436 (1912).

[50] J. Aitken, “Breath figures”, *Nature,* **86**, 516 (1911).

[51] J. T. Baker, “Breath figures”, *Phil. Mag.* **S. 6. 44**, 752 (1922).

[52] D. Beysens and C. M. Knobler, “Growth of breath figures”, *Phys. Rev. Lett.* **57**, 1433 (1986).

[53] C. M. Knobler and D. Beysens, “Growth of breath figures on fluid surfaces”, *Europhys. Lett.* **6**, 707 (1988).

[54] A. Steyer, P. Guenoun, D. Beysens and C. M. Knobler, “Two-dimensional ordering during droplet growth on a liquid surface”, *Phys. Rev. B* **42**, 1086 (1990).

[55] A. Steyer, P. Guenoun and D. Beysens, “Hexatic and fat-fractal structures for water droplets condensing on oil”, *Phys. Rev. E* **48**, 428 (1993).

[56] B. J. Briscoe and K. P. Galvin, “The evolution of a 2D constrained growth system of droplets — breath figures”, *J. Phys: D* **23**, 422 (1990).

[57] B. J. Briscoe and K. P. Galvin, “An experimental study of the growth of breath figures”, *Colloids and Surfaces* **56**, 263 (1991).

[58] A. V. Limaye, R.D.Narhe, A. M. Dhote and S. B. Ogale, “Evidence for convective effects in breath figure formation on volatile fluid surfaces”, *Phys. Rev. Lett.* **76**, 3762 (1996).

[59] O. Pitois and B. François, “Crystallization of condensation droplets on a liquid surface”, *Colloid. Polym. Sci*. **277**, 574 (1999).

[60] P. Dell’Aversana and G. P. Neitzel, “When liquids stay dry”, *Physics Today* **Jan.**, 38 (1998).

[61] E. Yablonovitch, “Photonic band-gap structures”, *J. Opt. Soc. Am. B* **10**, 283 (1993).

[62] J. D. Joannopoulos, P. R. Villeneuve and S. Fan, “Photonic crystals: putting a new twist on light”, *Nature* **386**, 143 (1997).

[63] J. S. Rossier, M. A. Roberts, R. Ferrigno and H. H. Girault, “Electrochemical detection in polymer microchannels”, *Anal. Chem.* **71**, 4294 (1999).

[64] J. Voldman, M. L. Gray and M. A. Schmidt, “Microfabrication in biology and medicine”, *Annu. Rev. Biomed. Eng.* **1**, 401 (1999).

[65] J. Aizenberg, A. Tkachenko, S. Weiner, L. Addadi and G. Hendler, “Calcitic microlenses as part of the photoreceptor system in brittlestars”, *Nature* **412**, 819 (2001).

[66] S. Mann and G. A. Ozin, “Synthesis of inorganic materials with complex form”, *Nature* **382**, 313 (1996).

[67] N. K. Raman, M. T. Anderson and C. J. Brinker, “Template-based approaches to the preparation of amorphous, nanoporous silicas”, *Chem. Mater.* **8**, 1682 (1996).

[68] T. Nishikawa, J. Nishida, R. Ookura, S. I. Nishimura, S. Wada, T. Karino and M. Shimomura, “Honeycomb-patterned thin films of amphiphilic polymers as cell culture substrates”, *Mater. Sci. Eng. C* **8-9**, 495 (1999).

[69] T. Nishikawa, J. Nishida, R. Ookura, S. I. Nishimura, S. Wada, T. Karino and M. Shimomura, “Mesoscopic patterning of cell adhesive substrates as novel biofunctional interfaces”, *Mater. Sci. Eng. C* **10**, 141 (1999).

[70] T. Nishikawa, M. Nonomura, K. Arai, J. Hayashi, T. Sawadaishi, Y. Nishiura, M. Hara and M. Shimomura, “Micropatterns based on deformation of a viscoelastic honeycomb mesh”, *Langmuir* **19**, 6193 (2003).

CHAPTER 2

FILM PREPARATION AND MORPHOLOGY CHARACTERIZATION

In this study, we focus on two kinds of polymers — flexible linear polystyrenes with various end groups and semi-rigid conjugated polymers devoid of polystyrene coils. On the one hand, although many polymers have been found to form ordered macroporous structures by this “moist-casting method”, most of them are related to polystyrene, either star-like polystyrenes or copolymers with polystyrene blocks [1-6], which limits the understanding of the structure formation. On the other hand, linear polystyrenes can be easily obtained in bulk, either by simple syntheses in a chemistry laboratory or by direct purchase from a chemical company. Also, they have been fully studied and widely used in different areas from academic research to industrial manufacturing. Conjugated polymers are promising semiconducting materials which can work as the active elements in heterojunction devices such as organic light-emitting diodes (OLEDs) [7,8], thin-film transistors [9,10], solar cells [11,12], and sensors [13]. Nano- or micro-structuring the semiconducting polymers is of critical importance to these applications and there is no easy method available up to now [14]. By applying this simple casting method, macroporous films can be prepared in tens of seconds.

To characterize the morphology of the macroporous films, a normal optical microscope and a laser scanning confocal microscope were used since the size of the pores is in the micron range. Some background about optical microscopy, especially confocal microscopy, is given in section 2.2.

2.1 Experiments

2.1.1 Film Preparation

2.1.1.1 Materials

Table 2.1 lists polystyrenes with various end groups and molecular weights used in the preparation of the porous films, with data of the weight-averaged molecular weight (M_w), the polydispersity index (PDI), and the hydrodynamic radius (R_h). They are all commercially available, where the carboxyl- or hydroxyl-terminated ones were bought from Scientific Polymer Products, Inc. and the standards were from Aldrich Chemical Company, Inc.

Figure 2.1-2.3 gives the chemical structures of the semi-conducting polymers used, where the polyfluorene homopolymer and copolymers (PFOs) were obtained from Dr. D. D. C. Bradley at Imperial College in London, UK, and the poly[*p*-(phenylene)ethynylene]s with different side chains (PPEs) and polythiophene (PT) were prepared by Dr. Bunz's group at Georgia Tech.

The solvents used are carbon disulfide (CS_2) and benzene, both reagent A.C.S. grades. They were purchased from Fisher Scientific Inc., and used as received without further purification.

Table 2.1 Data (weight-averaged molecular weight, M_w, polydispersity index, PDI, and hydrodynamic radius, R_h) of linear polystyrenes used in the preparation of the highly-ordered macroporous films.

Polystyrene (atactic)	M_w[a] (g/mol)	Abbreviation	M_w[b] (g/mol)	PDI[b]	R_h[b]
Mono-carboxyl terminated	50,000	PS1c50	39,800	1.11	6.3
Di-carboxyl terminated	25,000	PS2c25	15,600	1.18	3.6
	50,000	PS2c50	51,600	1.21	7.4
	100,000	PS2c100	105,000	1.32	11.1
Mono-hydroxyl terminated	10,000	PS1h10	7,390	1.12	1.6
	100,000	PS1h100	91,900	1.16	/
Polystyrene standards	18,700	PS18	/	/	/
	29,300	PS29	/	/	/

[a] Data provided by Manufacturer

[b] Data measured using Waters GPC (Gel Permeation Chromatography) in conjunction with Wyatt QELS (Quasi-Elastic-Light-Scattering) instrument with THF (HPLC grade) as a solvent

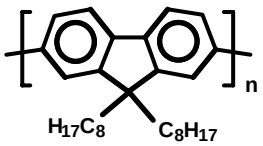

Poly(9,9-dioctylfluorene) [PFO]

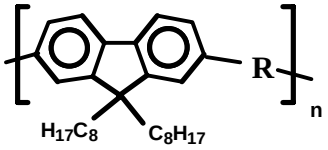

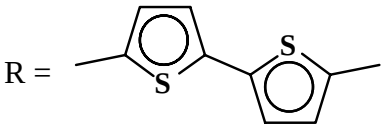

Poly(9,9-dioctylfluorene-co-bithiophene) [F8T2]

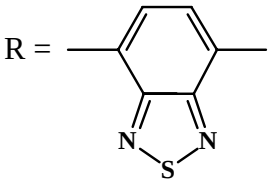

Poly(9,9-dioctylfluorene-co-benzothiadiazole) [F8BT]

Figure 2.1 Chemical structures of polyfluorene homopolymer (PFO) and copolymers (F8T2 and F8BT) used in the preparation of the macroporous films.

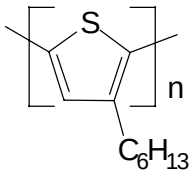

Poly(3-hexylthiophene) [hexPT]

Figure 2.2 Chemical structure of polythiophene (hexPT) used in the preparation of the macroporous films.

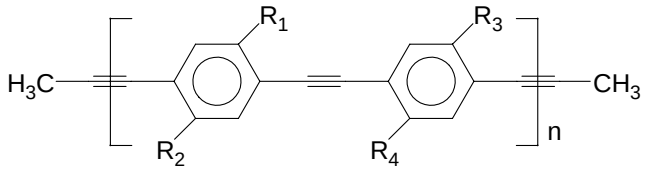

$R_1 = R_2 = R_3 = R_4$ = 2-(ethyl)hexyl = 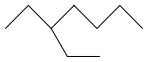 [ehexPPE]

$R_1 = R_2 = R_3 = R_4$ = hexoxy = 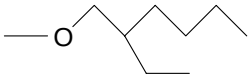 [hexoPPE]

$R_1 = R_3$ = tri-isopropylsilane, $R_2 = R_4$ = methyl [tipsPPE]

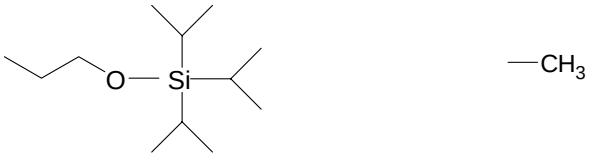

$R_1 = R_2$ = 2-(ethyl)hexyl, R_3 = azide , R_4 = methyl [azidePPE]

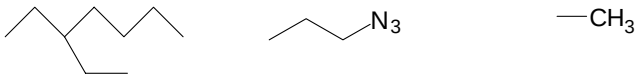

Figure 2.3 Chemical structures of poly[*p*-(phenylene)ethynylene]s (PPEs) with different side chains used in the preparation of the macroporous films.

2.1.1.2 Apparatus

Two types of apparatus have been used to make the macroporous films. A simple setup is sketched in Figure 2.4. Bubbler, buffer, airflow meter and glass chamber are connected by plastic tubing (Tygon, 1/4" in diameter). The glass chamber consists of a rectangular glass tube (open ends, $200 \times 30 \times 10$ mm^3) sealed with a glass cap by a rubber band at each end. A glass slide can be inserted into the glass chamber by removing one rubber band and the glass cap at that end. The polymer solution is loaded through an orifice at the side of the glass chamber using a syringe. Compressed air is bubbled through distilled water in the bubbler at different flow rates.

The other equipment (Apparatus II, customized by CARON Products & Service, Inc., see Figure 2.5) with controlled temperature and humidity was used for film preparation and the study of humidity effect on the film morphology. It consists mainly of two parts: i) a conditioning chamber, where airflow is tailored to the desired conditions, and ii) an environmental chamber, where the macroporous film is prepared. The two parts are connected by ducts. The arrows represent the directions of airflow. Ambient air flows into the front of conditioning chamber, where its temperature and humidity are adjusted toward the preset values, then passes through environmental chamber and goes out from the back of the conditioning chamber. Temperature and humidity can be preset and read through the temperature and humidity control panel located on the front surface of the conditioning chamber. A temperature sensor is placed at the inlet to the environmental chamber and the feedback is sent back to the conditioning chamber through a temperature receptacle. Humidity is added into the air through a water inlet connected to distilled water. Airflow velocity can be adjusted via a dial knob in the fan control panel.

Sample is loaded from the top of the environmental chamber by removing the lid. A window with work light is installed in the lid so that the film formation can be observed.

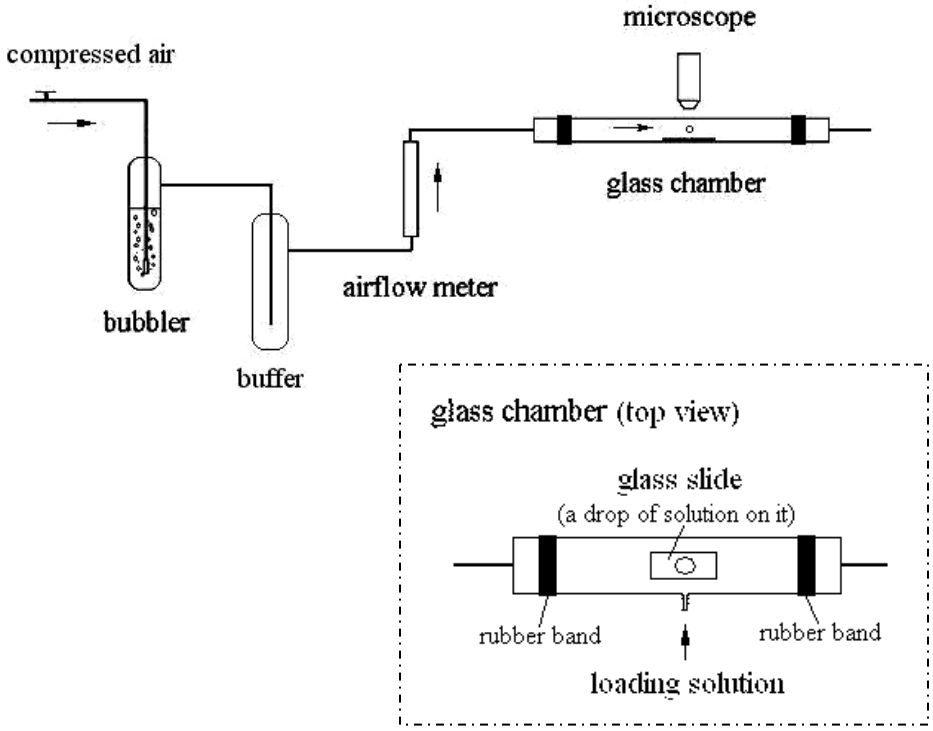

Figure 2.4 Schematic of an experiment setup (Apparatus I) for the preparation of the macroporous films.

(a) Top view

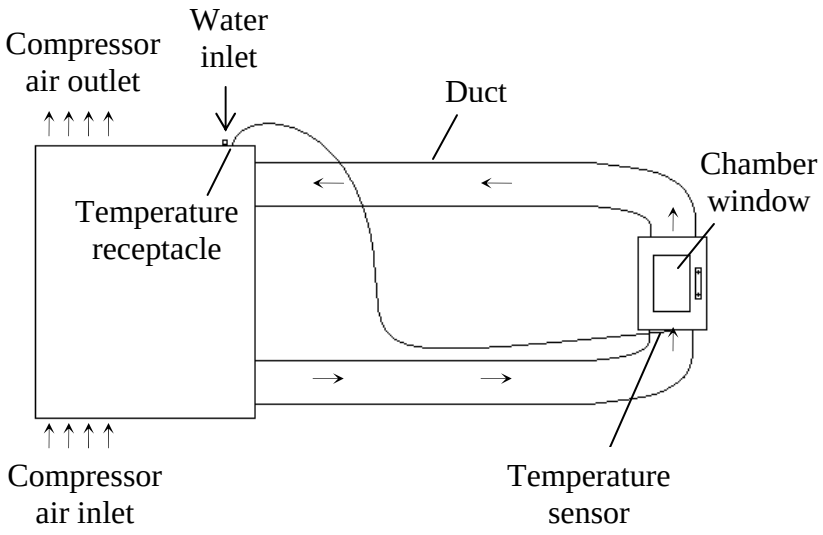

(b) Side view

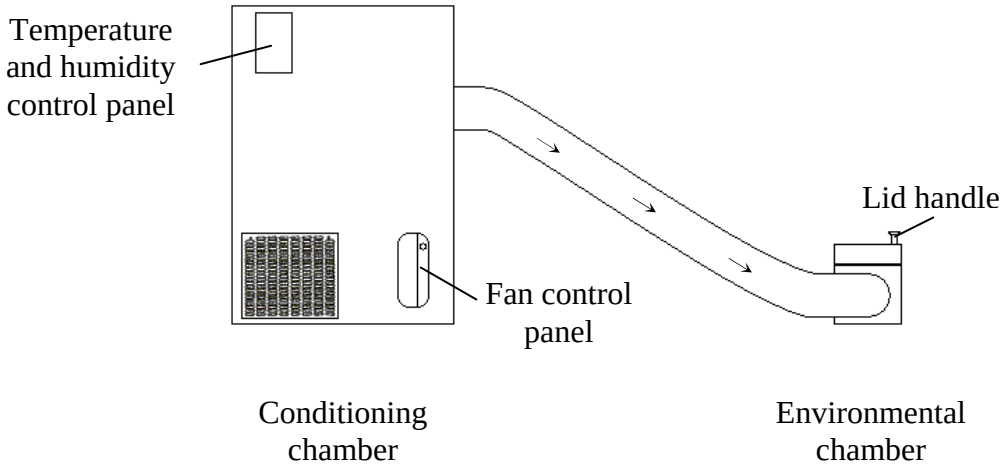

Figure 2.5 Schematic of an experiment setup (Apparatus II, customized by CARON Products & Service, Inc.) for the preparation of the macroporous films.

2.1.1.3 Film Preparation

A layer of dilute polymer solution is spread on a substrate and blown with moist air to make the macroporous film. Different conditions (concentration of the polymer solutions, and humidity and speed of the airflow) are used, as listed in Table 2.2. The temperature is set at room temperature to avoid condensation of water droplets on the walls of the flow path and the chamber for film preparation. In addition to the films made of single polymer, two or three kinds of polymers are mixed together to make films of polymer blends. Microscope glass slides, silicon wafers and water have been used as substrates.

Table 2.2 Conditions used in making the macroporous films.

Conditions	Apparatus I	Apparatus II
Relative Humidity (%)	N/A	70 – 100
Flow Rate (m/min)	(0 – 40)[a]	(0 – higher than 344)[b]
Temperature (°C)	Room Temperature	
Solution Concentration	0.8–5 wt. % for polystyrenes 0.1–0.5 wt. % for semi-conducting polymers	

[a] Calculated from the readings of the flow meter (volume flow rates multiplied by the cross-section of the glass chamber) in Figure 2.4.

[b] Data from manufacturer, measured by placing a flow meter inside the conditioning chamber in Figure 2.5.

2.1.2 Morphology Characterization by Optical Microscopy

An optical microscope (Leica DMRX, 40× 0.75 dry or 50× 0.75 dry objective) coupled with a CCD camera was used to image the films and, with the help of a Bertrand lens, the correspondent Fraunhofer diffraction patterns. An interference filter (central λ = 532 ± 2 nm, FWHM = 10 ± 2 nm) was used to give nearly monochromatic light. To get sharp diffraction patterns, aperture diaphragm was closed down to the minimum to get well-collimated normally-incident light.

A laser scanning confocal microscope (LSCM, Leica TCS SP, 40× 0.75 dry, 50× 0.75 dry or 100× 1.4 oil objective) was used to image the surface morphology and the three-dimensional structure of the films. 488-nm light produced by an Ar^+ laser was used to illuminate the films and the reflected, fluorescent (500-700 nm) and transmitted lights were collected by three photomultipliers separately. For 3D images, a sample film was optically sectioned, either parallel to (xy-scan) or normal to (xz-scan) the film surface. After a series of scans at different planes through a film (generally the spacing between consecutive scans is 0.041 μm for the xy-scan and 0.065 μm for the xz-scan), images of these planes were combined to reconstruct 3D views or orthogonal-sectioning images of the porous film via computer software (Leica TCSNT).

2.2 Basics of Optical Microscopy

Optical microscopy is a convenient tool for studying morphology of specimens at micron and submicron level. The basic idea is that upon illumination, fine information of a sample is magnified by an objective and further by an eyepiece so that they can be discerned by human eyes or optical detectors [15-18]. Both the objective and the eyepiece

are composed of a series of lenses to obtain desired magnification without significant optical aberrations [15,16]. For simplicity, they can be looked as two ideal convex thin lenses. Depending on the optical and geometrical properties of the sample, transmitted, reflected or fluorescent light from the sample can be collected to image the sample [17]. Image formation in a transmitted optical microscope will be discussed in some detail in Chapter 3.

Resolution and contrast are two factors dictating image quality. For sample details to be seen or resolved by a microscope, the resolution of the microscope needs to be equal to or smaller than the size of the details. If the separation of two adjacent points is below the resolution, the two points will appear to be one. Following Rayleigh's criterion [15-18], the resolution of a conventional optical microscope is often defined as

$$d = \frac{0.61\lambda}{\mathrm{NA}}, \tag{2.1}$$

where, λ is the wavelength of light (most commonly, 400–700 nm) and NA is the numerical aperture of the objective, defined as $n\sin\theta_{\mathrm{NA}}$, with n being the refractive index of the dispersion medium and θ_{NA} being the angular semi-aperture of the objective, i.e., the maximum angle with respect to the optical axis at which diffracted light can go into the objective [15-18]. Depending on the objective aperture and the dispersion medium (air, immersion oil or water) between the sample and the objective lens, the value of NA changes from 0.1 to 1.4. According to Eq. (2.1), the shorter the wavelength and the higher the numerical aperture of the objective, the higher the resolution can be achieved.

In reality, resolution is affected by contrast to a large degree [17,18]. For an object to be observed, there needs to be optical contrast, that is, intensity difference between light from the object and that from the surrounding or background. When white

light is used for illumination, this intensity difference can appear as color difference. Different contrast-enhancing techniques, from simply staining samples to complex ones such as phase contrast and differential interference contrast (DIC), have been utilized to increase contrast of low intrinsic-contrast specimens in microscopy [17,18]. Even for specimens with enough intrinsic-contrast, the obtained contrast in an image by a microscope can be significantly affected by the way the image is taken, that is, by the imaging principle and the quality of the microscope. One principle to obtain high-contrast images is to reduce undesired noisy light [18]. Noise can degrade contrast and further obscure resolution. When a dim spot is next to a very bright one, with noise added, they may not be resolved even with their separation larger than the resolution [18].

In a conventional wide-field optical microscope, a specimen is uniformly and simultaneously illuminated over the field-of-view area through the entire thickness [17,18]. Sample details in the in-focus plane can be obscured by light from out-of-focus regions as well as stray light. This situation becomes worse for fairly thick samples or fluorescent microscopy where fluorescent light (in a longer wavelength than the illumination) remitted from a sample is collected to image the sample [17]. Bright fluorescent signals from the regions outside the in-focus plane can reduce the contrast [17].

Comparing with a conventional wide-field optical microscope, a laser scanning confocal microscope (LSCM) illuminates a sample point by point in a raster pattern over a sample plane. With point illumination and an aperture in front of the detector (detector pinhole), a laser scanning confocal microscope is able to eliminate most of the out-of-focus light and stray light to image optical sections in a thick sample in much higher

contrast [18]. Further, a series of optical sections through the sample can be recombined by computer software to give 3D images of the specimen. Figure 2.6 is a schematic showing the principle of a laser scanning confocal microscope [17,18]. Light from a laser source first passes an aperture (the source pinhole) and is subsequently expanded to fill the rear aperture of the objective [17]. After being reflected by a beam splitter, the expanded light is focused by the objective into a diffraction-limited spot at the in-focus sample plane. Note that the focused spot is a diffraction disk with finite diameter and thickness due to the wave nature of light, so the in-focus sample plane actually has a measurable thickness which is called depth of field [17]. The detailed theory of diffraction in image formation can be found in optical-physics books [15,16] Upon the spot illumination, light (reflected or fluorescent) from the in-focus sample region (a diffraction-limited disk) is collected by the objective and passes back through the beam splitter to focus at the detector pinhole. Since the source pinhole, the illuminated spot in the sample and the detector pinhole are mutually conjugate (i.e., confocal), that is the origin of the name “confocal microscopy” [18], by limiting the illuminated sample volume to a focused spot at a time, most of the nearby sample volume is not illuminated so that no noisy light comes from it at all. And for the volume within the path of the illuminating beam and out of focus, most of the reflected or fluorescent light will be cut-off by the detector pinhole without reaching the detector [18].

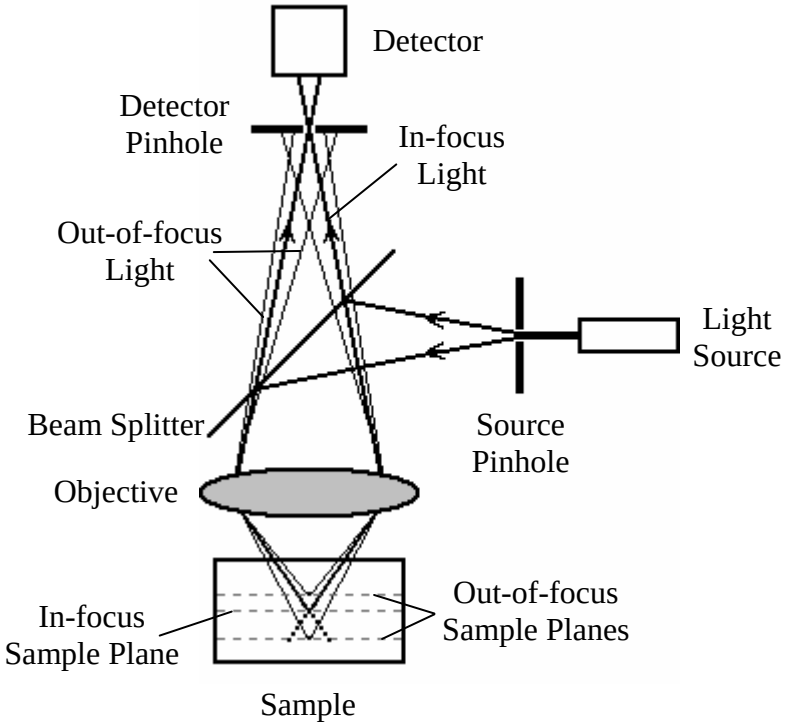

Figure 2.6 Optical principle of confocal microscopy. Light from a laser source first passes an aperture (the source pinhole) and is subsequently expanded to fill the back aperture of objective. After reflected by a beam splitter, the expanded light is focused by the objective into a small spot at the in-focus sample plane. Then light remitted from the in-focus sample volume is collected by the objective and passes back through the beam splitter to focus at the detector pinhole. Most of the light remitted from out-of-focus planes is rejected by the detector pinhole from reaching detector [17,18].

2.3 Results

2.3.1 Structuring Polymer Films by "Moist Casting"

As observed by other researchers [19-21], with a suitable polymer/solvent system and the right conditions (e.g., the concentration of the polymer solution, the temperature and humidity of the air flow, etc), soon after moist air was blown across a layer of polymer solution spread on a substrate, an opaque layer formed on top of the solution, showing iridescent colors when illuminated by white light. Solvent evaporated in tens of seconds depending on the vapor pressure of the solvent and the amount of the evaporating solution, leaving an opaque polymer film. Sometimes, on a humid day, this process happened in open air without the need of moist airflow. Figure 2.7 is a macroscopic image of a finished film, which gives iridescent colors as well and the colors change when the film is observed from different angles. Both of the iridescent colors seen on the solution and on the film are due to the scattering and interference of white light, respectively by an ordered array of water droplets and by an ordered array of air bubbles (which gives periodic refractive-index variation), in sizes which are comparable to the wavelength range of the illumination. The different colors across the solution or the film are because of the different orientation of grains as well as the different size of water droplets or air bubbles.

(a)

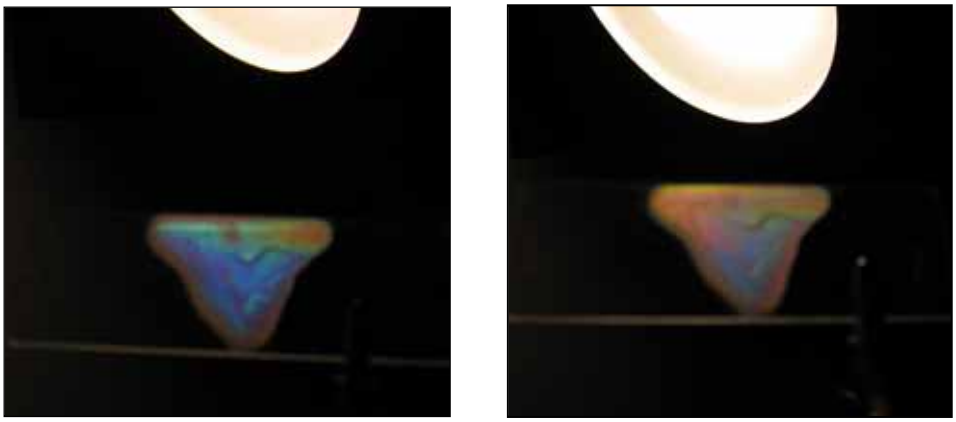

(b)

Figure 2.7 Iridescent color seen on a macroporous film with ordered array of air bubbles, when it was illuminated with (a) an incandescent lamp (the bright area on the top of each image is a part of the lamp cover) and (b) an incandescent flash light. Color of the film changed when illuminated or observed at different angles. The images were taken by a digital camera (Canon A80). For the images in (a), the aperture diaphragm of the camera was closed down to the minimum to increase contrast. The film was made of polystyrene (PS1c50, ~ 1 wt. %), cast from carbon disulfide under moisture airflow using Apparatus I (the airflow speed ~ 13.7 m/min). The size of the air pores in the film is about 1.8-2.5 μm in diameter. The straight side of the triangle film is 3 cm.

2.3.1.1 Films Made of Polystyrenes and Their Blends

Under the experimental conditions, linear polystyrenes terminated with one or two carboxyl endgroups (PS1c50, PS2c25, PS2c50, PS2c100) can form ordered macroporous structures, with an optimal concentration of around 1% by weight and relative humidity of 80–90%. When benzene was used as a solvent, higher humidity and faster airflow were needed. Figures 2.8–2.11 give some examples of the cast polystyrene films. Figure 2.8 and Figure 2.9 are imaged by a normal optical microscope (Leica DMRX) in transmission mode. The insets in Figure 2.8 are the correspondent Fraunhofer diffraction patterns which were imaged by adding a Bertrand lens into the optical path of the microscope. The spot diffraction patterns with six-fold symmetry are evident of the highly ordered, hexagonal arrays. A detailed description of the diffraction patterns can be found in Chapter 3. Figure 2.10 and Figure 2.11 are images of film surfaces by a laser scanning confocal microscope (Leica TCS SP) in the fluorescence mode. The bright green region is polystyrene and the black one is air.

Generally films cast from benzene looked more opaque. Comparing Figures 2.8 and 2.10 with Figures 2.9 and 2.11, it can be seen that carbon disulfide gives more ordered morphology (i.e., closely packed, mono-dispersed air pores). Films made from benzene solutions have the packed air pores, but more defects so that the films have much smaller ordered grains (a grain is used to represent a closed area with only one set of orientations, i.e., a 2D crystal). Generally, the diffraction patterns of the films cast from benzene are more blurry because of the overlap of several sets of diffraction spots with different orientations.

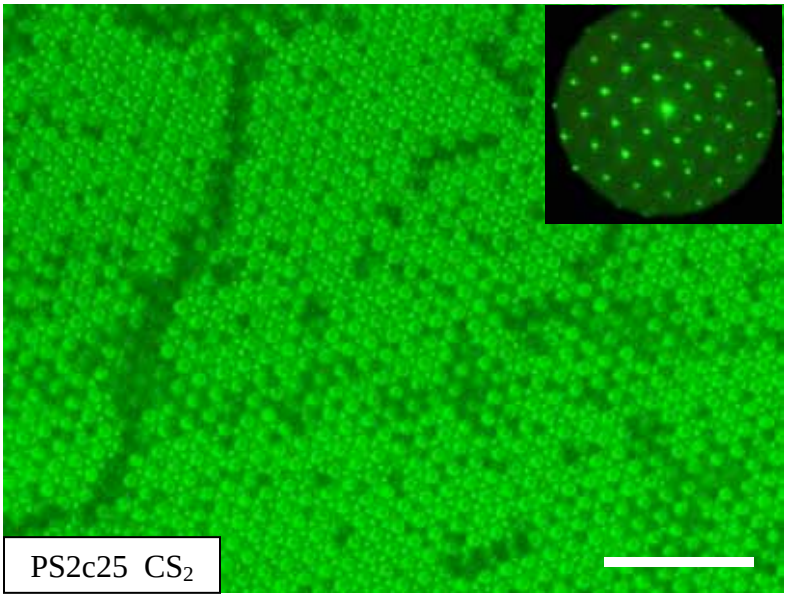

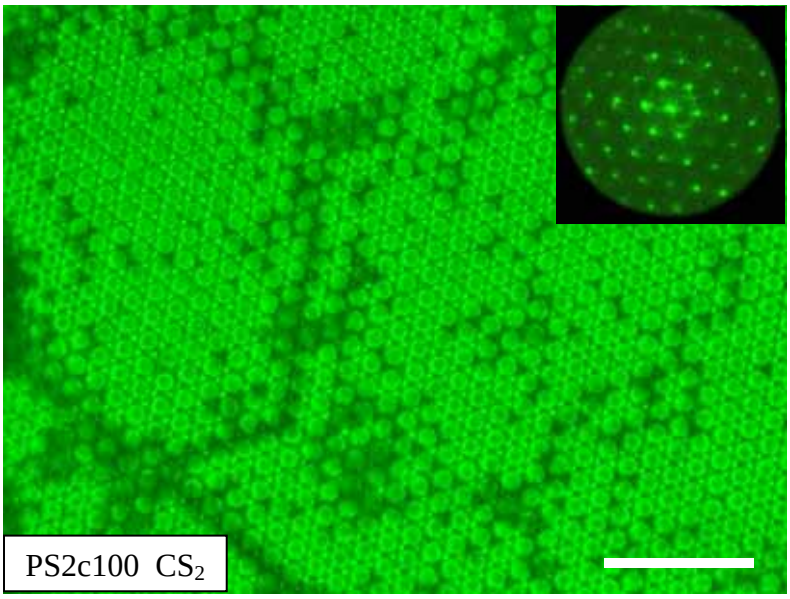

Figure 2.8 Images of macroporous polystyrene films cast from carbon disulfide at a concentration of 1 wt. % using Apparatus II. The relative humidity was 84% and the airflow speed was around 240 m/min for both. Images were taken by an optical microscope (Leica DMRX, 50× 0.75 dry objective) using transmitted white light. The inset in each image is the correspondent Fraunhofer diffraction pattern, which was imaged by adding a Bertrand lens into the optical path of the microscope. An interference filter (λ = 532 nm) was used to give nearly monochromatic light. Scale bar: 20 μm.

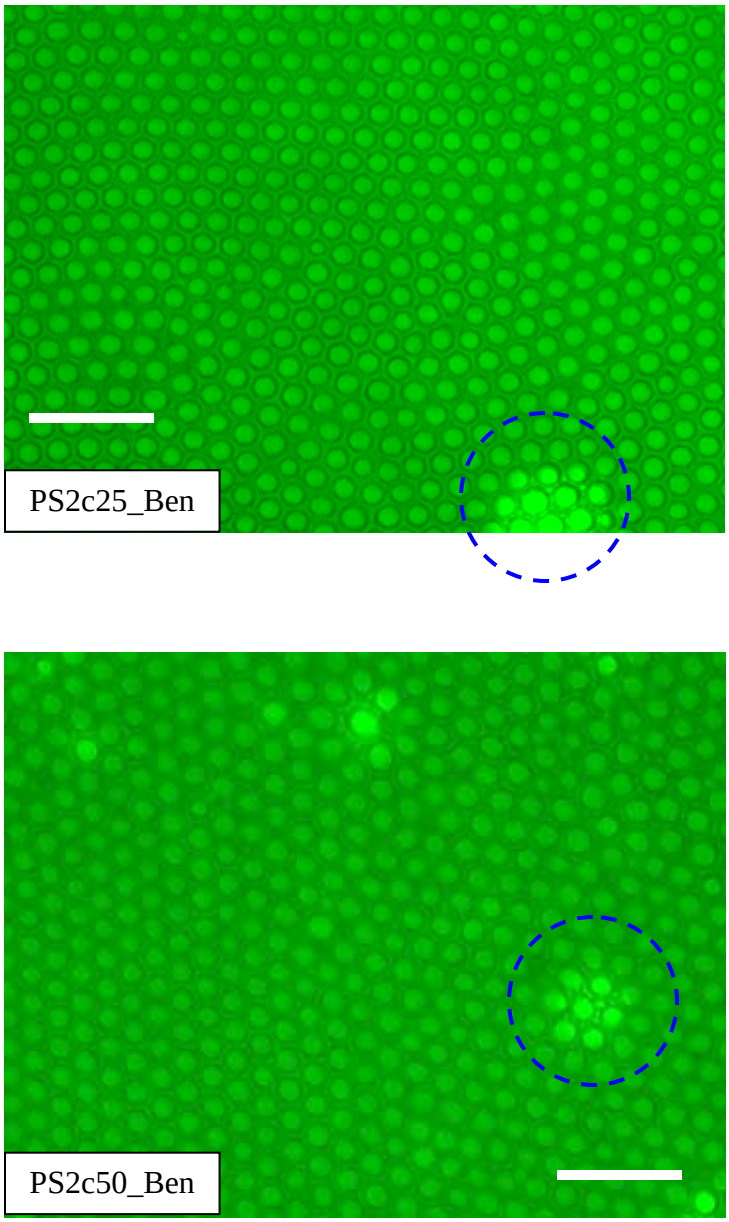

Figure 2.9 Images of macroporous polystyrene films cast from benzene at a concentration of 1 wt. % using Apparatus II. The relative humidity was 90% and the airflow speed was around 400 m/min for both. Bright spots as marked by the blue dashed circles were often observed. Images were taken by an optical microscope (Leica DMRX, 40× 0.75 dry objective) in transmission mode. An interference filter (λ = 532 nm) was used to give nearly monochromatic illumination. Scale bar: 20 μm.

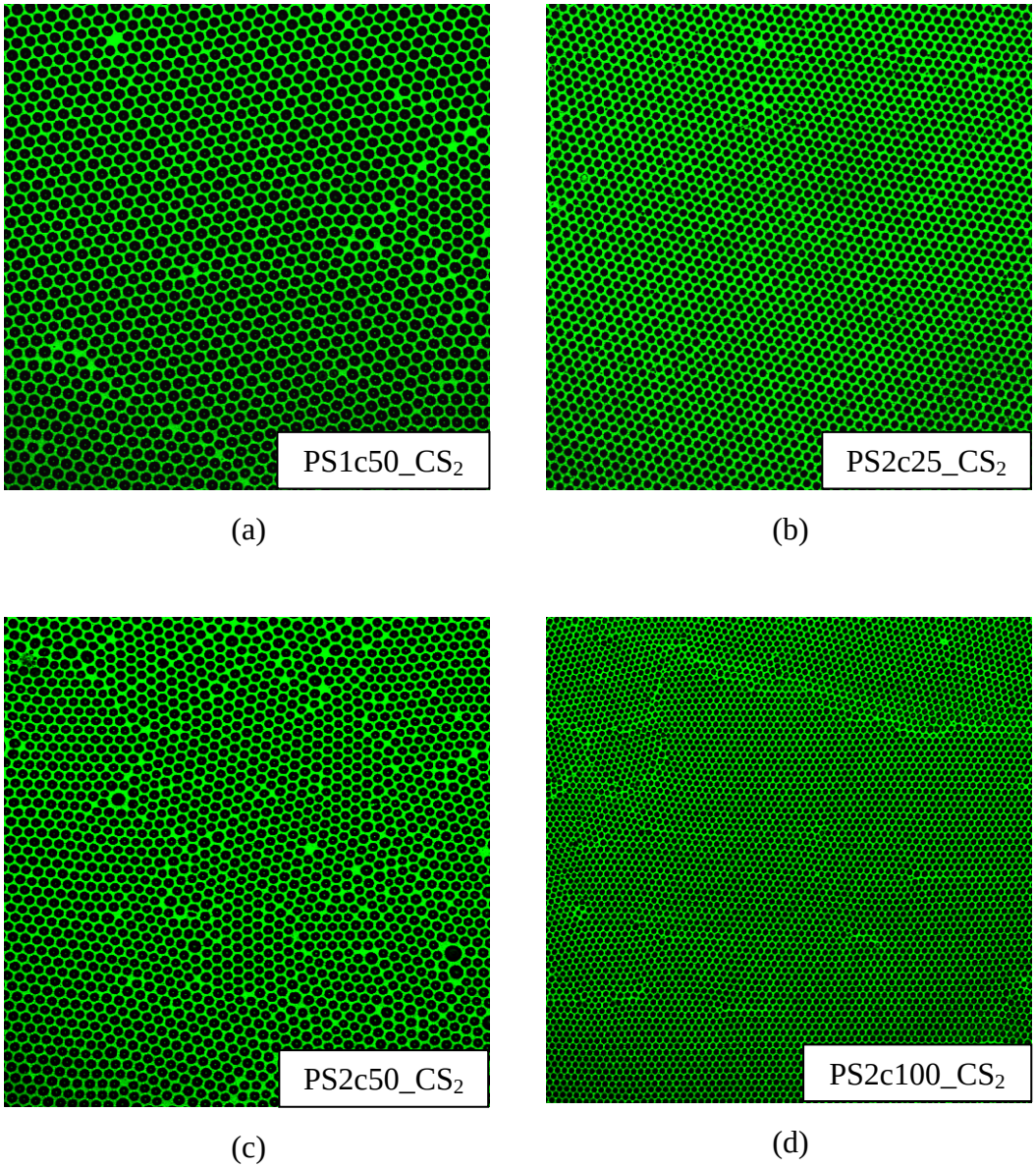

Figure 2.10 Images of macroporous polystyrene films cast from carbon disulfide at a concentration of 1 wt. % using Apparatus II. The relative humidity was 84% for all and the airflow speed was around 240 m/min for all the four films. Images are taken by a laser scanning confocal microscope (Leica TCS SP, 50× 0.75 dry objective). All of the images are in the size of 200 × 200 μm^2.

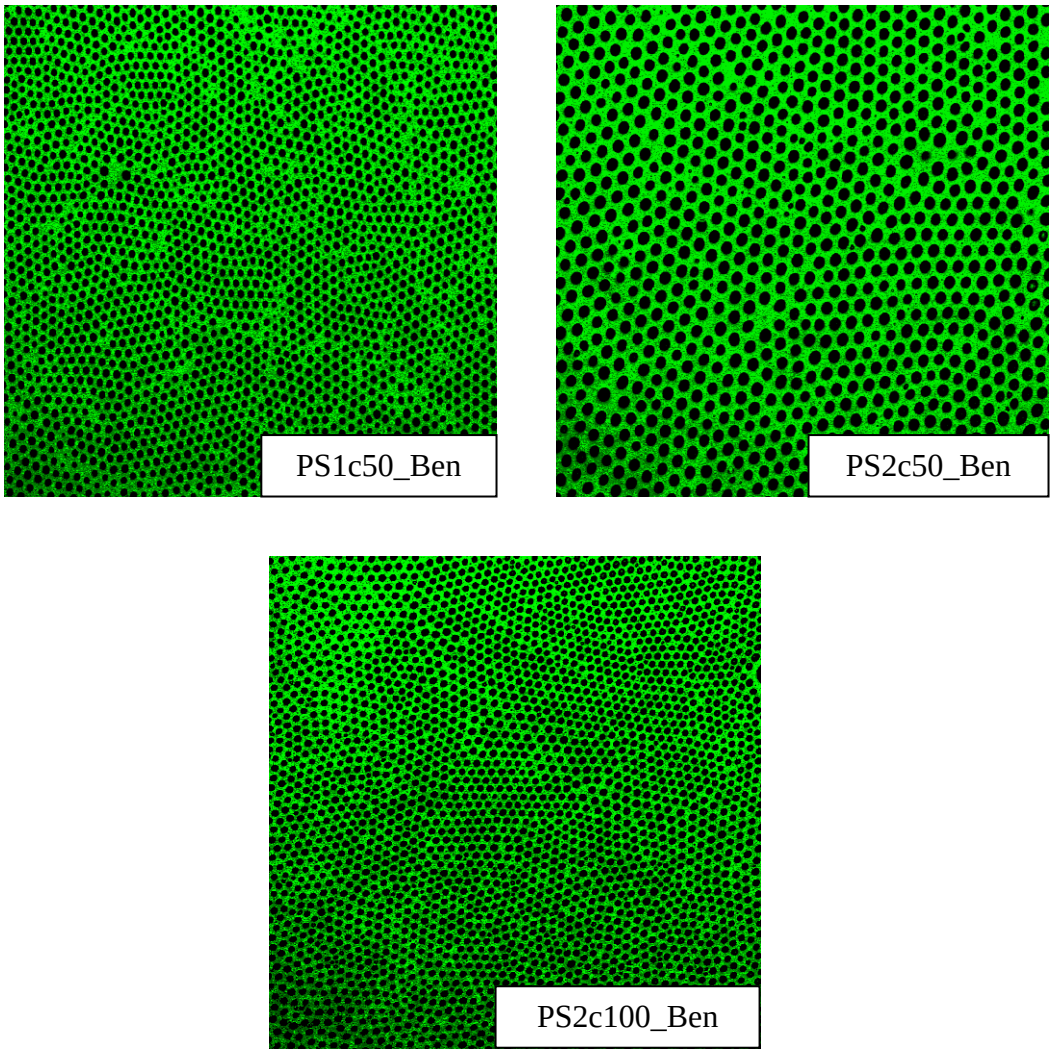

Figure 2.11 Images of macroporous polystyrene films cast from benzene at a concentration of 1 wt. % using Apparatus II. The relative humidity was 90% and the airflow speed was around 400 m/min for all the three films. Images are taken by a laser scanning confocal microscope (Leica TCS SP, 50× 0.75 dry objective). All of the images are in the size of 200 × 200 μm^2.

Polystyrenes with one hydroxyl end group (PS1h10 and PS1h100) and polystyrene standards without end group (PS18 and PS29) did not form ordered macroporous structures when prepared under the same experimental conditions. However, by adding a small amount of polystyrenes which can form ordered structures into the polymer solutions, more ordered structures can be prepared. One example is given in Figure 2.12, where PS2c100 was blended into PS29. It can be seen that much ordered porous structure was obtained when the ratio of the amount of PS2c100 to that of PS29 is 1:15 by weight. Similar phenomena were seen for the other blends. In addition, ordered macroporous films were obtained from blends of polystyrenes which were able to form well-ordered films when cast separately (Figure 2.13). As well, they can be blended with polymers which cannot form ordered structures to get more ordered array of air pores (Figure 2.14).

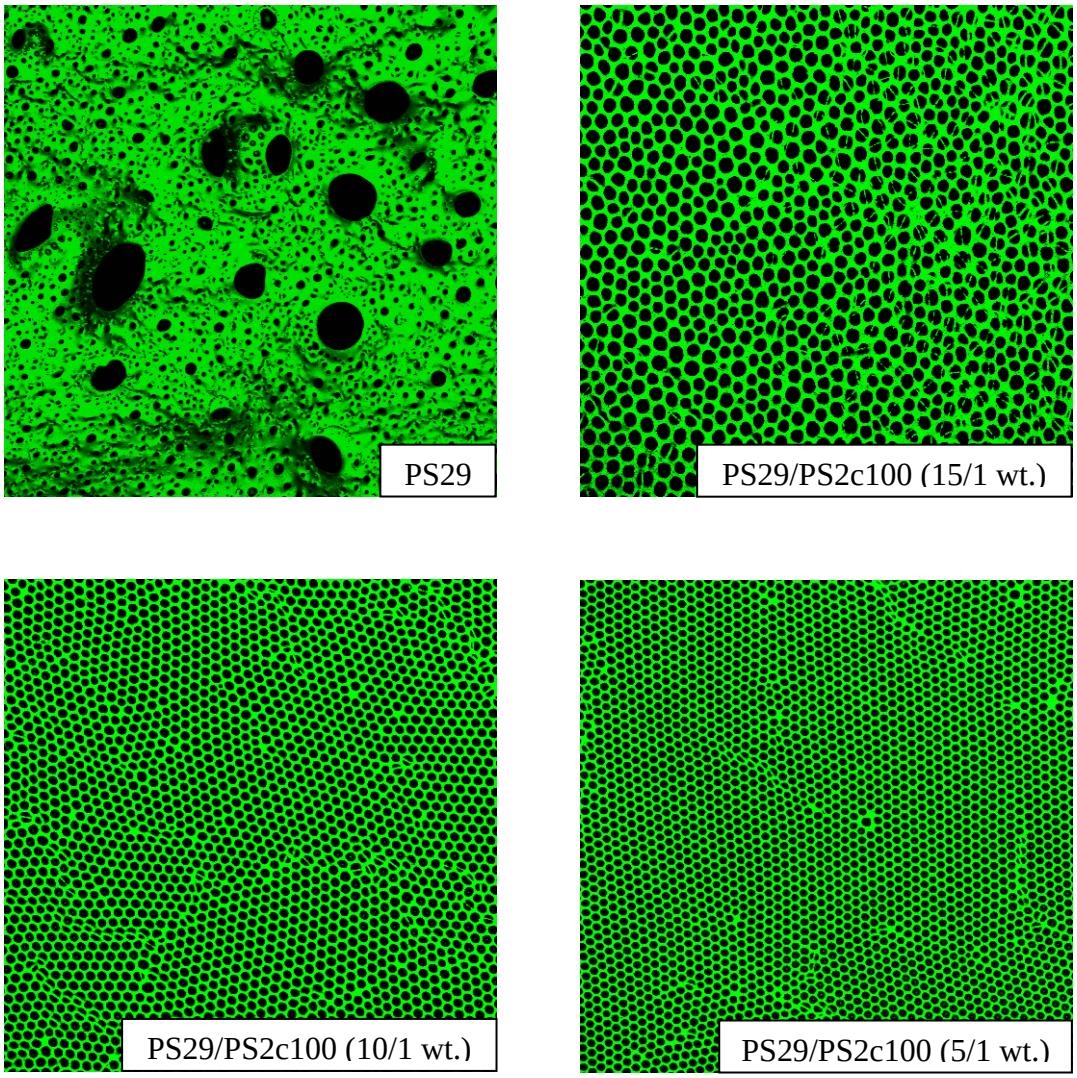

Figure 2.12 Macroporous films made of polystyrene standard (PS29, M_w ~ 29,300) and its blends with two-carboxyl terminated polystyrenes (PS2c100, M_w ~ 100,000). The blending ratios given in the images are by weight. All of the films are cast from carbon disulfide at a concentration of 1 wt. % using Apparatus II. The relative humidity was 84% and the airflow speed was around 240 m/min for all the four films. Images are taken by a laser scanning confocal microscope (Leica TCS SP, 50× 0.75 dry objective) in fluorescence mode. All of the images are in size of 200 × 200 μm^2.

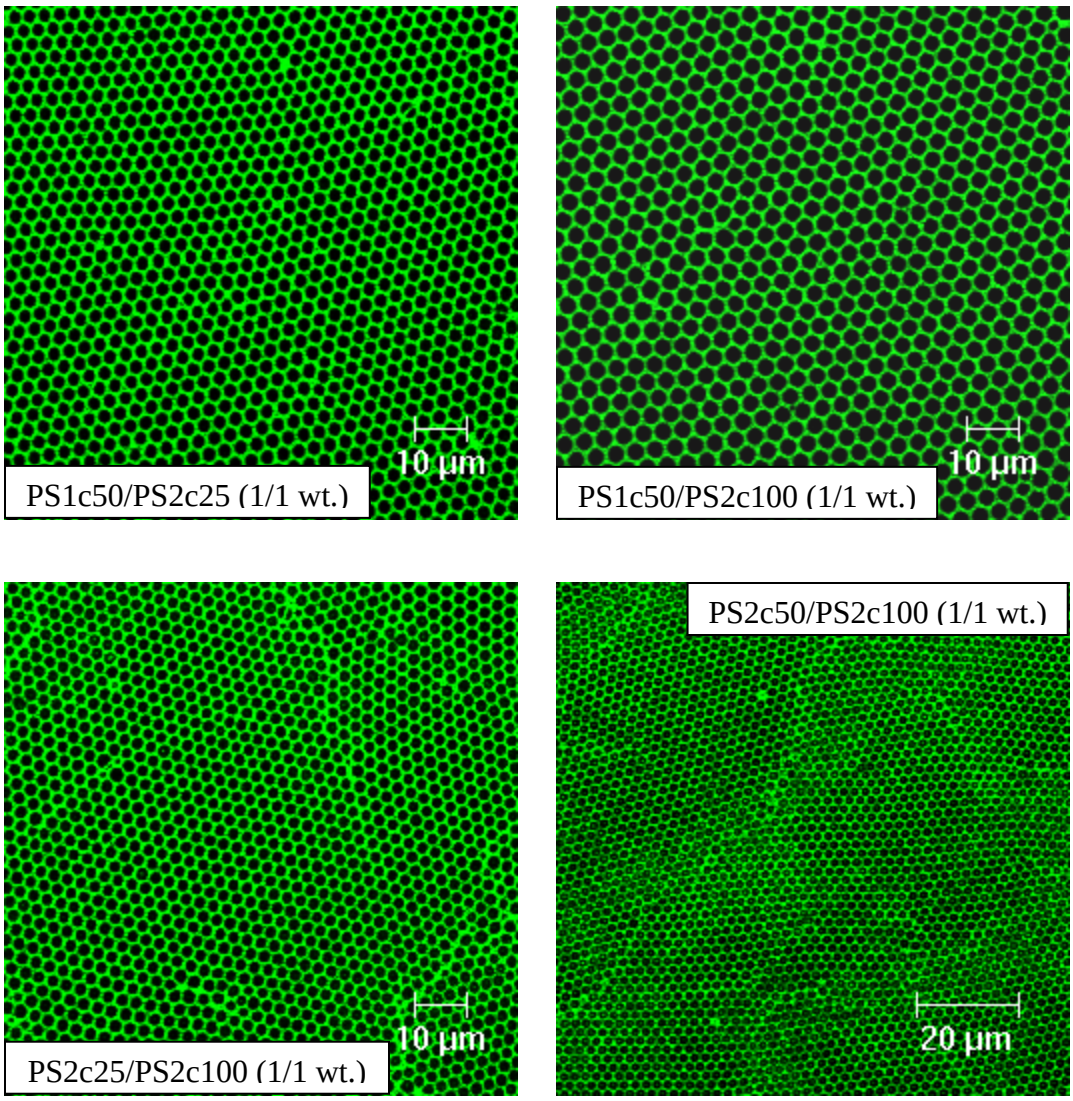

Figure 2.13 Macroporous films made of blends of different polymers as marked in the images. The blending ratio is 1:1 by weight for all four blends. All of the films are cast from carbon disulfide in a concentration of 1 wt. % using Apparatus II. The relative humidity was 84% and the airflow speed was around 240 m/min for all the four films. Images are taken by a laser scanning confocal microscope (Leica TCS SP, 50× 0.75 dry objective) in fluorescence mode. All of the images are in size of 100 × 100 μm^2.

(a)

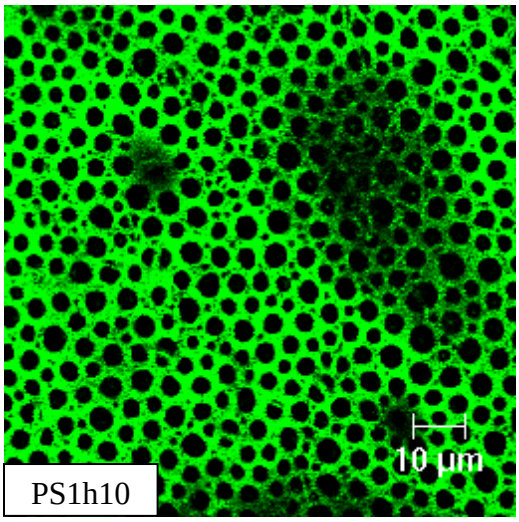

(b)

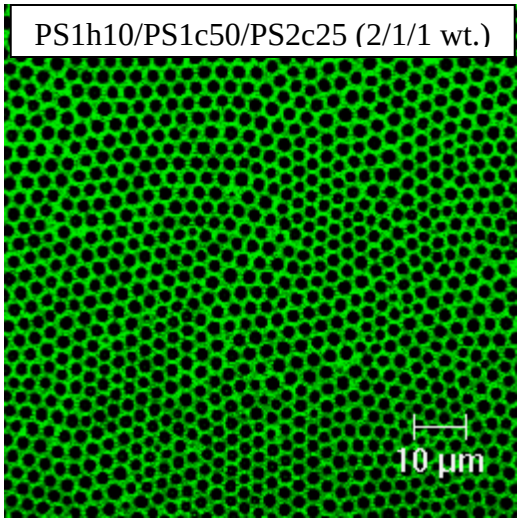

Figure 2.14 Macroporous films made of one-hydroxyl terminated polystyrene (PS1h10) and its three-component blends with carboxyl-terminated polystyrenes (PS1c50 and PS2c25). The blending ratio is 2:1:1 by weight. Films are cast from carbon disulfide in a concentration of 1 wt. % using Apparatus II. The relative humidity was 84% and the airflow speed was around 240 m/min for both. Images are taken by a laser scanning confocal microscope (Leica TCS SP, 50× 0.75 dry objective) in fluorescence mode. Both image are in size of 100 × 100 μm^2.

2.3.1.2 Structuring Semi-conducting Polymers

Well-ordered macroporous films of semi-conducting polymers including polyfluorene copolymers (F8BT and F8T2), poly[*p*-(phenylene)ethynylene]s (ehexPPE, hexoPPE, tipsPPE and azidePPE) and poly(3-hexylthiophene) (hexPT) were prepared by this "moist casting method" with carbon disulfide as a solvent (these polymers do not dissolve in benzene) in a concentration of 0.2–0.5 wt. %. Some examples are given in Figures 2.15-2.17. Generally, the grain size is larger for the films made of hexoPPE, azidePPE and tipsPPE, comparing with the rest.

When a mixture of poly(3-hexylthiophene) and C_{60} was used, depending on the amount of C_{60}, cast films showed different morphology. C_{60} precipitated only at the edge of a film with the ordered porous structure of hexPT in the central part intact (Figure 2.18a and 2.18aE) when the amount of C_{60} is low. With the increase of the amount of C_{60}, some aggregates of C_{60} (black sticks) showed up across the films. At the beginning, the "black sticks" were not seen on the top surfaces but only inside the films (i.e., below the film surfaces, Figure 2.18b and 2.18bI), small and sparsely dispersed. Later at a relative higher concentration of C_{60}, the C_{60} aggregates were seen all over the surfaces with increased size and number density; small domains of macroporous hexPT can be differentiated in between (Figure 2.19). Ordered structures of hexPT were totally destroyed by the precipitated C_{60} when the amount of C_{60} was further increased.

(a)

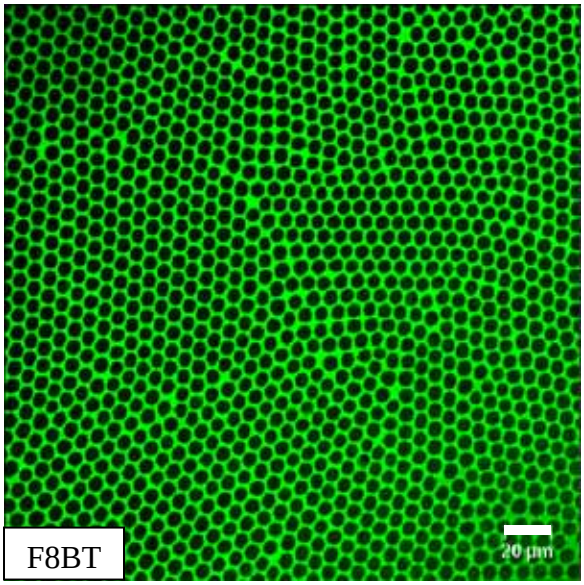

(b)

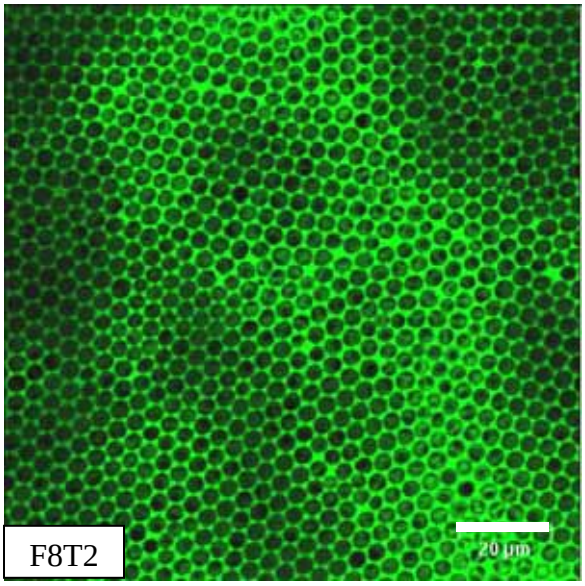

Figure 2.15 Macroporous films of polyfluorene copolymers (F8BT and F8T2). Films were prepared with carbon disulfide as a solvent using Apparatus II. The relative humidity was 84% and the airflow speeds were about (a) 100 m/min and (b) 180 m/min, respectively. Images were taken by a laser scanning confocal microscope (Leica TCS SP, 40× 0.75 dry objective) in fluorescence mode. Scale bar: 20 μm.

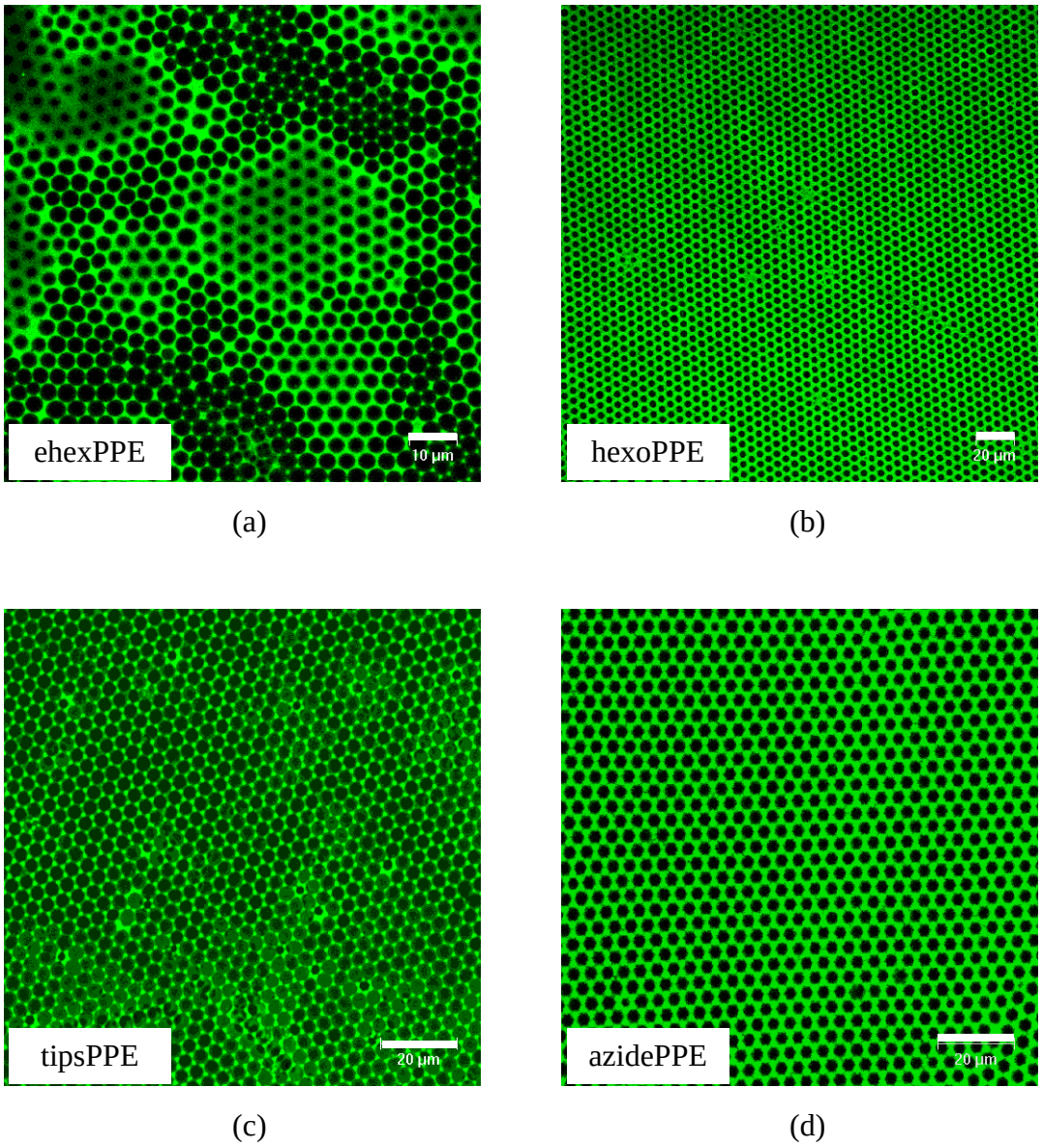

Figure 2.16 Macroporous films of PPEs with different side chains. Films were prepared with carbon disulfide as a solvent at a concentration of 0.2-0.5 wt. % using Apparatus II. The relative humidity was 84% for all the four films and the airflow speeds were around (a) 20 m/min, (b) 70 m/min, (c) 20 m/min, and (d) 70 m/min. Images were taken by a laser scanning confocal microscope (Leica TCS SP) in fluorescence mode with an objective of (a) 100× 1.4 oil, (b) – (d) 40× 0.75 dry. Scale bar: (a) 10 µm, (b) – (d) 20 µm.

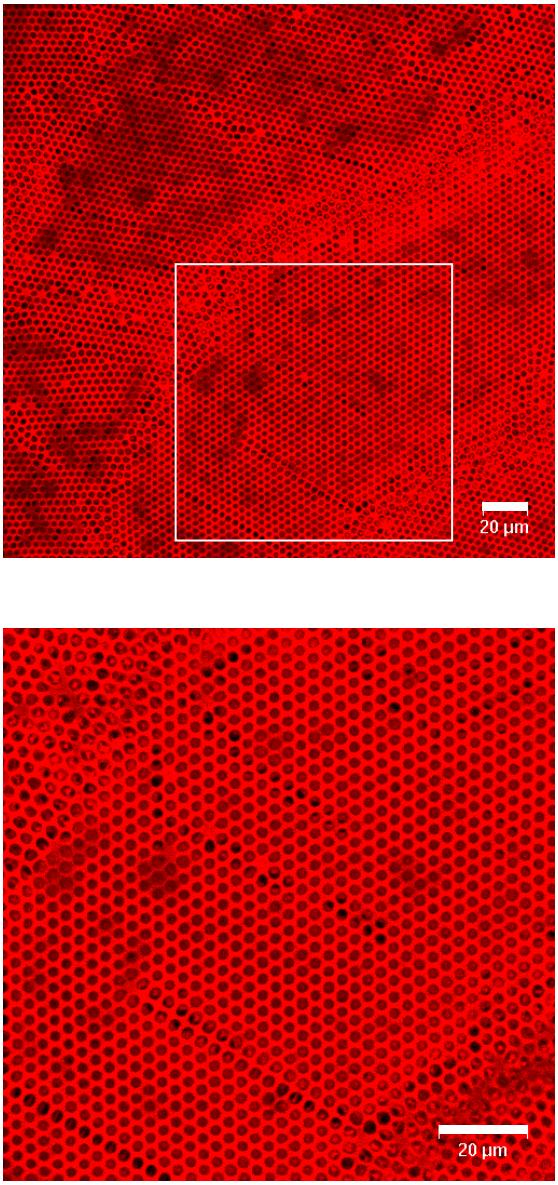

Figure 2.17 A macroporous film made of poly(3-hexylthiophene) (hexPT), cast from carbon disulfide at a concentration of around 0.3 wt. % using Apparatus II. The relative humidity was 84% and the airflow speed was around 70 m/min. The lower image is a zoomed-in of the top image, marked by a white square. Images were taken by a laser scanning confocal microscope (Leica TCS SP, 40× 0.75 dry objective) in fluorescence mode. Scale bar: 20 µm.

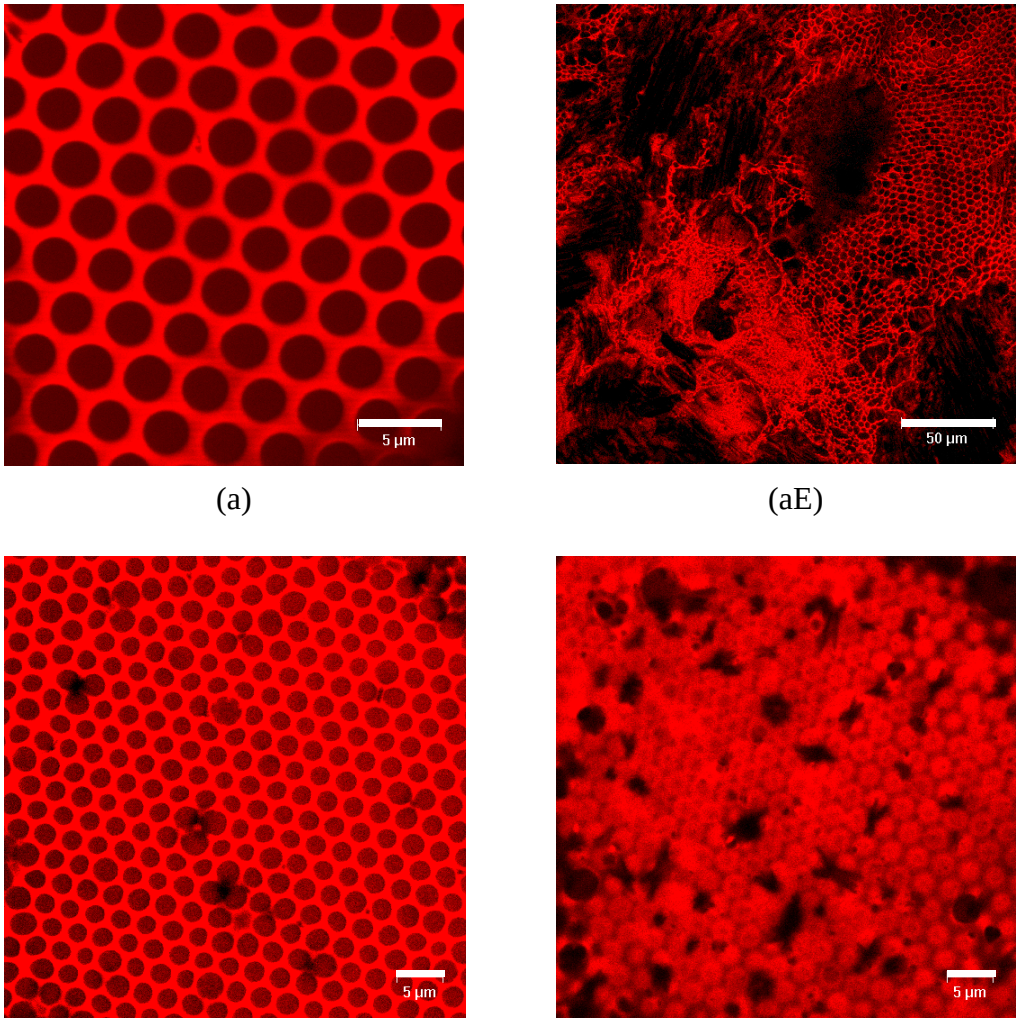

(a) (aE)

(b) (bI)

Figure 2.18 Two macroporous films made of a mixture of poly(3-hexylthiophene) and C_{60}, cast from carbon disulfide in a concentration of about 0.3 wt. % using Apparatus II. The relative humidity was 84% and the airflow speed was around 70 m/min for both films. Images (a) and (aE) are respectively taken at the center and the edge of a film with lower fraction of C_{60}. Images (b) and (bI) are of the other film with relatively higher fraction of C_{60}, taken at the same xy-position but different z-position (i.e., respectively at the surface and the inside) of the film. Images were taken by a laser scanning confocal microscope (Leica TCS SP). (a), (b) and (bI) 100× 1.4 oil objective, scale bar: 5 µm; (aE) 40× 0.75 dry objective, scale bar: 50 µm.

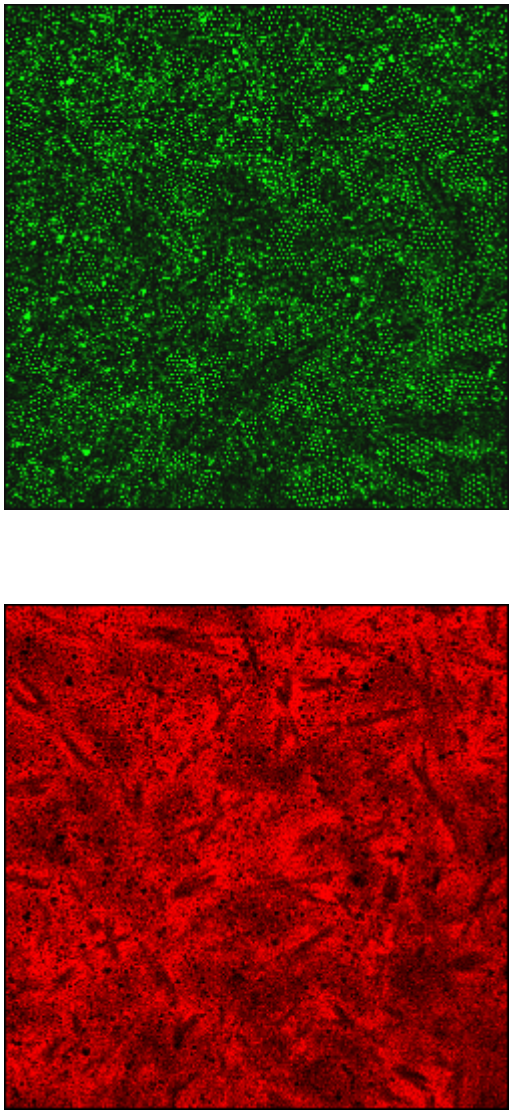

Figure 2.19 Images of the surface of a macroporous film made of polythiophene (hexPT) mixed with increased amount of C_{60}, cast from carbon disulfide in a concentration of about 0.3 wt. % using Apparatus II. The relative humidity was 84% and the airflow speed was around 70 m/min. Images were taken by a laser scanning confocal microscope (Leica TCS SP, 40× 0.75 dry objective) in the reflection mode (the upper one) and fluorescence mode (the lower one). Image size: 250 × 250 μm^2.

2.3.1.3 The Effects of Casting Conditions on Film Morphology

As mentioned in the experimental section, the temperature of the airflow was fixed at room temperature to avoid undesired condensation of water in the apparatus along the airflow path. Here the adjusted experimental conditions include the humidity and speeds of the airflow and the concentration of polymer solutions. Our observations of the effects of these experiment conditions on film morphology are quite similar to those by other researchers [6,12-14].

The humidity needs to be in the right range. It needs to be high enough to ensure condensation of water on the polymer solutions, that is, the dew point of the airflow needs to be above the temperature of the evaporating polymer solutions. When the humidity is too low, solid films without any pore features are obtained. However, too high humidity may lead to coalescence of breath figures with resulting non-ordered film morphology. The exact values of the humidity range depend on the polymer/solvent systems and the airflow speeds. The concentration of polymer solutions needs to be in the right range, too, generally quite low. Beyond that range, the ordered macroporous morphology gradually disappeared. Similarly, the exact values of the concentration range depend on the polymer/solvent systems. With suitable concentration and humidity, the pore size decreased with increased airflow rate.

In fact, there is no exact quantitative relation of air-pore size or film morphology to experimental conditions because the film-formation process is a subtle process accompanied by multiple heat and mass transfer processes and fluid dynamics. The pore size may change from part to part even in one film; generally, edges dried faster, leading to smaller air bubbles and centers dried slower having larger pores (Figure 2.20). The size

difference in one film is sometimes small and sometimes large. Also, these bubble arrays are two–dimensional polycrystals (i.e., composed of a number of single crystals or "grains" with different orientations) and there are always defects, such as point defects and line dislocations. Neither the pore-size difference in a film nor the size and the shape of a grain and various defects are exactly predictable and reproducible.

.

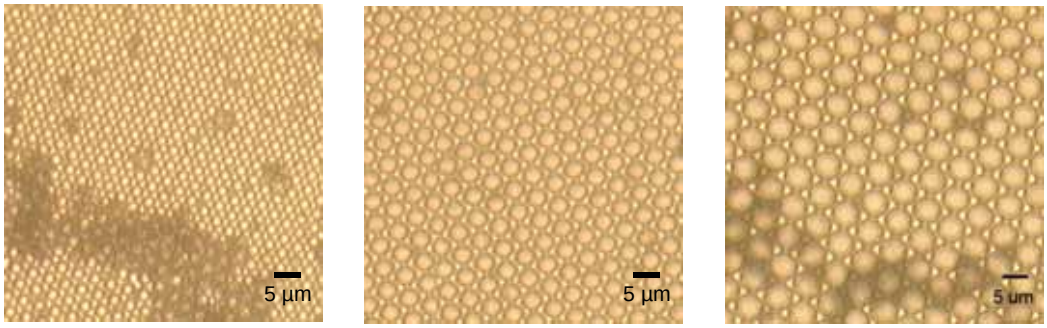

(a) (b) (c)

Figure 2.20 The size of air pores increase from (a) the edge to (c) the center of a macroporous polymer film, (b) a region located in between. The film was cast from a polystyrene/CS_2 solution (PS1c50, 1 wt. %) using Apparatus I (the airflow speed ~ 13.7 m/min). Images were taken by an optical microscope (Leica DMRX, 40× 0.75 dry objective) in transmission mode. Scale bar: 5 µm.

2.3.1.4 Substrate Effect

Films with ordered arrays of air bubbles were also prepared on silicon wafers and water as shown in Figure 2.21. It seemed that the silicon-crystal surfaces had no effect on the formation of the ordered macroporous films. When water was used as a substrate, depending on the surface and interfacial properties of water and the applied polymer solution, the polymer solution totally spread (e.g., polystyrene-benzene solution) or

floated in a lens-like shape (e.g., F8BT-CS_2) on water. The difference between casting a film on a solid substrate such as glass or silicon wafer and on a liquid substrate such as water was that the dried polymer (i.e., after solvent has evaporated) did not get pinned when water was used as a substrate so that the film shrank during the evaporation of the solvent. The shrinkage was more significant for the benzene solution of polystyrene, which can totally spread on the water surface. A corrugated film was left after the solvent totally evaporated from the polystyrene-benzene solution when cast on water. Some small ordered regions were seen between the corrugations.

(a)

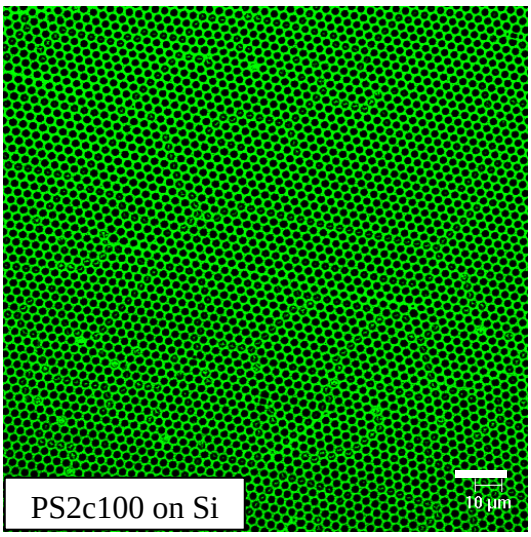

(b)

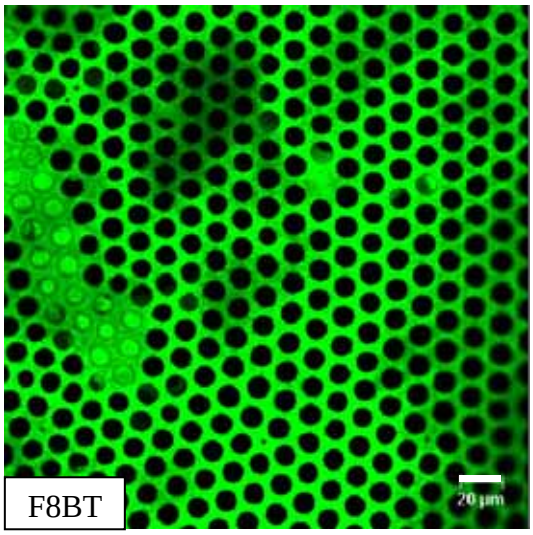

Figure 2.21 Macroporous films prepared on (a) silicon wafer and (b) water with carbon disulfide as a solvent. (a) Film was prepared using Apparatus II (~ 84%RH, airflow speed ~ 240 m/min). (b) Film was prepared in open air in a humid day. Images were taken by a laser scanning confocal microscope (Leica TCS SP). Scale bar: 20 μm.

2.3.2 Three-dimentional Structures of Macroporous Films by LSCM

As discussed in section 2.2, by rejecting most of the out-of-focus light, confocal microscopy images samples at much higher contrast so that true resolution of optical microscopy can be realized (low contrast obscures resolution), especially in the direction parallel to the optical axis, which enables studies of the interior structural details of thick samples. Modern laser scanning confocal microscopes use laser sources to optically section samples and all the images of the sections are combined by computer software to reconstruct 3D images of the samples. Generally, in order to get sharp and non-deformed 3D reconstructed images of a sample by LSCM, the sample has to be fluorescent and robust enough to withstand immersion oil for microscopy. Several conjugated polymers used in our experiments have been found to satisfy these requirements. By looking inside the films via an LSCM, some features which were not seen from the normal optical microscope or the surface scans via an LSCM have been revealed.

2.3.2.1 Connected Large Segments of Air Spheres

From the optical sections of the macroporous films (Figure 2.22a) by the LSCM and the 3D reconstructed images (Figures 2.22b, 2.22c and 2.23b, 2.23c) or the orthogonal-sectioning images by software (Figure 2.23a), it is clear that those holes in the former 2D pictures in Figures 2.8-2.21 are actually spherical pores with their tops open at the surfaces of the films. Although two neighboring air bubbles seem to be separated by a wall of polymer matrix when observed from the top, they actually contact each other and are connected by a small hole inside the film due to the spherical shape. In the case of

tipsPPE, the holes connecting two air pores in contact are actually quite big (Figure 2.23c), resulting in a higher volume fraction of air.

2.3.2.2 Air Bubbles Underneath

For many films made in our experiments, dispersed holes or clusters of holes were found underneath the top ordered arrays of air bubbles. As shown in Figures 2.24 and 2.25, when the laser beam scanned down inside the films, some randomly-dispersed holes of different size or relatively ordered, small arrays of holes almost of the same size showed up below the top layers of air bubbles. Most of the time, a lower pore (pore below the top layer of air bubbles) sat right below the interstice among three closely-packed air bubbles in the top layers to form a closely-packed tetrahedron. Many of the lower pores were found at the grain boundaries where two grains meet.

2.3.2.3 Open Bottom of Air Bubbles in AzidePPE Films

For the macroporous films made of azidePPE, most of the case, air pores with open bottom were observed as shown in Figure 2.26, where Figure 2.26a are the images viewed from the top of the film and Figure 2.26b are from the bottom. Compared with those made from other polymers, where the pores are in shape of spherical segments, the films made of azidePPE have pores which are in shape of spherical layers (a spherical layer is a part of a sphere, included between two parallel planes crossing the spherical surface). Neighbors of these spherical layers of air still contact each other and are connected by small holes.

2.3.2.4 Partially Coalescing Air Bubbles

Occasionally, when the laser beam scanned down into the films, it was found that the neighboring air pores which looked like separate on the surface of the films coalesced inside (Figures 2.27-2.29). This phenomenon was also seen in macroporous films made of ehexPPE.

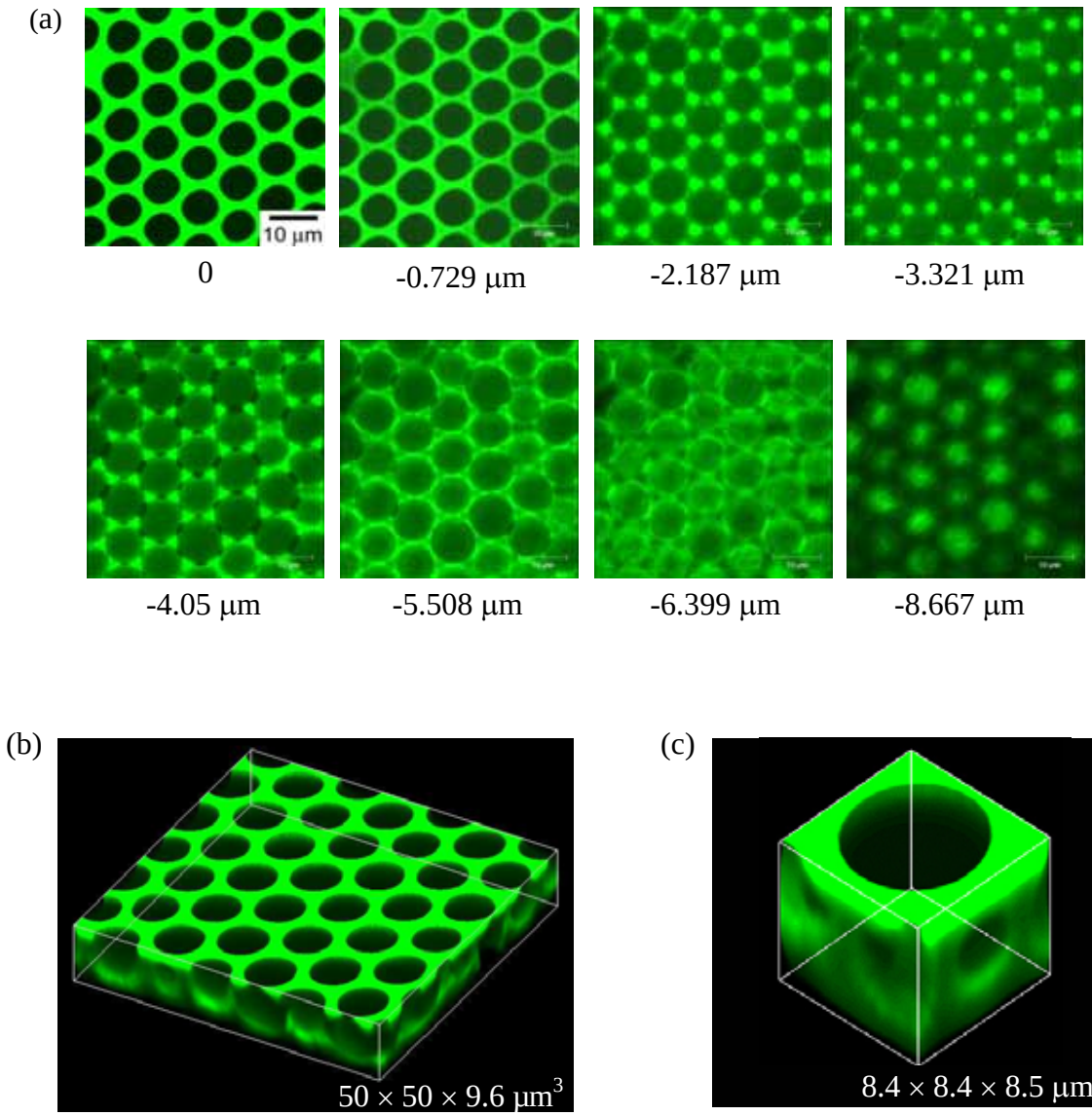

Figure 2.22 Three-dimensional structures of macroporous films of Poly(9,9-dioctylfluorene-co-bithiophene) [F8BT] by a laser scanning confocal microscope (Leica TCS SP, 100× 1.4 oil objective) in fluorescence mode. (a) Optical xy-sections through the thickness of a film from the top to the bottom, where the relative depth is listed below each image. (b) and (c) 3D reconstructed images of film segments. The size of each cube is marked on its image. The films were prepared with carbon disulfide as a solvent using Apparatus II. The relative humidity was 84% and the airflow speed was about 100 m/min.

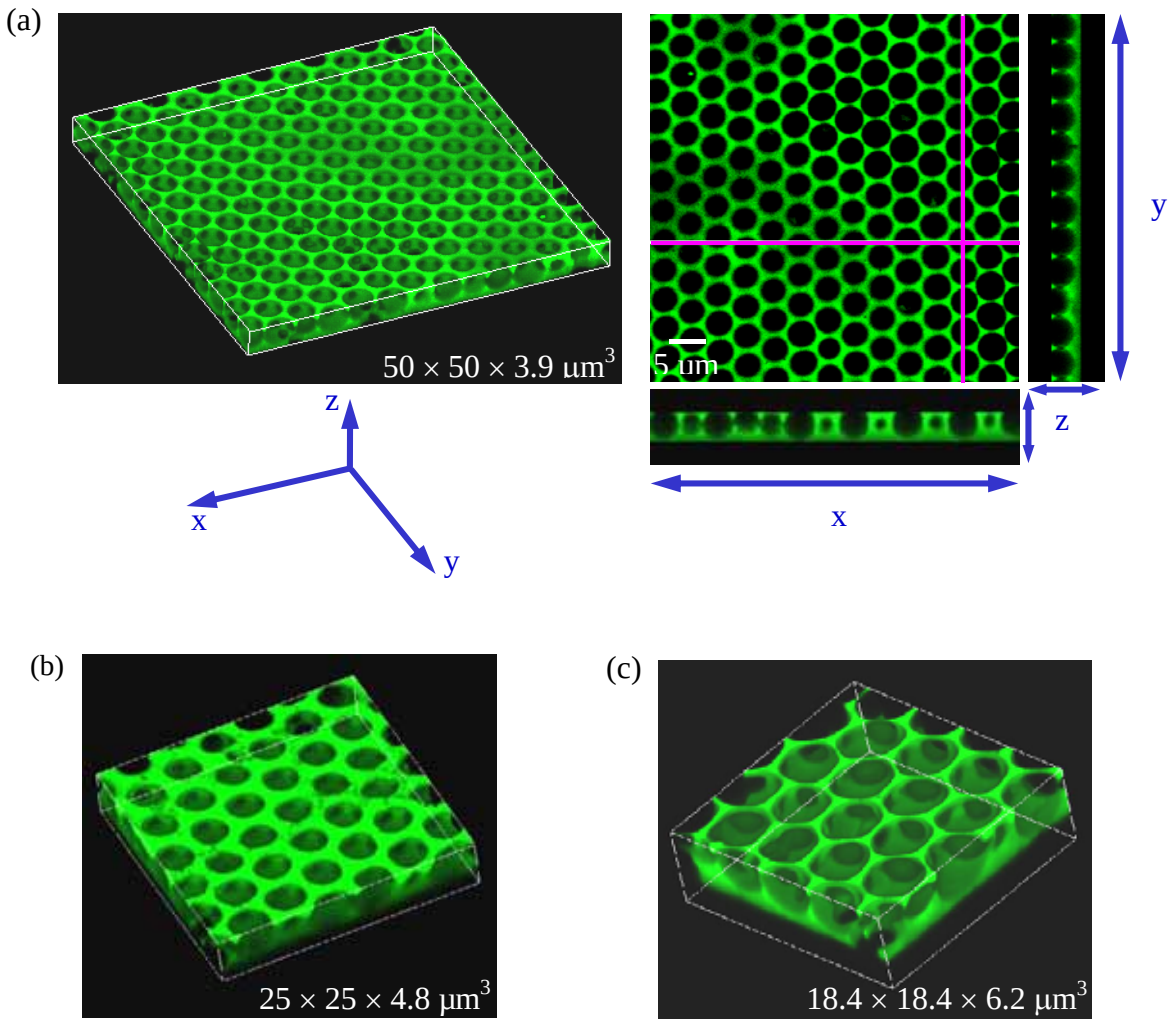

Figure 2.23 Three-dimensional structures of macroporous films of poly[*p*-(phenylene)ethynylene]s (PPEs) by a laser scanning confocal microscope (Leica TCS SP, 100× 1.4 oil objective) in fluorescence mode. (a) 3D reconstructed (left) and the correspondent orthogonal-sectioning (right) images of ehexPPE. In the orthogonal-sectioning image, the xz- and yz-section are taken at the positions marked by the horizontal and vertical red lines on the xy-section, respectively. (b) 3D reconstructed images of hexoPPE. (c) 3D reconstructed images of tipsPPE. The size of every cube is marked on its image. The films were prepared with carbon disulfide as a solvent at a concentration of 0.2-0.5 wt. % using Apparatus II. The relative humidity was 84% for all the three films and the airflow speeds were around (a) 20 m/min, (b) 70 m/min, and (c) 20 m/min, respectively.

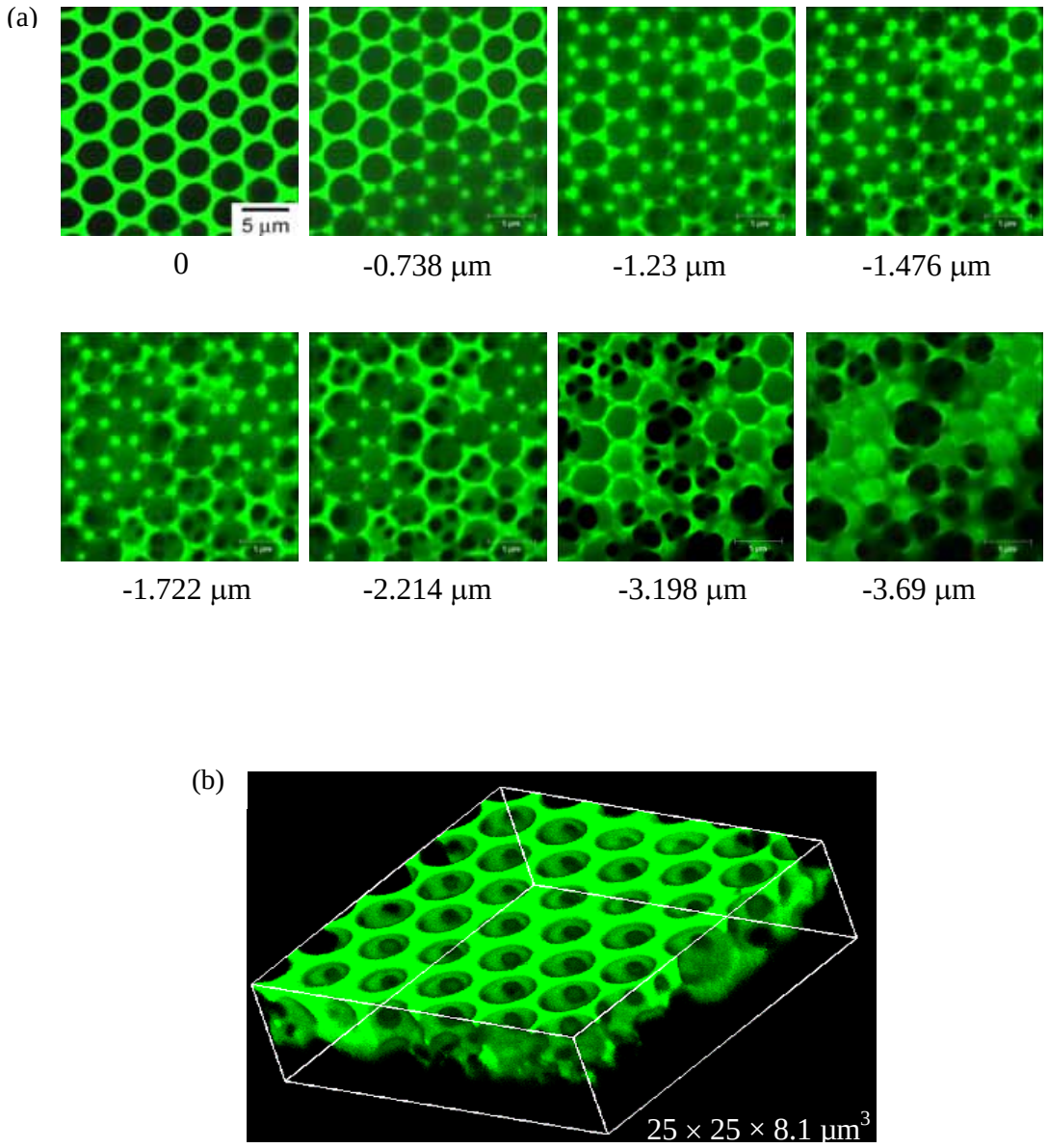

Figure 2.24 Dispersed holes in different size below the top arrays of air bubbles can be observed in some macroporous films. (a) Optical xy-sections of a film (F8T2) through its thickness from the top to the bottom, where the relative depth is listed below each image. (b) 3D-reconstructed image of an ehexPPE film with the cube size marked on the image. The films were prepared with carbon disulfide as a solvent using Apparatus II. The relative humidity was 84% and the airflow speeds were about (a) 180 m/min and (b) 70 m/min. All images were taken by a laser scanning confocal microscope (Leica TCS SP, 100× 1.4 oil objective) in fluorescence mode. Scale bar: 5 µm.

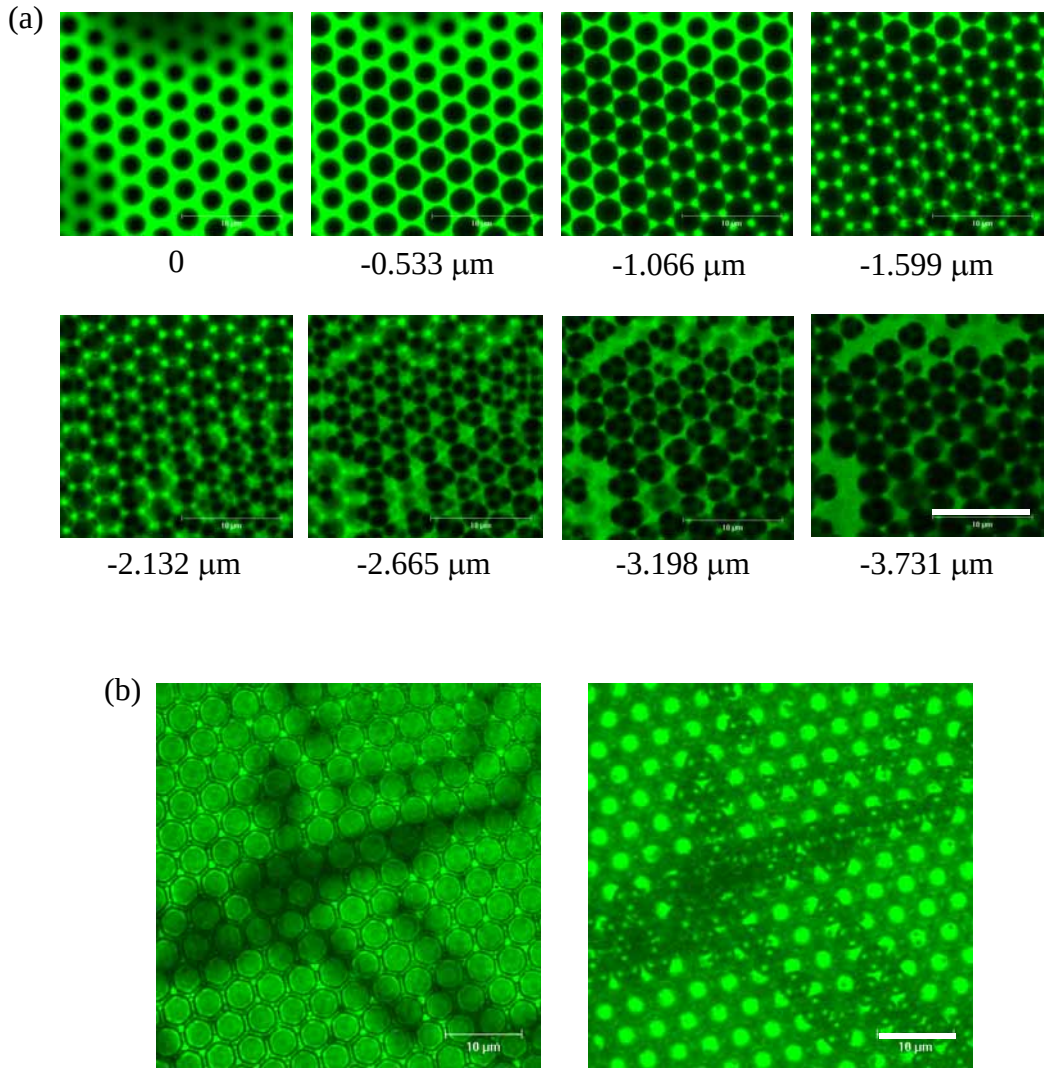

Figure 2.25 Relatively ordered, small arrays of holes below the top arrays of air bubbles can be observed in some macroporous films. (a) Optical xy-sections of a film (azidePPE) through its thickness from the top to the bottom, where the relative depth is listed below each image. (b) Transmitted images of a film made of a blend of polystyrenes (PS2c100/PS1h10, 2:1 by weight), where the left is an image of the top and the right is an image of the inside of the film. The films were prepared with carbon disulfide as a solvent at a concentration of (a) ~ 0.3 wt. % and (b) 1 wt. % using Apparatus II. The relative humidity was 84% for both films and the airflow speeds were around (a) 180 m/min and (b) 240 m/min, respectively. All images were by a laser scanning confocal microscope (Leica TCS SP) in fluorescence mode with an objective of (a) 100× 1.4 oil and (b) 50× 0.75 dry. Scale bar: 10 μm.

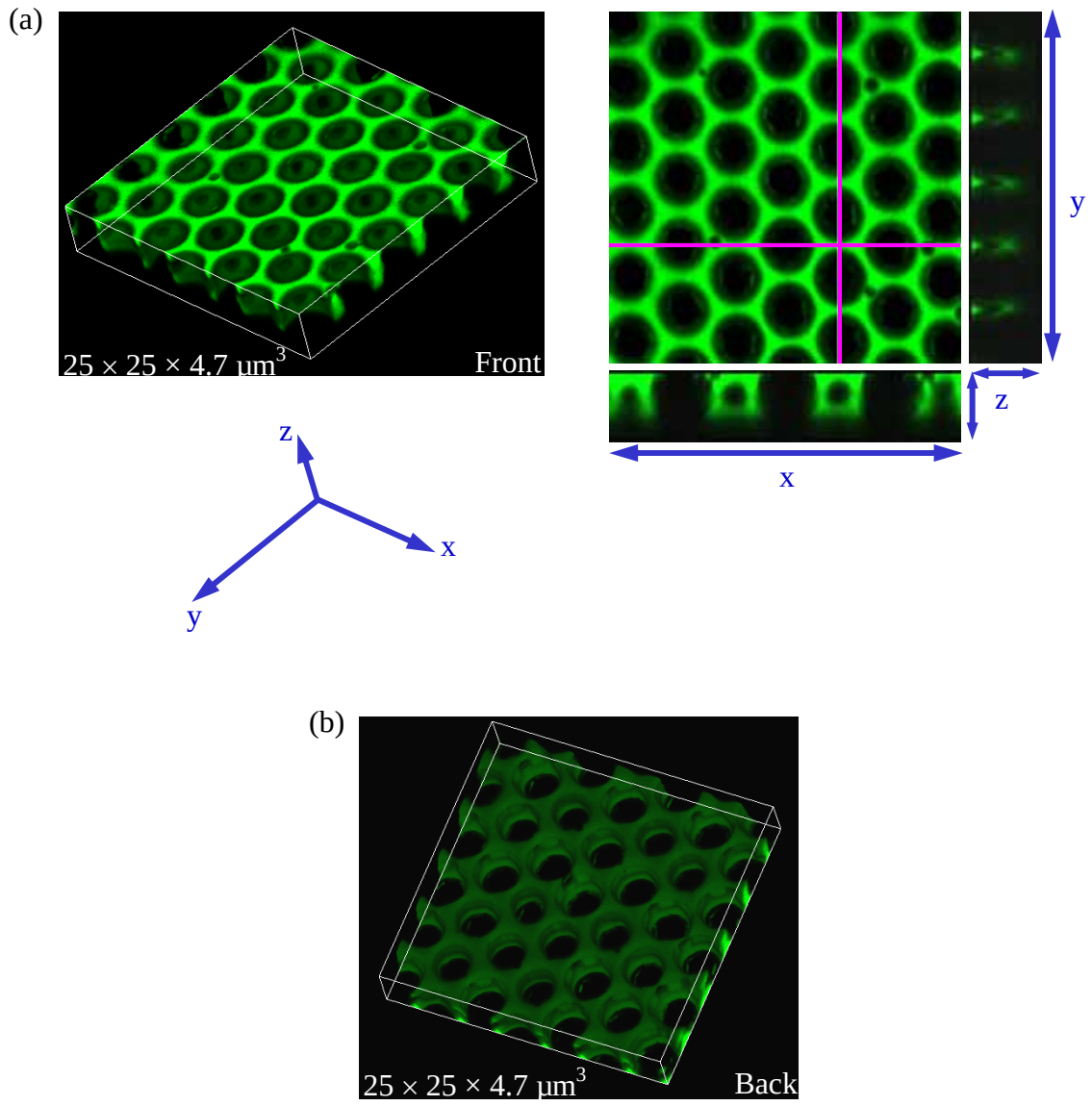

Figure 2.26 Air bubbles in azidePPE films generally have open bottoms. (a) 3D reconstructed image (left) and the correspondent orthogonal-sectioning image (right) of a segment of an azidePPE film, observed from the top. For the right image, the xz-section and yz-section are taken at the positions marked by the horizontal and vertical red lines on the xy-section, respectively. (b) 3D reconstructed image of the same segment observed from the bottom. The size of the cube is marked on its image. The film was prepared with carbon disulfide as a solvent at a concentration of ~ 0.3 wt. % using Apparatus II. The relative humidity was 84% and the airflow speed was around 180 m/min. All images were by a laser scanning confocal microscope (Leica TCS SP, 100× 1.4 oil objective).

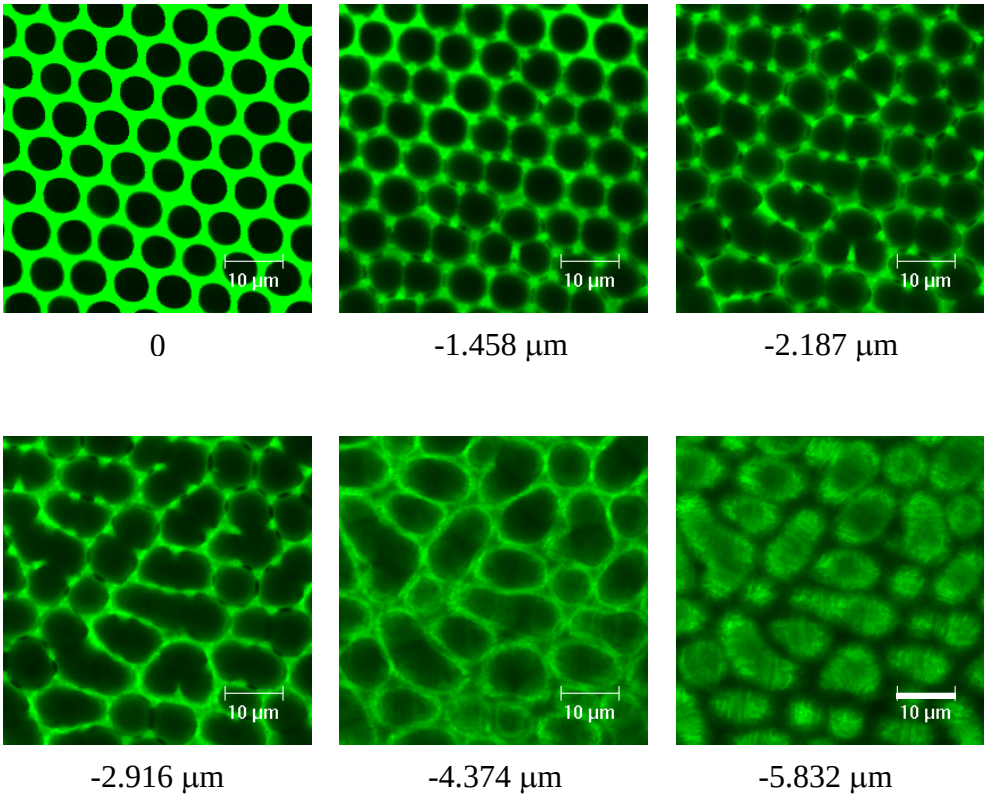

Figure 2.27 Partially coalescing air bubbles can be observed in some macroporous films. Shown here are optical xy-sections of a F8BT film through its thickness from the top to the bottom by a laser scanning confocal microscope (Leica TCS SP, 100× 1.4 oil objective) in fluorescence mode, where the relative depth is listed below each image. Scale bar: 10 µm. The film was prepared with carbon disulfide as a solvent using Apparatus II. The relative humidity was 84% and the airflow speed was around 100 m/min.

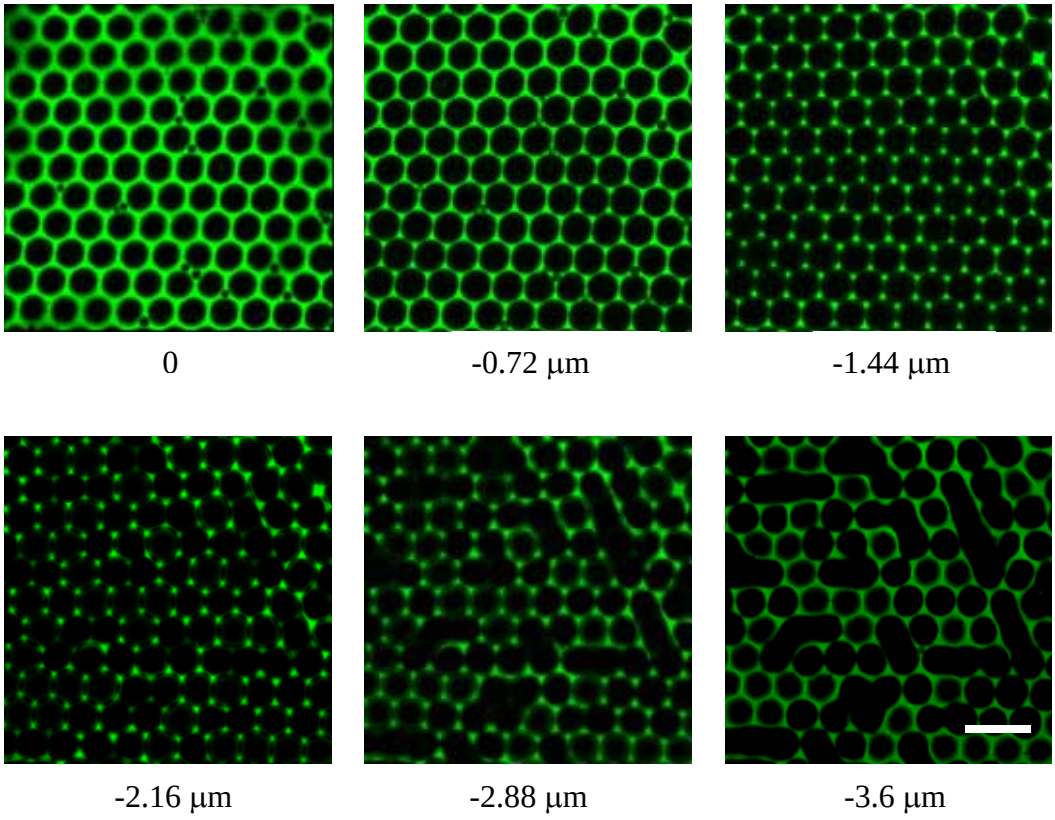

Figure 2.28 Partially coalescing air bubbles can be observed in some macroporous films. Shown here are optical xy-sections of an azidePPE film through its thickness from the top to the bottom by a laser scanning confocal microscope (Leica TCS SP, 100× 1.4 oil objective) in fluorescence mode, where the relative depth is listed below each image. Scale bar: 10 μm. The film was prepared with carbon disulfide as a solvent using Apparatus II. The relative humidity was 84% and the airflow speed was around 180 m/min.

(a)

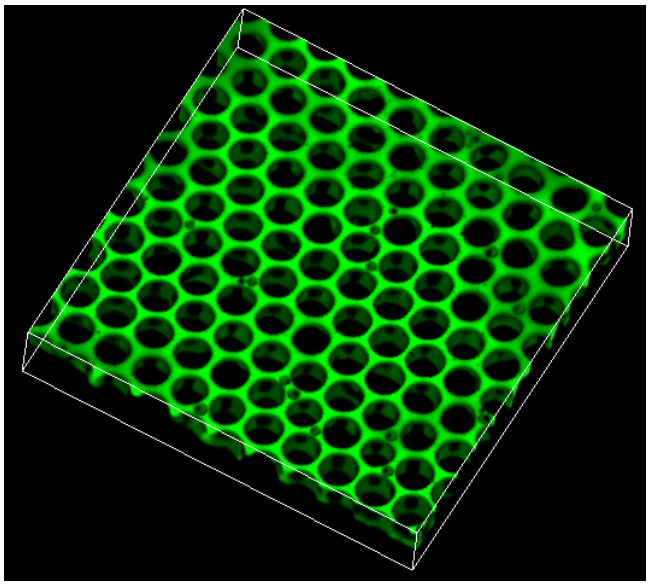

(b)

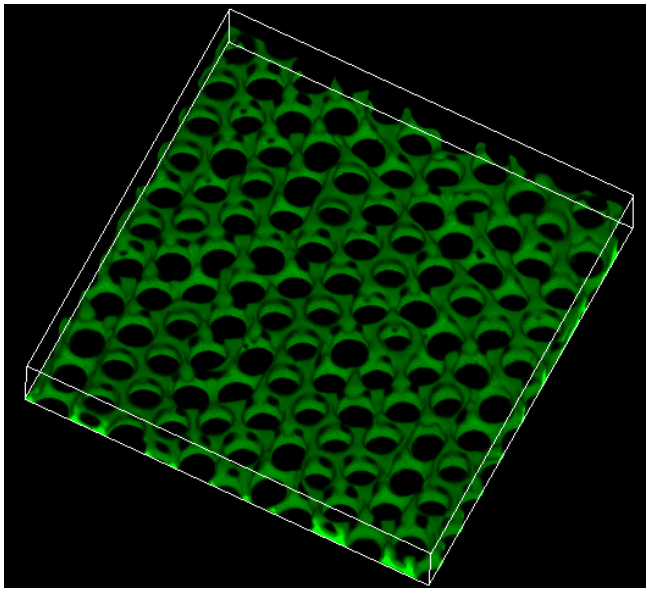

Figure 2.29 Three-dimensional (a) top view and (b) bottom view of a segment of an azidePPE film, whose optical sections (selected) are shown in figure 2.28. It can be seen that some neighboring pores are partially coalesced from the bottom view. Images were taken by a laser scanning confocal microscope (Leica TCS SP, 100× 1.4 oil objective) in fluorescence mode. Cube size: $50 \times 50 \times 8\ \mu m^3$.

2.4 Discussion

2.4.1 Equilibrium Shape and Position of Condensed Water

As indicated by the 3D structure of the macroporous films via LSCM, the air bubbles in a film are large segments of air spheres with top open at the surface. If they formed with condensed water droplets as templates, a water droplet on the polymer solution, right before the solvent has totally evaporated, should have the same shape as the corresponding air bubble (assuming no obvious deformation/shrinkage of the polymer film upon final drying) as we observed in the microscopic 3D images. Therefore we can infer that the water droplet was in a "lens" shape (i.e., the three phases — water, solution and air are in mutual contact) [22] suspended on the solution surface (Figure 2.30a) when the solution was about to dry up.

The equilibrium shape and position of a liquid lens on an immiscible liquid surface is determined by a balance between gravity, buoyancy and surface (or interfacial) tension forces [22,23]. For a drop with a size of several microns, the surface tension forces experienced by the drop are much larger than gravity, so that the gravitational effects can be neglected for a rough estimate of the drop shape [22,24]. (Note that gravity does exist; just because it is much smaller than the surface tension forces, when both of them are applied on the droplet, the effect of gravity will be concealed by that of surface tension forces.) As pointed out in Ref. 22, without gravity, the liquid surface will be flat up to the perimeter of the lens and the upper and lower surfaces of the lens are spherical, so that the angles between interfaces, θ_{12} and θ_{13} (see Figure 2.30a), are related to the interfacial tensions by simple equations [22]

$$\cos\theta_{12} = \frac{1+(\gamma_{12}/\gamma_{23})^2 - (\gamma_{13}/\gamma_{23})^2}{2\gamma_{12}/\gamma_{23}} \tag{2.2}$$

and

$$\cos\theta_{13} = \frac{1+(\gamma_{13}/\gamma_{23})^2 - (\gamma_{12}/\gamma_{23})^2}{2\gamma_{13}/\gamma_{23}} \quad , \tag{2.3}$$

where, γ_{12} , γ_{23} and γ_{13} are the interfacial tension between liquid lens and liquid substrate, between liquid substrate and air, between liquid lens and air, respectively.

In our case, a solution is mainly composed of a solvent (carbon disulfide or benzene), with only a very small amount of polymer (about or less than 1 wt. %). Because data of the interfacial properties of the solvents are available in literature [25,26], we can first look at a system of a water droplet at a pure-solvent surface so that the three phases are water (phase 1), pure solvent (phase 2) and air (phase 3). In the case with carbon disulfide as a substrate, the three interfacial tensions, γ_{12} , γ_{23} and γ_{13}, are 48.4 dynes/cm, 32 dynes/cm and 72.75 dynes/cm at 20 °C, respectively [26]. According to Eqs. (2.2) and (2.3), the angles are calculated to be 128.4° for θ_{12} and 31.4° for θ_{13}, so that a water droplet will have a large segment below the liquid solvent surface, which matches the shape of the observed air pores quite well. Pitois and François [27] observed similar shape and position of a water drop (in a diameter of about 2 mm) when they placed it into a reservoir of cold pure CS_2 (they did not give the exact temperature of the CS_2). However this is still just a rough estimate because the existence of a small amount polymer in the liquid substrate might have a large effect on the interfacial tensions.

When pure benzene is the substrate, the three interfacial tensions, γ_{12} , γ_{23} and γ_{13}, are 35 dynes/cm, 28.8 dynes/cm and 72.75 dynes/cm at 20 °C, respectively. In this case,

γ_{13} is larger than ($\gamma_{12} + \gamma_{23}$) by 9 dynes/cm, so that benzene should totally cover the top of the water droplets given enough time. Then gravity takes control and, since water has a larger density than benzene (ρ_{ben} = 0.88 g/ml), these water droplets inside benzene will sink to the bottom eventually [20]. Similarly, this is just a rough estimate.

If γ_{13} is still larger than ($\gamma_{12} + \gamma_{23}$) when a small amount of polymer was dissolved in the benzene substrate, three-dimensional arrays of air bubbles are possible as observed by Srinivasarao et al. [20]. However, as will be discussed in Chapter 5, capillary forces probably contribute to the two-dimensional packing when carbon disulfide was used as a solvent; when benzene was used as a solvent, a new mechanism is required to explain the 3D packing inside the solution. The whole process gets more subtle and complicated, especially when there is strong convection in the bulk (which is very possible for our fast-evaporating solutions); the water droplets in the bulk solution probably are more prone to convection because there is no surface tension to hold them. This might be a reason that the macroporous film prepared with benzene as a solvent is less ordered than that made of carbon disulfide.

As seen in Figure 2.9, there are often bright spots (as marked by blue dashed circles) observed in the films cast with benzene as a solvent under an optical microscope in transmission mode. It was found that they were concave regions at the bottom when the film was viewed from the bottom. They were probably the imprints of the water droplets which sank into the solution, coalesced and attached to the glass surface. Light passed through a thinner polymer layer at those regions so that they looked brighter.

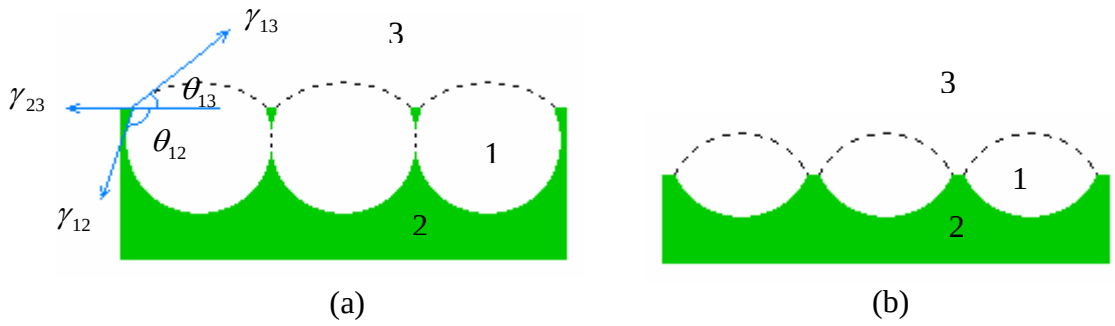

Figure 2.30 (a) Schematic of a cross-section of a macroporous film observed via LSCM. The dashed arcs are the inferred water-air interfaces before the film totally dried with γ_{12}, γ_{23} and γ_{13} being the three interfacial tensions, where phase 1, 2 and 3 are respectively water, polymer solution and air. (b) Schematic of a possible shape of pores in a macroporous film by condensing another liquid instead of water. Similarly, the dashed arcs are the inferred interfaces between the liquid lenses and air. In this case, the surface tension of the condensed liquid, γ_{13}, should be smaller than that of the polymer solution, γ_{23}.

Since the ordered arrays of air bubbles are the inverse of breath figures (i.e., patterns of condensed water droplets), to obtain macroporous films in a similar way by templating the condensation patterns of another vapor instead of water, firstly, the vapor has to be able to condense, drop-wise, which depends on the surface and interfacial tensions of the three phases (polymer solution, air and condensed liquid) [22]. The shape of the condensed liquid lenses will also have an effect on the order of the pores. As seen in our studies and in the literature [1-6,14,19-21,27,30-32], in principle, the pores are large segments of air spheres as sketched in Figure 2.30a, not the case in Figure 2.30b. This seems to be reasonable because, when they meet, two liquid lenses in a shape as depicted in Figure 2.30b will merge more easily and faster than those in a shape as in Figure 2.30a. A thin layer of substrate liquid (i.e., a polymer solution) needs to be

depleted out of the interstice between two apparently contacting droplets in the later case, which takes time and the depleting speed decreases with the thinning of the separating solution layer [23,28,29].

2.4.2 Hypothesis for the Origin of the Connecting Holes

In our case, the pores were found to be connected by small holes via LSCM. As discussed in Chapter 1, silimar structures were observed by Srinivasarao et al. [20] and Boer et al. [30] via SEM, while the neighboring pores were found to be separated by polymer walls without connecting holes in the films prepared by Hayakawa and Horiuchi [31] via SEM and by Böker et al. [32] via TEM. The different results by different researchers are probably due to different material systems and/or the preparation conditions.

For the origin of the connecting holes as in our case, a possible explanation can be given by considering the temperature effects on water density. Since water has a maximum density at 3.97 °C under atmospheric pressure [30], when the temperature of water droplets is higher than 3.97 °C, the density decreases with increasing temperature, thus the volume of the droplets increases. At the final stage of a film-formation process, solvent has totally evaporated macroscopically, the temperature of the film (which is filled with water droplets) goes back to the room temperature, leading to the swelling of the water droplets, puncturing the very thin layer of polymer between two water droplets if there are still any.

2.4.3 Comments on the Special Features Observed in 3D Structures

The dispersed, less-ordered holes or small arrays of holes below the top ordered arrays of air bubbles (Figures 2.24 and 2.25) are the reason that some areas in a porous film looked darker when observed under a microscope in the transmission mode (Figures 2.8, 2.20 and 2.25b). More light was scattered due to these holes underneath.

As discussed in Chapter 1, Widawski et al. [1] and Hayakawa and Horiuchi [31] also sometimes obtained multilayered macroporous films with carbon disulfide as a solvent. Similarly to our case, as pointed out in Ref. 27, the lower layers obtained were usually discontinuous and not always well-ordered. Besides, Shah et al. [21] obtained multilayered porous films from Freon (1,1,2-trichlorotrifluoroethane). Both carbon disulfide and Freon are denser than water, so that density effect as in the case when benzene or toluene is used as a solvent [20] should not be responsible for the formation of these lower holes. (According to Srinivasarao et al. [20], when a film was cast from benzene or toluene, due to the density of the solvent is less than that of condensed water, water droplets finally sank into the solution.) The origin of the lower holes in our films was revealed by *in situ* recording the film formation processes (i.e., the evolution of breath figures on the evaporating polymer solutions) via a microscope coupled with a high-speed camera and replaying the recordings at lower speeds. The details will be discussed in Chapter 5.

The open-bottom pores in azidePPE films indicate that the templates, i.e., the condensed water droplets, are in contact with the glass substrates. For this to happen, a water droplet needs to deplete a layer of azidePPE-CS_2 solution between it and the glass substrate, indicating that it is a favorable situation for water to contact the glass surface.

Considering the interfacial tensions between the three phases (water, the azidePPE-CS_2 solution and glass), there are two possibilities — one is that the interfacial tension between water and the polymer solution is very high and the other is that the interfacial tension between the polymer solution and glass is very high. However, the 3D images of azidePPE films (see Figure 2.26) indicate that the azidePPE-CS_2 solution tends to cover the water droplets at the top so that the interfacial tension between water and the polymer solution should be quite low. Therefore, we can infer that the interfacial tension between the azidePPE-CS_2 solution and glass is probably very high so that water droplets tend to replace the solution to form water-glass interface of a lower interfacial tension instead of solution-glass interface. In addition, the small thickness of the polymer films should be helpful for the water droplets to contact the glass substrates.

From the partially coalesced pores, we can infer that the coalescence events should take place at the time when the concentration of a polymer solution is very high so that two water droplets in contact can only break a part of the polymer solution wall separating them. As will be seen in Chapter 5, the coalescence between neighboring water droplets was seen at a very late stage right before the structure was vitrified.

2.4.4 Effect of Polymer on the Film Morphology

The results of our experiment (with the same solvent, i.e., carbon disulfide) seem to suggest that the nature of polymer affects the film morphology. First, some polymers seem to be able to form ordered macroporous films (e.g., carboxyl-terminated polystyrenes, polyfluorene copolymers, hexyl-polythiophene and several poly[*p*-(phenylene)ethynylene]s) and some not (e.g., hydroxyl-terminated polystyrenes,

polystyrene standards and polyfluorene homopolymer). Secondly, among the polymers which can form ordered morphologies, some (e.g., PS2c25, PS2c100, hexoPPE, azidePPE) seem to have larger ordered grains and fewer defects than others (e.g., PS2c50, PS1c50, F8T2 and ehexPPE). Thirdly, some polymers (e.g., F8T2 and ehexPPE) seem to have more lower-layer pores. Finally, azidePPE generally gives pores with open bottom, different from others. The details about how the nature of polymer affects the film morphology are still not clear. We have tried to measure the end groups of the polystyrenes using IR (infrared) and ^{1}H NMR (Nuclear Magnetic Resonance) since the end groups seem to dictate whether the ordered macroporous structure forms or not. However, due to the very low amount of the end groups in polymers, they were not detected (i.e., the polystyrenes with various end groups gave the same IR and NMR spectra).

As mentioned in Chapter 1, there are mainly two opinions about where the growth and the packing of the condensed water droplets take place; one is on the surface of a polymer solution (i.e., the water droplets are suspended on the solution surface) [6,19,21,27,34] and the other is above the solution surface (i.e., the water droplets are hovering above the rapidly-evaporating solution) [20]. In the first case, the interfacial property of the polymer at the water/solvent interface should be the key factor for the film morphology [6,19,21,27,34], while, in the second case, the effect of the polymer on the evaporation of the solvent is probably the key [20]. Therefore, to find out how the nature of the polymer affects the film morphology, we also need to figure out how the breath figure grows.

With the opinion that the water droplets are suspended on the solution surface during their growth and packing, Pitois and François [27] further attributed the formation of ordered porous films to the star-shape of polymer molecules and/or the ability of a polymer to form star-like micelles in solution. However, our experimental results and those by other researchers [19-21,31,32,34] have clearly shown that ordered macroporous films can be prepared from polymers which do not have star molecular-shape and do not form star-like micelles in solution.

2.5 Conclusions

In conclusion, we have prepared well-ordered macroporous films out of linear polystyrenes and their blends, and conjugated polymers. Optimal preparation conditions were found. The morphology of these films was studied in detail via optical microscopy. By using a laser scanning confocal microscope, many three-dimensional features of the macroporous films were revealed. Based on the morphology of the films, possible film-formation processes in different polymer/solvent systems were conjectured, with the assumption that the morphology seen in the finished films corresponds to the breath figures formed on the solutions at the final stage. The experimental results seem to suggest that the nature of polymer used has an effect on the film morphology, but the details are still not clear. However, the discovery of several polymers which do not have star shape and do not form star-like micelles in solutions excluded the hypothesis by Pitois and François [27] that star shape of polymers is the key to the formation of ordered macroporous films by this moist-casting method.

2.6 Recommendations

From the discussion, it can be concluded that the interfacial tension between water and a polymer solution can be an important factor affecting the final morphology of a macroporous film. Therefore, it will be helpful to study the interfacial properties including spreading coefficients of the polymer solutions on water.

References:

[1] G. Widawski, M. Rawiso and B. François, "Self-organized honeycomb morphology of star-polymer polystyrene films", *Nature* **369**, 387 (1994).

[2] B. François, O. Pitois and J. François, "Polymer films with a self-organized honeycomb morphology", *Adv. Mater.* **7**, 1041 (1995).

[3] B. François, Y. Ederlé and C. Mathis, "Honeycomb membranes made from $C_{60}(PS)_6$", *Synth. Met.* **103**, 2362 (1999).

[4] B. de Boer, U. Stalmach, H. Nijland and G. Hadziioannou, "Microporous honeycomb-structured films of semiconducting block copolymers and their use as patterned templates", *Adv. Mater.* **12**, 1581 (2000).

[5] M. H. Stenzel-Rosenbaum, T. P. Davis, A. G. Fane and V. Chen, "Porous polymer films and honeycomb structures made by the self-organization of well-defined macromolecular structures created by living radical polymerization techniques", *Angew. Chem. Int. Ed.* **40**, 3428 (2001).

[6] M. H. Stenzel, "Formation of regular honeycomb-patterned porous film by self-organization", *Aust. J. Chem.* **55**, 239 (2002).

[7] J. H. Burroughes, D. D. C. Bradley, A. R. Brown, R. N. Marks, K. Mackay, R. H. Friend, P. L. Burns and A. B. Holmes, "Light-emitting diodes based on conjugated polymers", *Nature* **347**, 539 (1990).

[8] T. Piok, S. Gamerith, C. Gadermaier, H. Plank, F. P. Wenzl, S. Patil, R. Montenegro, T. Kietzke, D. Neher, U. Scherf, K. Landfester and E. J. W. List, "Organic light-emitting devices fabricated from semiconducting nanospheres", *Adv. Mater.* **15**, 800 (2003).

[9] F. Garnier, R. Hajlaoui, A. Yassar and P. Srivastava, "All-polymer field-effect transistor realized by printing techniques", *Science* **265**, 1684 (1994).

[10] M. Willander, A. Assadi and C. Svensson, “Polymer based devices their function and characterization”, *Synth. Met.* **57**, 4099 (1993).

[11] N. S. Sariciftci, L. Smilowitz, A. J. Heeger and F. Wudl, “Photoinduced electron transfer from a conducting polymer to bulkminsterfullerene”, *Science* **258**, 1474 (1992).

[12] M. Granström, K. Petritsch, A. C. Arias, A. Lux, M. R. Andersson and R. H. Friend, “Laminated fabrication of polymeric photovoltaic diodes”, *Nature* **395**, 257 (1998).

[13] A. C. Partridge, P. Harris and M. K. Andrews, “High-sensitivity conducting polymer sensors”, *The Analyst* **121**, 1349 (1996).

[14] L. Song, R. K. Bly, J. N. Wilson, S. Bakbak, J. O. Park, M. Srinivasarao and U. H. F. Bunz, “Facile microstructuring of organic semiconducting polymers by the breath figure method: hexagonally ordered bubble arrays in rigid-rod polymers”, *Adv. Mater.* **16**, 115 (2004).

[15] R. S. Longhurst, *Geometrical and Physical Optics*, 2nd Ed. (Longman Group LTD London, 1967), Ch.3 & Ch.14.

[16] S. G. Lipson, H. Lipson, and D. S. Tannhauser, *Optical Physics*, 3rd Ed. (Cambridge University Press, Cambridge, 1995), Ch.3 & Ch.12.

[17] D. B. Murphy, Fundamentals of Light Microscopy and Electronic Imaging (Wiley-Liss New York, 2001), Ch1 & Ch12.

[18] R. H. Webb, “Confocal optical microscopy”, *Rep. Prog. Phys.* **59**, 427 (1996).

[19] O. Karthaus, M. Shimomura, X. Cieren, M. Shimomura, H. Hasegawa and T. Hashimoto, “Water-assisted formation of micrometer-size honeycomb patterns of polymers”, *Langmuir* **16**, 6071 (2000).

[20] M. Srinivasarao, D. Collings, A. Philips and S. Patel, “Three-dimensionally ordered array of air bubbles in a polymer film”, *Science* **292**, 79 (2001).

[21] P. S. Shah, M. B. Sigman, Jr., C. A. Stowell, K. T. Lim, K. P. Johnston and B. A. Korgel, “Single-step self-organization of ordered macroporous nanocrystal thin films”, *Adv. Mater.* **15**, 971 (2003).

[22] H. M. Princen, “The equilibrium shape of interfaces, drops, and bubbles. Rigid and deformable particles at interfaces”, in *Surface and Colloid Science*, edited by E. matijevic, Vol. 2, (Wiley-Interscience, New York, N. Y.) 1969.

[23] A. Steyer, P. Guenoun and D. Beysens, “Hexatic and fat-fractal structures for water droplets condensing on oil”, *Phys. Rev. E* **48**, 428 (1993).

[24] C. M. Knobler and D. Beysens, “Growth of breath figures on fluid surfaces”, *Europhys. Lett.* **6**, 707 (1988).

[25] I. M. Smallwood, *Handbook of organic solvent properties* (Arnold, London, 1996).

[26] http://www.nisc.com/cis/samples/chris.htm#hl_1, CIS ID: CH-00000314.

[27] O. Pitois and B. François, “Formation of ordered micro-porous membranes”, *Eur. Phys. J. B* **8**, 225 (1999).

[28] A. Steyer, P. Guenoun, D. Beysens and C. M. Knobler, “Two-dimensional ordering during droplet growth on a liquid surface”, *Phys. Rev. B* **42**, 1086 (1990).

[29] D. Beysens, A. Steyer, P. Guenoun, D. Fritter and C. M. Knobler, “How does dew form”, *Phase Transitions* **31**, 219 (1991).

[30] B. de Boer, U. Stalmach, H. Nijland and G. Hadziioannou, “Microporous honeycomb-structured films of semiconducting block copolymers and their use as patterned templates”, *Adv. Mater.* **12**, 1581 (2000).

[31] T. Hayakawa and S. Horiuchi, “From angstroms to micrometers: self-organized hierarchical structure within a polymer film”, *Angew. Chem. Int. Ed.* **42**, 2285 (2003).

[32] A. Böker, Y. Lin, K. Chiapperini, R. Horowitz, M. Thompson, V. Carreon, T. Xu, C. Abetz, H. Skaff, A. D. Dinsmore, T. Emrick and T. P. Russell, “Hierarchical nanoparticle assemblies formed by decorating breath figures”, *Nat. Mater.* **3**, 302 (2004).

[33] P. G. Debenedetti, “Supercooled and glassy water”, *J. Phys.: Condens. Matter* **15**, R1669 (2003).

[34] A. Mourran, S. S. Sheiko and M. Möller, “Vitrified condensation pattern in thin polymer films: New approach for micropatterning”, *PMSE Proceedings of the Am. Chem. Soc.* **81**, 426 (1999).

CHAPTER 3

CHARACTERIZATION OF TWO-DIMENSIONAL ORDER

One of the reasons that the macroporous films are interesting is the highly-ordered nature of the bubble arrays, i.e., pores are uniform in size and hexagonally packed on the film surfaces. Hence it is useful to characterize the order of the films. In the following, three methods have been used to characterize the order — Fraunhofer diffraction in reciprocal space, Voronoi diagram and bond-orientational correlation function in real space. These characterizations are helpful for further control of the structure formation and quantifying material/device properties as a function of the order of the structured films.

3.1 Fraunhofer Diffraction

Because of its wave nature, a beam of light will bend around the edge of obstacles whose dimensions are comparable to the wavelength of the light. This phenomenon is called diffraction [1]. Fraunhofer diffraction happens when a beam of parallel light is incident onto an obstacle, and the diffraction can be observed at infinity [1]. In practice, lenses are generally used for the observation of the resultant diffraction patterns [1]. Mathematically, Fraunhofer diffraction performs a spatial Fourier transform with positions in the diffraction space corresponding to diffracted angles (angle between the incident beam and the diffracted beams) in the real space. Although the diffraction pattern of a random object can be quite complicated, a highly ordered periodic structure (grating) forms a well-defined diffraction pattern which is correlated to the original

periodic structure by a simple "grating equation" or sometimes called "two-dimensional Bragg's law".

$$m\lambda = n\, d_{hk} \sin\theta, \tag{3.1}$$

where, m is the order of the diffraction maxima, m = 0, 1, 2, …, λ is the wavelength of the incident light, n is the refractive index of the dispersion medium, d_{hk} is the lattice spacing and θ is the diffraction angle. Thus Fraunhofer diffraction is a convenient way to characterize the degree of order of a two-dimensional array and estimate the average feature size [1-3].

Here we use a transmission optical microscope (Leica DMRX, 40× 0.75 dry objective) coupled with a CCD camera (Sony DKC5000) to obtain the direct-space images of our macroporous films and, with the help of a Bertrand lens, their correspondent Fraunhofer diffraction patterns. An interference filter (the central wavelength λ = 532 ± 2 nm, FWHM = 10 ± 2 nm) is added to give an illumination of near monochromatic light and the aperture diaphragm is closed down to the minimum to provide a well-collimated, normal-incident light at the sample plane.

A schematic of the light path in an optical microscope is given in Figure 3.1. When well-collimated light is normally incident onto a sample, the parallel light beams diffracted at different angles are converged by an objective to its back focal plane, forming a Fraunhofer diffraction pattern of the sample. Then the converged light propagates further and interferes at the intermediate image plane (i.e., the eyepiece diaphragm plane) to form the real-space image of the sample that can be observed from an eyepiece or photographed by a camera. In order to observe/photograph the corresponding diffraction pattern, a Bertrand lens is inserted into the optical path between

the back focal plane of the objective and the intermediate image plane so that the image of the diffraction pattern forms at the intermediate image plane.

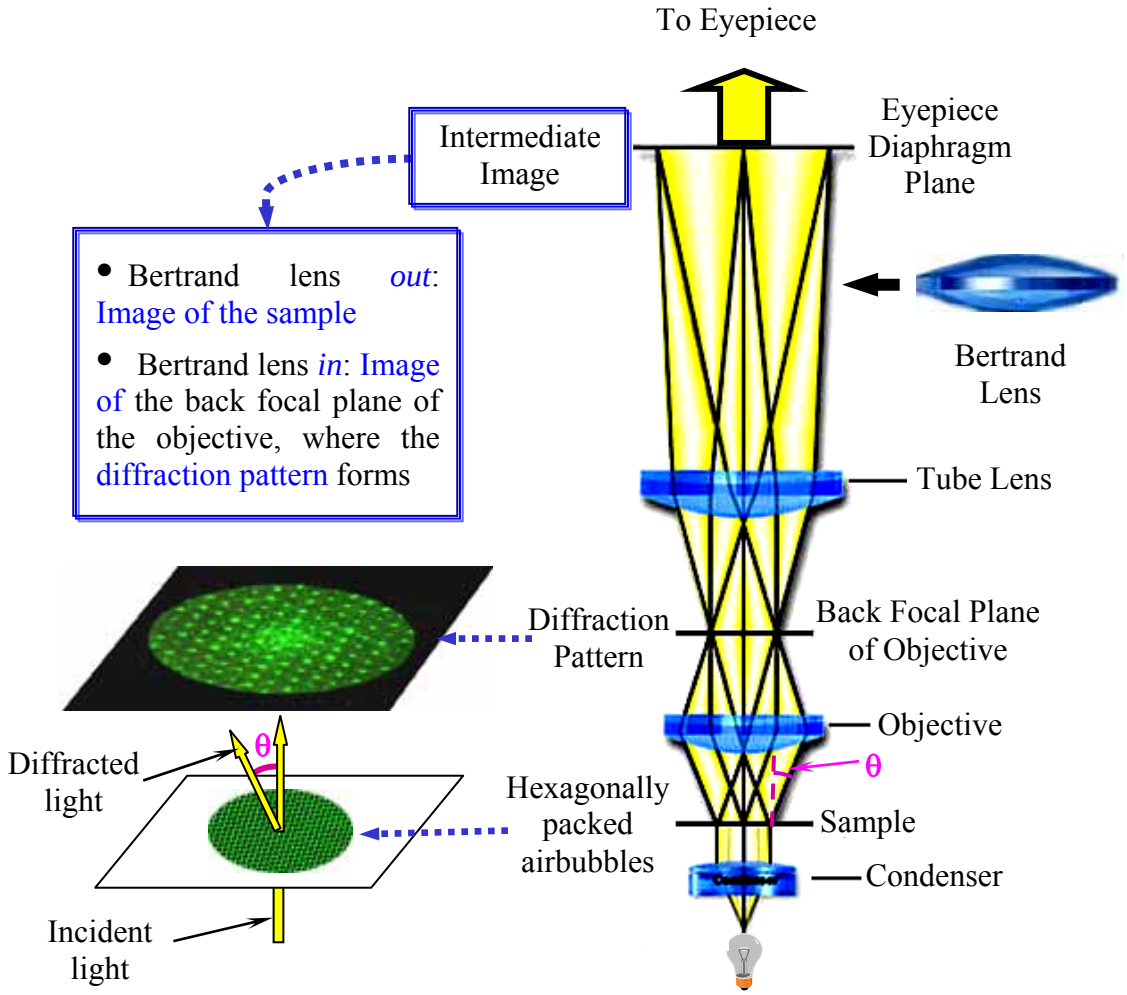

Figure 3.1 Schematic of image formation in a transmitted optical microscope. The yellow color represents the flow of light.

(a)

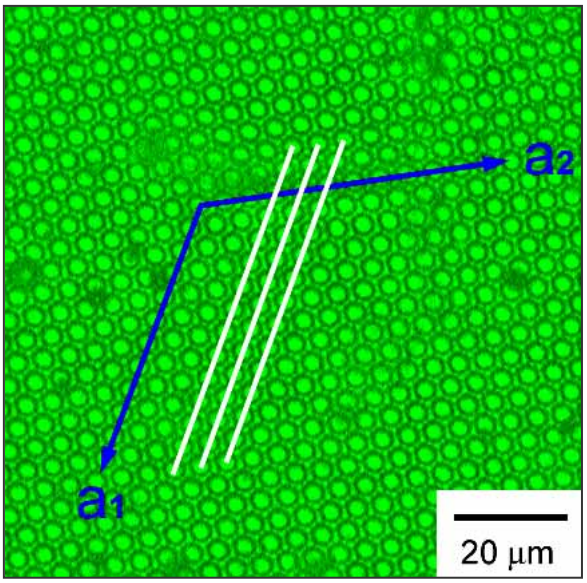

(a′)

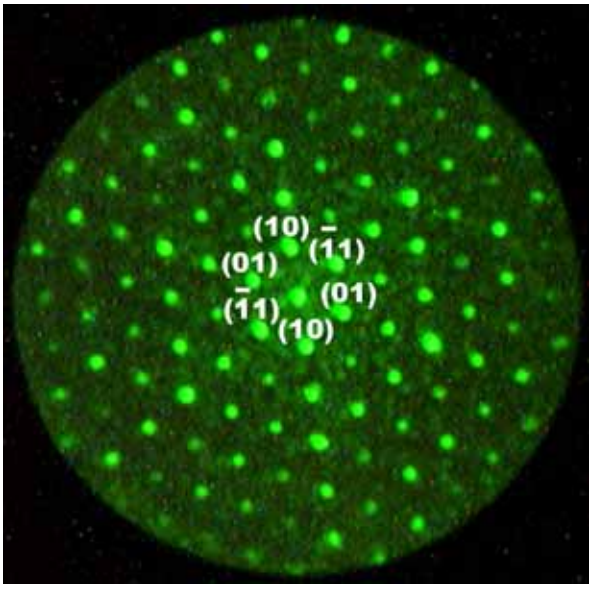

Figure 3.2 (a) Real-space image and (a′) its diffraction pattern of a polystyrene film, cast from a carbon-disulfide solution (~ 1 wt. %). Imaged by an optical microscope (Leica DMRX, 40× dry objective, NA = 0.75) with an interference filter (λ = 532 nm). Miller indices (*hk*) of the first ring of diffraction maxima are shown in (a′) with the unit-vector directions a_1 and a_2 given in (a). The white lines through the centers of the air bubbles parallel are the virtual lattice lines analogous to the lattice planes in a crystal.

Figure 3.2 gives an image of a macroporous film (Figure 3.2a) and its diffraction pattern (Figure 3.2a') by an optical microscope with near monochromatic (λ = 532 nm) illumination. The array of circles in Figure 3.2a is a two-dimensional array of closely-packed spherical pores with top open at the surface of the film. We can see that the macroporous film gives very nice, neat, multiple-spot diffraction pattern with sixfold modulation, which is evident of a high degree of hexagonal order of the air-bubble array.

Average spacing of the bubbles can be calculated from the diffraction pattern based on Eq. (3.1). For a layer of hexagonally packed spheres, d_{hk} is the spacing of a set of parallel lines through the centers of the spheres (white lines drawn in Figure 3.2a), where hk is the two-dimensional Miller index which is usually used in crystallography to specify a set of parallel planes in a crystal [3,4]. The unit cell relationship is given by

$$d_{hk} = \frac{D}{2}\left[\frac{3}{h^2 + hk + k^2}\right]^{\frac{1}{2}}, \tag{3.2}$$

where, D is the center-to-center distance of the spheres [4]. In our experiment, λ is 532 nm and the dispersion medium is air so that $n = n_{\text{air}} = 1$. Thus, by knowing the angle θ, the lattice spacing d_{hk} and the bubble spacing D can be calculated from Eqs. (3.1) and (3.2).

For Gaussian optics (i.e., small angle or paraxial approximation), the relationship of the position of a diffraction point and the sinusoid of the diffraction angle is linear. In a modern optical microscope, a series of lenses are combined to make a complex objective so that the linear approximation can be preserved out to large angles (up to the angular semi-aperture of the objective) [1,2]. In our case,

$$\sin\theta \propto r_{\text{q}}, \tag{3.3}$$

where, r_q is the distance between the zeroth-order diffraction maximum and the mth-order one, which can be directly measured from the diffraction pattern. Combining Eq. (3.1) and Eq. (3.3), we can see that the dimensions of the diffraction lattice are reciprocally related to those of the real lattice (that is why the diffraction space is often called "reciprocal space"). By using a reference with known direct-space spacing (d_{hk} or D), e.g., an optical grating, the diffraction/reciprocal space can be calibrated and the values of d_{hk} and D of other samples can be calculated from their diffraction patterns.

Here, we use the numerical aperture (NA) of the objective to do the calculation. NA is defined as $n\sin\theta_{NA}$, where n is the refractive index of the dispersion medium and θ_{NA} is the angular semi-aperture of the objective, i.e., the maximum angle with respect to the optical axis at which diffracted light can go into the objective [1,2]. Diffraction angle θ_{NA} corresponds to the most outside circle in the diffraction pattern (Figure 3.2a′), thus its sinusoid is proportional to the radius of the NA circle in the diffraction pattern. The values of D calculated from the spot diffraction pattern for a film (Figure 3.2a) are given in Table 3.1. It is evident that the values calculated from the diffraction pattern compare very favorably with those measured from the real-space image.

Table 3.1 Center-to-center distance of air bubbles calculated from diffraction pattern (D_{cal}) according to Eqs. (3.1)–(3.3), comparable with D_{meas} = 4.76 μm measured from the corresponding real-space image (Figure 3.2).

Families of lines	Indices (hk)	Orders (m)	Average d_{cal} (μm)	Average D_{cal} (μm)
{10}	(10), (01), ($\bar{1}$1)	1	4.088	4.720
		2	4.102	4.736
		3	4.122	4.760
		4	4.093	4.727
		5	4.117	4.753
{11}	(11), ($\bar{1}$2), ($\bar{2}$1)	1	2.375	4.750
		2	2.361	4.722
		3	2.371	4.742
{12}	(12), (21), ($\bar{1}$3), ($\bar{3}$1), ($\bar{2}$3), ($\bar{3}$2)	1	1.550	4.735
		2	1.552	4.742
{13}	(13), (31), ($\bar{1}$4), ($\bar{4}$1), ($\bar{3}$4), ($\bar{4}$3)	1	1.140	4.747
{23}	(23), (32), ($\bar{2}$5), ($\bar{5}$2), ($\bar{3}$5), ($\bar{5}$3)	1	0.942	4.743
{14}	(14), (41), ($\bar{1}$5), ($\bar{5}$1), ($\bar{4}$5), ($\bar{5}$4)	1	0.895	4.738
{15}	(15), (51), ($\bar{1}$6), ($\bar{6}$1), ($\bar{5}$6), ($\bar{6}$5)	1	0.740	4.758

3.2 Voronoi Diagram

Voronoi diagram is sometimes called Thiessen or Dirichlet tessellation. In the two-dimensional case, a plane with N separate points is partitioned into N convex polygons (Voronoi polygons) with each polygon containing exactly one point and every point in a given polygon closer to its central point than to any other [5]. The polygons are drawn by joining the bisectors of the lines between the point and its neighbors [6,7], so the number of the nearest neighbors of a point is equal to the number of the sides of its Voronoi polygon. This simple mathematical construct has been extended to three dimensions (Voronoi polyhedrons) and used in many fields such as crystallography and cell biology.

Based on Voronoi diagrams, the sixfold order of our macroporous films can be checked by looking at the coordination number (z) of every air bubble and the fraction (P_z) of every coordination z [5,7]. The coordination number (z) of a bubble is the number of its nearest neighbors, i.e., the number of the sides of its Voronoi polygon. For a perfect hexagonal lattice, all bubbles should have six neighbors and P_6 should equal to one. Further, the degree of order in a system can be described in terms of the entropy of conformation, defined as $S = -\Sigma P_z \ln P_z$ [6,8].

Figures 3.3 and 3.4 are two examples of the Voronoi analysis of our films, where only polygons with non-six sides are drawn (Figure 3.3b and Figure 3.4b). We can see that, in our films, most polygons are six-sided (P_6 is larger than 0.9), only a small amount of polygons with five and seven sides (5-7 pairs) and polygons with other number of sides are almost negligible. Due to the high degree of order, the conformational entropy is

quite small (comparing with the value of 1.71 for a system of random distributed points [8,9]).

(a)

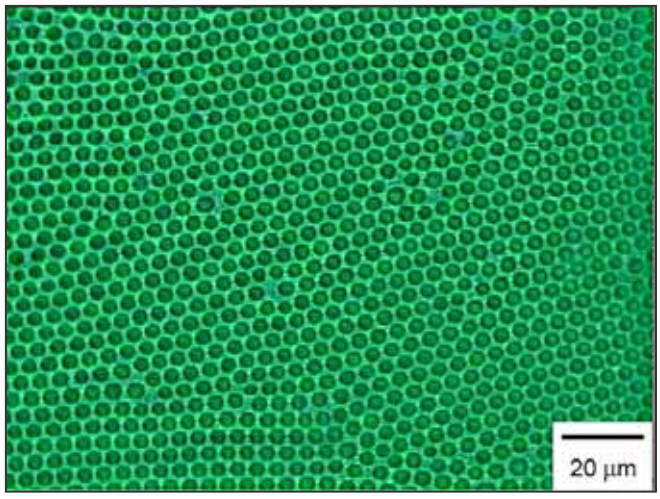

(b)

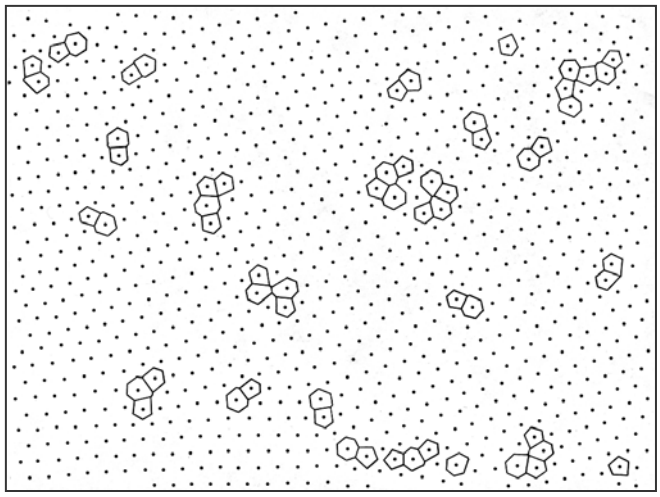

$P_4 = 0.0012$

$P_5 = 0.0392$

$P_6 = 0.9296$

$P_7 = 0.0300$

$S = - \Sigma P_z \ln P_z = 0.3081$

Figure 3.3 (a) Image of a macroporous polystyrene film by an optical microscope (Olympus BX60, 50× 0.75 dry objective) in reflection mode. (b) Voronoi polygon analysis of the image, where the dots correspond to the centers of the air bubbles and polygons with non-six sides are marked. The textbox next to (b) lists the calculated values of the fraction of coordination number (P_z) and the entropy of the system (S).

(a)

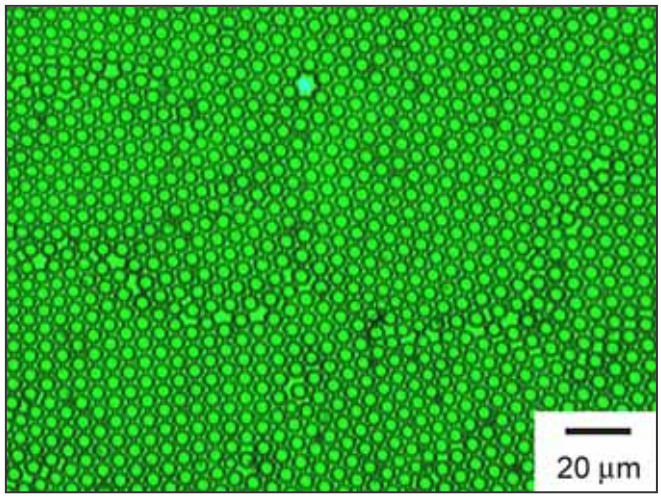

(b)

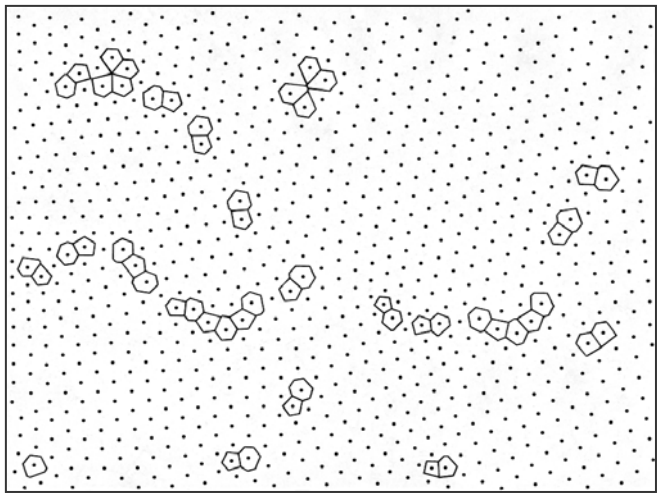

$P_4 = 0.0012$

$P_5 = 0.0322$

$P_6 = 0.9368$

$P_7 = 0.0298$

$S = -\Sigma P_z \ln P_z = 0.2846$

Figure 3.4 Image of a macroporous polystyrene film by an optical microscope (Leica DMRX, 40× 0.75 dry objective) in transmission mode. (b) Voronoi polygon analysis of the image, where the dots correspond to the centers of the air bubbles and polygons with non-six sides are marked. The textbox next to (b) lists the calculated values of the fraction of coordination number (P_z) and the entropy of the system (S).

3.3 Bond-orientational Correlation Function

Another method that one can use to characterize the macroporous films is bond-orientational correlation function, $G_6(r)$, which measures the orientational order of a hexagonal lattice. $G_6(r)$ was first suggested for a two-dimensional melting theory by Nelson et al. [10], and has been used to identify the phase of two-dimensional colloids and plasma crystals.

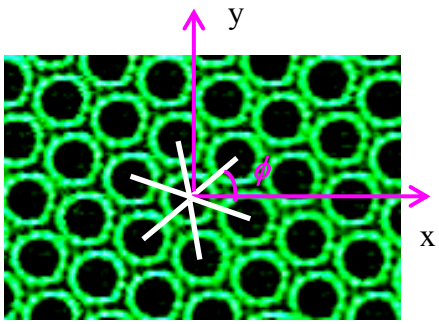

Figure 3.5 The bonds [10] joining a sphere at **r** = (x, y) to its nearest neighbors are shown as white short lines in the image. ϕ is the bond angle with respect to an axis, e.g., x-axis here.

The "bonds" are defined [10] as the imaginary lines joining a sphere at **r** = (x, y) to its nearest neighbors (Figure 3.5). Normalized bond-orientational correlation function is given by [10]

$$G_6(r) \equiv \langle \psi_6^*(\mathbf{r}) \psi_6(\mathbf{0}) \rangle / G_B(r), \tag{3.4}$$

where, $\psi_6(\mathbf{r})$ is the bond-orientational order parameter,

$$\psi_6(\mathbf{r}) \equiv \sum_{\mathbf{r}_{jk}} \delta(\mathbf{r} - \mathbf{r}_{jk}) \exp(6i\phi_{jk}), \tag{3.5}$$

and $G_B(r)$ is the auto-correlation of bond density ρ_B,

$$\rho_B(\mathbf{r}) \equiv \sum_{\mathbf{r}_{jk}} \delta\,(\mathbf{r} - \mathbf{r}_{jk}). \tag{3.6}$$

Here, $\mathbf{r}_{jk}$ are the position vectors of the bond centers and ϕ_{jk} are the bond angle with respect to the x-axis. For a perfect hexagonal crystal, $G_6(r)$ would be fixed at unity for all r. For less ordered solids, $G_6(r)$ decays with increasing r [10]. We use the procedure described by Quinn et al. [11] to do the calculation. First the positions of the air bubble centers are recorded, and then the midpoints $\mathbf{r}_i$ and the angles θ_i (with respect to an arbitrary axis) of the bonds which joint the bubbles to their nearest neighbors are calculated. Next a numerical average of cos $[6(\theta_i - \theta_0)]$ is performed for all bonds i whose midpoints are $r = |\mathbf{r}_i - \mathbf{r}_0|$ away from the midpoint $\mathbf{r}_0$ of the center bond 0, which has a bond angle θ_0. This result is averaged again using each bond as a center bond, yielding $G_6(r)$ [11]. Some results are shown in Figure 3.6, which was calculated using computer software (Matlab 6.1). The programs for this calculation are given in Appendix.

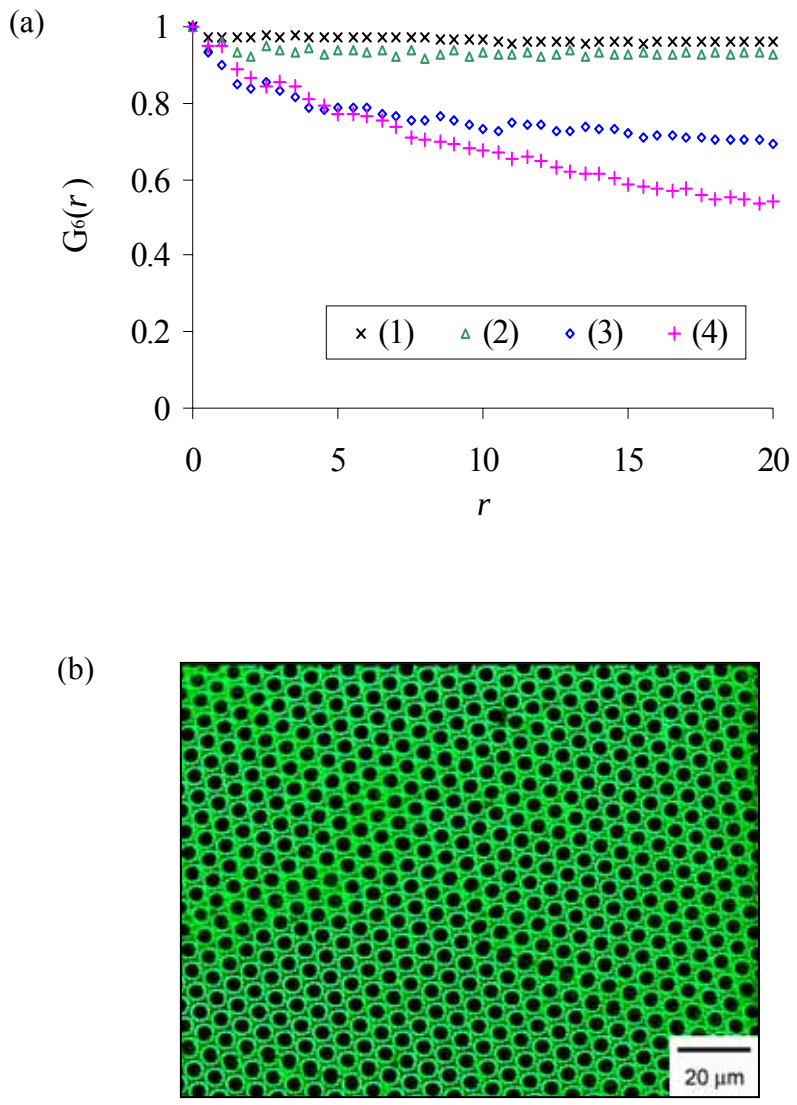

Figure 3.6 (a) Plots of bond-orientational correlation function, $G_6(r)$, in units of average spacing of air bubbles. Curve (1) corresponds to image (b) shown in this figure. Curves (2), (3) and (4) correspond to Figure 3.2a, Figure 3.3a and Figure 3.4a, respectively. (b) Image of a well-ordered macroporous polystyrene film by an optical microscope (Olympus BX60, 50× 0.75 dry objective) in reflection mode.

3.4 Discussion

Comparing the real-space characterization data of sample films whose images are shown in Figure 3.3a and 3.4a, we can see that film in Figure 3.3a has a larger value of $G_6(r)$ (more ordered) but smaller P_6 and larger S (less ordered) than film in Figure 3.4a. This is reasonable because the Voronoi polygon analysis and the orientation correlation function have different emphases. $G_6(r)$ emphasizes on orientational order, and the orientation of bubble array rotates by a large angle across a grain boundary in Figure 3.4a, thus the $G_6(r)$ decays faster with separation distance r; while, for Figure 3.3a, the size of the bubbles is not as uniform as that in Figure 3.4a, some larger or smaller bubbles are trapped locally, leading to more Voronoi polygons with the number of sides different from six. Therefore, the film in Figure 3.3a is more ordered in orientation and less uniform in size comparing with the film in Figure 3.4a.

3.5 Conclusions

In conclusion, we have examined and characterized the 2D hexagonal close-packed arrays of air bubbles in the macroporous films, via Fraunhofer diffraction, Voronoi diagram (coordination and entropy) and orientational correlation function. These characterizations are helpful for further control of the structure formation and quantifying material/device properties as a function of order of the structured films.

References:

[1] S. G. Lipson, H. Lipson, and D. S. Tannhauser, *Optical Physics*, 3rd Ed. (Cambridge University Press, Cambridge, 1995), Ch.7 & Ch.12.

[2] R. S. Longhurst, *Geometrical and Physical Optics*, 2nd Ed. (Longman Group LTD London, 1967), Ch.14.

[3] A. S. Nowick and S. R. Mader, "A hard-sphere model to simulate alloy thin films", *IBM J. Res. Dev.* **Sept.-Nov.**, 358 (1965).

[4] J. W. Goodwin, R. H. Ottewill, and A. Parentich, "Optical examination of structured colloidal dispersions", *J. Phys. Chem.* **84**, 1580 (1980).

[5] See, e.g., A. Okabe, B. Boots, K. Sugihara, and S. N. Chiu, *Spatial Tessellations: Concepts and Applications of Voronoi Diagrams,* 2nd ed. (Wiley, New York, 2000), Ch. 2.

[6] A. Steyer, P. Guenoun, D. Beysens, and C. M. Knobler, "Two-dimensional ordering during droplet growth on a liquid surface", *Phys. Rev. B* **42**, 1086 (1990).

[7] A. Steyer, P. Guenoun, and D. Bensens, "Hexatic and fat-fractal structures for water droplets condensing on oil", *Phys. Rev. E.* **48**, 428 (1993).

[8] D. Weaire and N. Rivier, "Soap, cells and statistics — random patterns in two dimensions", *Contemp. Phys.* **25**, 59 (1984).

[9] A. V. Limaye, R. D. Narhe, A. M. Dhote, and S. B. Ogale, "Evidence for Convective Effects in Breath Figure Formation on Volatile Fluid Surfaces", *Phys. Rev. Lett.* **76**, 3762 (1996).

[10] D. R. Nelson, M. Rubinstein, and F. Spaepen, "Order in two-dimensional binary random arrays", *Philos. Mag. A* **46**, 105 (1982).

[11] R. A. Quinn, C. Cui, J. Goree, and J. B. Pieper, "Structural analysis of a coulomb lattice in a dusty plasma", *Phys. Rev. E* **53**, R2049 (1996).

CHAPTER 4

EVAPORATION OF SOLVENTS

As discussed in Chapters 1&2, the ordered array of air bubbles in the cast polymer films are the imprints of the array of condensed water droplets ─ breath figures (we have also recorded and subsequently analyzed the growth of breath figures on/above evaporating polymer solutions which will be discussed in detail in Chapter 5). In the whole process of the film formation, the evaporation of a volatile solvent plays very important roles [1]. First, it is the evaporation that cools the surface of the solution so that water droplets can nucleate and grow. Secondly, it is the evaporation that makes the transition from liquid polymer solutions to solid polymer films so that the imprints of breath figures are retained. Thirdly, as suggested by Srinivasarao et al. [1], the fast evaporation of a solvent in a polymer solution might result in the levitation of the condensed water droplets above the solution surface. *Whether the water droplets grow and pack above the solution surface or at the solution surface is critical for further understanding the non-coalescence of closely-packed water droplets*. Therefore, to look at the evaporation process of the solvents and polymer solutions, which are used to prepare the macroporous films, under the conditions for the film preparation is essential for a better understanding of the formation of the highly-ordered, macroporous structures.

Thermodynamically, evaporation is the process of atoms or molecules in the liquid state gaining enough energy (to overcome the cohesion energy at the surface) to enter the gaseous state. Therefore, evaporation is always accompanied by a cooling effect [2]. Macroscopically the driving force for evaporation is the difference between the

saturated vapor pressure of the liquid and the partial pressure of the vapor in the surrounding gas (air in most situations). Thus, the evaporation process is very sensitive to external conditions including temperature, partial vapor pressure, airflow velocity (which will bring fresh air to replace the saturated gas medium), and roughness of substrate (which will affect the shape and size of an evaporating surface).

Evaporation of solvents is a quite complicated problem. Multiple processes are involved, such as transfer of heat and mass (through diffusion and convection), in addition to the phase transition from liquid to vapor. Temperature gradients due to evaporation can induce thermal (Rayleigh) instabilities. Meanwhile, the temperature gradients may induce surface/interfacial tension gradients and in turn Marangoni convection in the bulk and instabilities at the liquid-vapor interface [3]. Some studies found that "interfacial turbulence" (chaotically evolved surface instabilities) arose in some conditions which significantly enhanced evaporation [5]. Many attempts have been made, both theoretically and experimentally, to understand and predict the evaporation processes in different situations with the basic theory laid by Maxwell in 1877 [4]. Several simplified models which deal with different limiting cases have been proposed [4,6].

For a liquid mixture composed of both volatile and non-volatile components, the problem can be even more complicated. The non-volatile component can be polymers [7-12] or various kinds of particles [13-22]. For a dilute polymer solution as in our case, the concentration gradients induced by the evaporation of the volatile component can also induce convections and instabilities which may dominate, in some situations, over those due to the thermal gradients [8]. And, when in relatively high concentrations, diffusion of

the volatile component from the viscous bulk to the surface of the liquid can be another limiting factor of the evaporation rate. Further, it has been suggested that a thin layer of polymer ("crust") may accumulate at the liquid-vapor interface [9]. At the same time, strong pinning of the three-phase contact line (i.e., the periphery of the liquid drop where gas, liquid and substrate meet) induced by the deposition of the non-volatile component can induce outward flow which changes the liquid-vapor interface and in turn changes the evaporation process [13-15].

Most of the literature discussed above is focused on the evaporation in a stationary medium, often, air. In our case, during the film formation, moist air is blown across the polymer solution which inputs at least two more factors which can have obvious effects on the evaporation process. One is moving air. Within the laminar-air-flow regime, a thin velocity boundary layer of air forms right above the solution surface, with flow velocity increasing rapidly from zero (relative to the solution surface) at the surface of the solution to that of the unperturbed air flow [4]. At the same time, a diffusion boundary layer and a temperature boundary layer overlap on to it with a similar thickness [4]. The other new factor is condensation of water droplets. The most obvious effect of the condensation of water is the input of heat and mass into the evaporating system which is losing heat and mass due to the evaporation of the solvent. Besides, there should be a new diffusion boundary layer of moisture and the heat and velocity boundary layers should be somewhat disturbed. Also, the condensed water droplets accumulate on the solution surface which might disturb the evaporation of the solvent.

Here, we do not want to go into the detailed process and theory of solvent evaporation, which requires more experiments with better controlled conditions. Rather,

we would like to examine the evaporation processes of the polymer solutions during the formation of macroporous films by simply monitoring the mass over time. For comparison, the same measurements were repeated for pure solvents and for dry airflow. Useful information has been obtained by the simple mass-time measurements.

4.1 Experiments

An analytical balance (METTLER TOLEDO, AT261 DeltaRange) configured for dynamic weighing was used to measure the mass of a layer of polymer solution as a function of time during the formation of a film. Mass data were transmitted to a computer through a data port (RS232) at the back of the balance and collected and processed via software (LabX Balance). Figure 4.1 is a schematic of the experiment setup with moist airflow across the surface of the solutions or the solvents.

The measurements were done by putting a microscope glass slide (cut in half to fit the weighing pan) on the weighing pan of the balance with all of the doors of the balance open and blowing air (from a compressed-air cylinder) through a rectangular glass tube, the same as the glass chamber used in Figure 2.4 without the orifice at the side, across the slide surface. (The balance and the glass tube were placed in a hood with the hood circulation turned off.) Then, with the glass slide on the weighing pan and the airflow across the slide surface, the balance was tared. Several drops (~ 1 to 1.2 ml) of a polymer solution were subsequently loaded onto the slide rapidly by a micropipette and the computer was triggered to collect data. Both moist (humidified by bubbling through distilled water) and dry (directly from the gas cylinder) airflow were used in the experiment.

The measurements were repeated with different airflow rates, which were monitored by a flow meter (see Figure 4.1), with different concentrations of a polystyrene solution (mono-carboxyl terminated, M_w = 50,000) and with different polymers in concentrations which were used to prepare macroporous films.

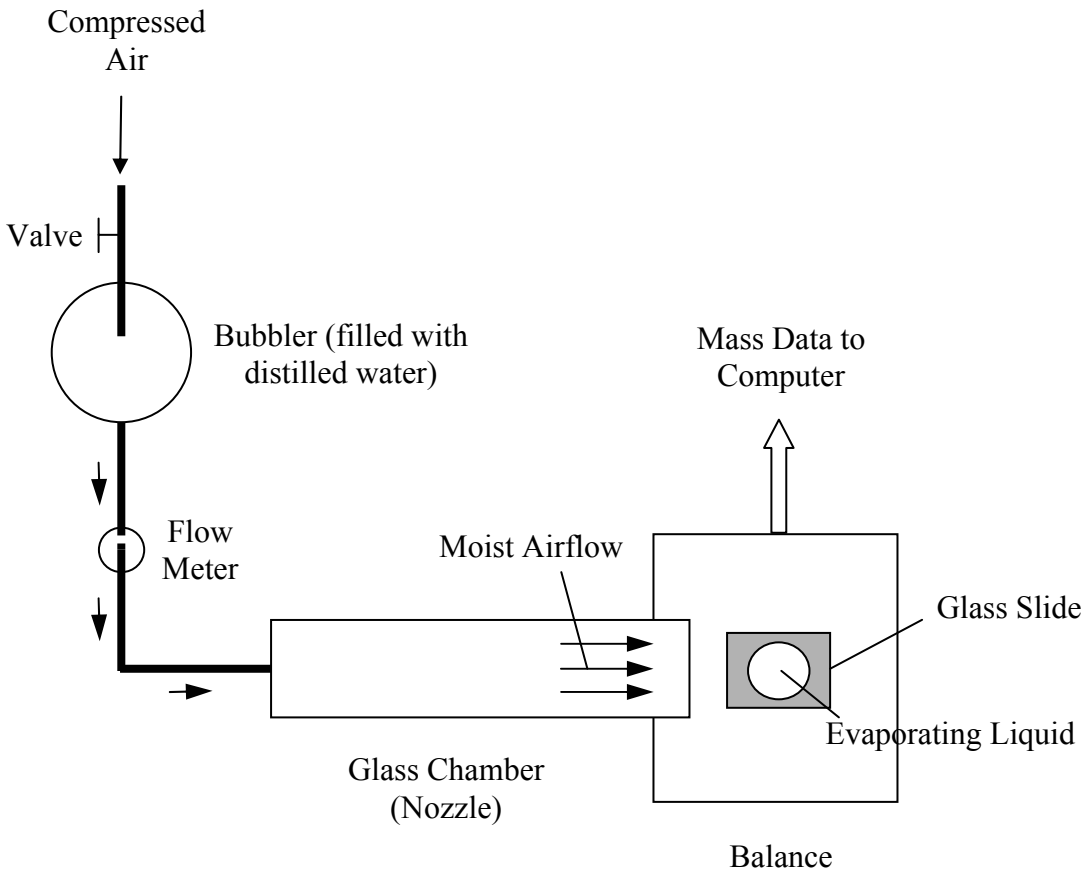

Figure 4.1 Schematic of the experimental setup for measuring the evaporation (mass versus time) of a layer of liquid (a polymer solution or a pure solvent) under moist airflow. Different airflow speeds are applied by adjusting the opening of the valve.

4.2 Results

4.2.1 Carbon Disulfide and Its Polymer Solutions

Mass versus time of pure carbon disulfide and its polymer solutions were measured as described above. For comparison, different airflow rates, dry or moist airflow, different concentrations of polystyrene (mono-carboxyl terminated, M_w = 50,000) and different solutes (i.e., polymers) were used. Representative results are shown in Figure 4.2-4.6. The airflow velocities marked in the figures are estimated values (assuming no leakage anywhere) in the glass chamber, which are calculated by multiplying the readings of the flow meter in the flow path by the cross-section area of the glass chamber (30×10 mm^2).

4.2.2 Benzene and Its Polystyrene Solutions

Similarly, mass versus time of pure benzene and its solution of polystyrene (mono-carboxyl terminated, M_w = 50,000) were measured. Typical results are given Figure 4.7.

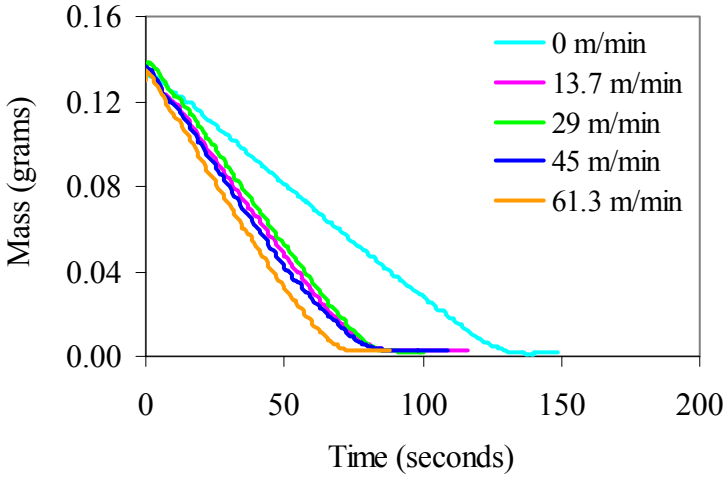

Figure 4.2 Mass versus time of polystyrene (PS1c50, mono-carboxyl terminated, M_w = 50,000) solution with carbon disulfide as a solvent at a concentration of 1 wt. %. The evaporation measurements were made under the conditions described in the experimental section with moist airflow applied. The estimated airflow rates in the glass chamber are listed in the figure.

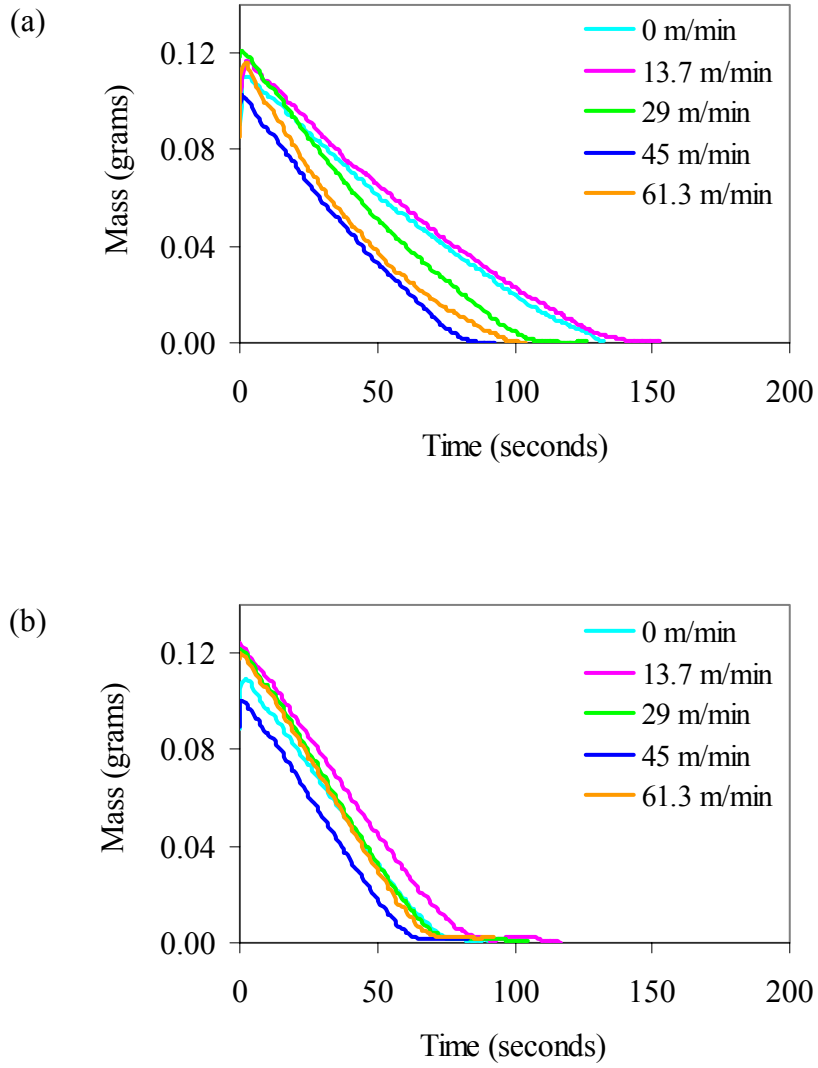

Figure 4.3 Mass versus time of (a) pure carbon disulfide and (b) its solution of polystyrene (mono-carboxyl terminated, M_w = 50,000, 1 wt. %). The evaporation measurements were made under the conditions described in the experimental section with moist airflow applied. The estimated airflow rates in the glass chamber are listed in the figure.

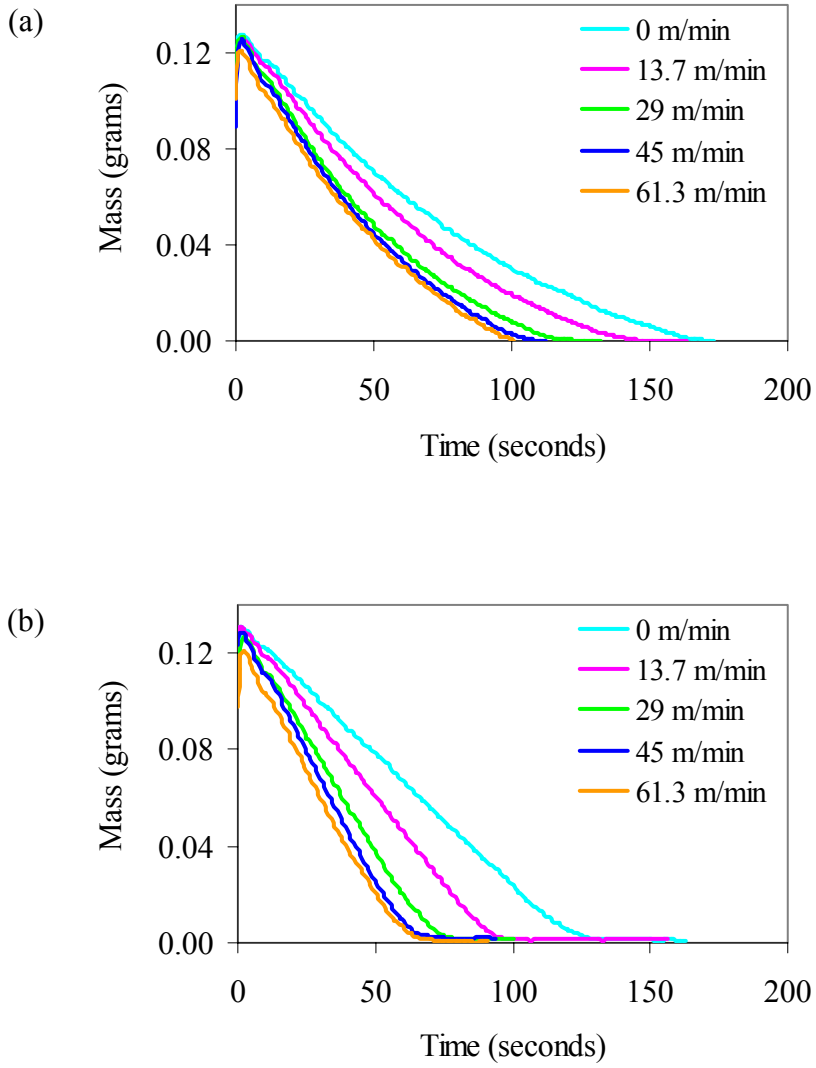

Figure 4.4 Mass versus time of (a) pure carbon disulfide and (b) its solution of polystyrene (mono-carboxyl terminated, M_w = 50,000, 1 wt. %). The evaporation measurements were made under the conditions described in the experimental section with dry airflow applied. The estimated airflow rates in the glass chamber are listed in the figure.

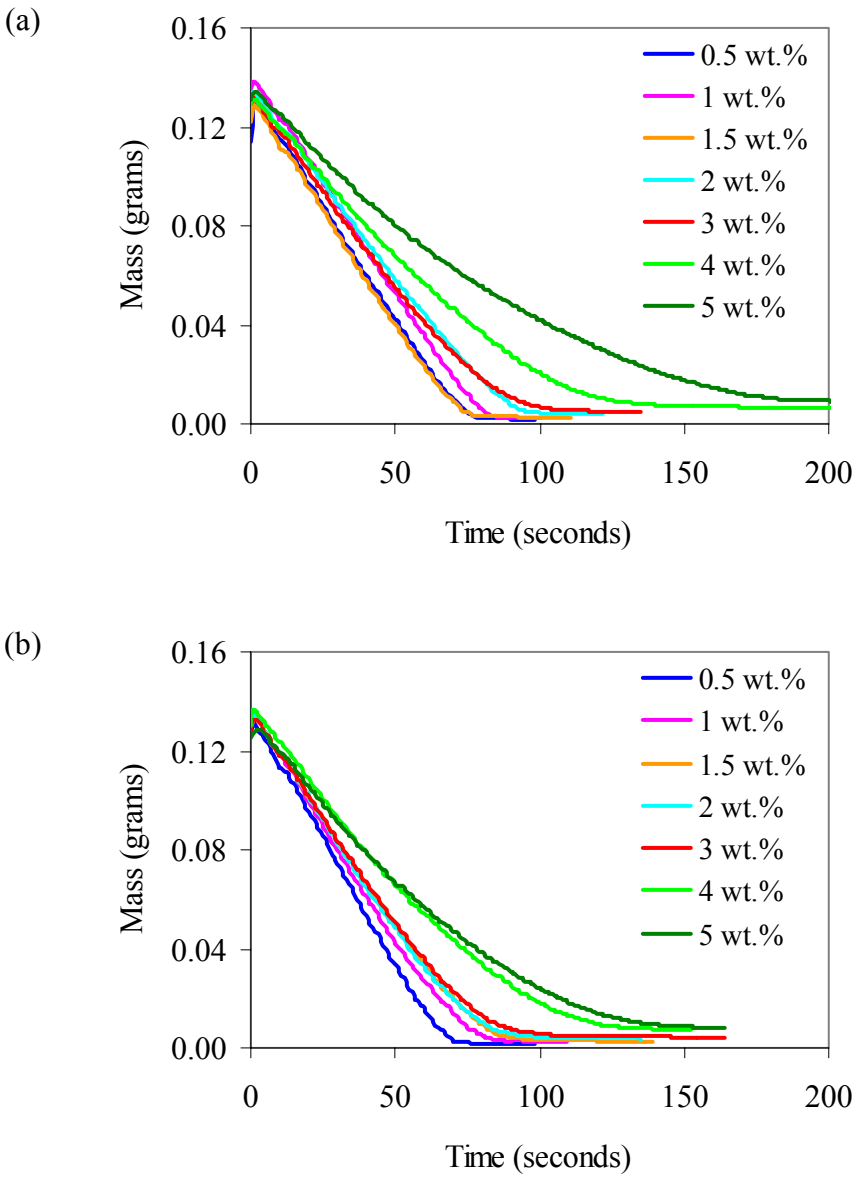

Figure 4.5 Mass versus time of polystyrene (mono-carboxyl terminated, M_w = 50,000) solutions with carbon disulfide as a solvent at different weight concentrations. The measurements were made under the conditions described in the experimental section with moist airflow applied. The estimated airflow rate in the glass chamber was (a) 29 m/min and (b) 45 m/min, respectively.

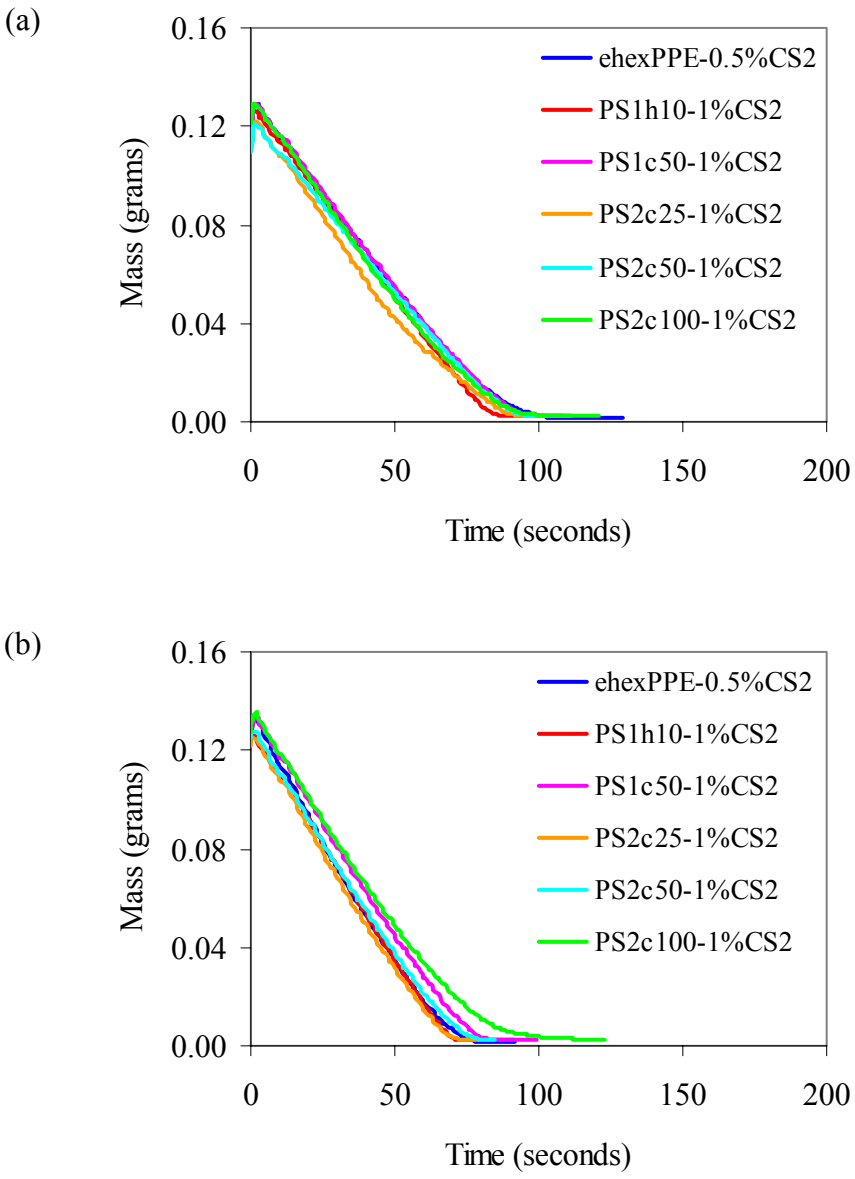

Figure 4.6 Mass versus time of different polymer solutions with carbon disulfide (CS_2) as a solvent at concentrations used to prepare macroporous films. The measurements were made under the conditions described in the experimental section with moist airflow applied. The estimated airflow rate in the glass chamber was (a) 13.7 m/min and (b) 29 m/min, respectively.

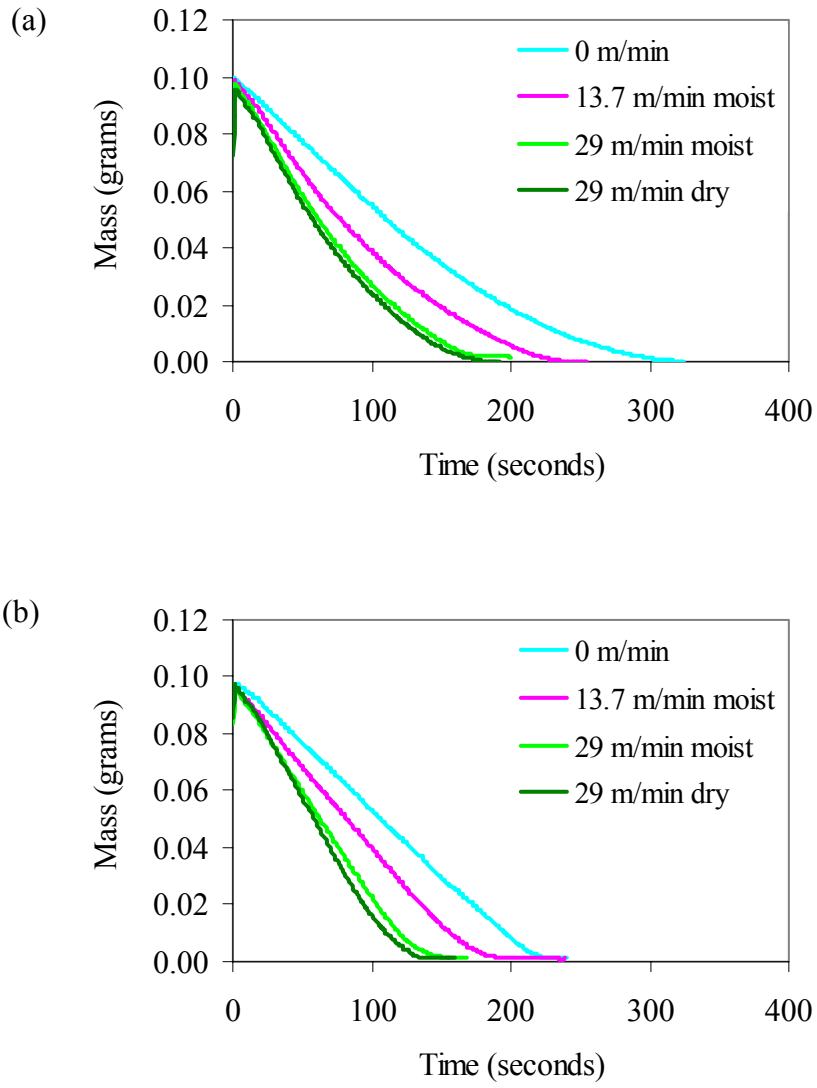

Figure 4.7 Mass versus time of (a) pure benzene and (b) its solution of polystyrene (mono-carboxyl terminated, M_w = 50,000, 1 wt. %). The evaporation measurements were made under the conditions described in the experimental section with different airflow applied. The airflow conditions and the estimated airflow rates in the glass chamber are listed in the figure.

4.3 Discussion

4.3.1 Effect of Airflow Velocity

In the measurements, the general trend was that, with other conditions fixed, higher velocity of airflow led to faster evaporation. This can be seen in Figures 4.2- 4.4 for polymer solutions in carbon disulfide and Figure 4.7 for polymer solutions in benzene. Sometimes, this trend may be obscured by inconsistency of other experimental factors, such as different loading amounts (i.e., initial mass) of sample liquids and pinning or de-pinning of contact lines on the substrates.

Varying the loading amount of the liquid to be tested led to a very different apparent evaporation speed. One example is shown in Figure 4.8, where the only difference among the three evaporation curves is the loading amount of a polystyrene solution. Similar results have been observed by Deegan, et al. [13] and Conway, et al. [16]. This is reasonable since different loading amounts give different liquid-vapor interfaces both in size and in shape and three-phase contact lines with different lengths, which are mainly dictated by the surface and interfacial tensions between the three phases — the substrates, the liquid samples and the surrounding gases. Liquid with a larger loading amount spreads into a liquid film on a glass slide with a larger liquid-vapor interface and a longer contact line, thus it will show a larger mass-loss rate.

Similarly, pinning or de-pinning of the contact lines changes the size and the shape of the liquid-vapor interfaces and the length of the contact lines which in turn affects the rate of mass loss. Weak pinning of the contact line of a sessile drop of pure liquid because of the chemical heterogeneity and/or physical roughness of the substrate at micron-scale, to which the contact angle hysteresis (difference between the advancing

and receding contact angles) is ascribed, has been an active research area in surface science and attracted much interest [23-28]. Recently, it was found that the pinning of the contact line of an evaporating liquid drop could be reinforced by the deposition of suspended particles at the perimeter of the drops which was responsible for the drying patterns such as "coffee ring" [13-15] and a variety of stripe patterns [17,18]. Meanwhile, it has been utilized to self-assemble nano- or micron-sized particles [19-21]. Here, because the heterogeneity (at the microscopic scale) of the glass substrates is not consistent from one to another, and with airflows in different speeds across the surfaces of the glass slides during loading certain amounts of liquid on them (especially, a contact line in the section facing a strong airflow may be de-pinned by the airflow), the pinning and de-pinning of the contact lines were different for different measurements.

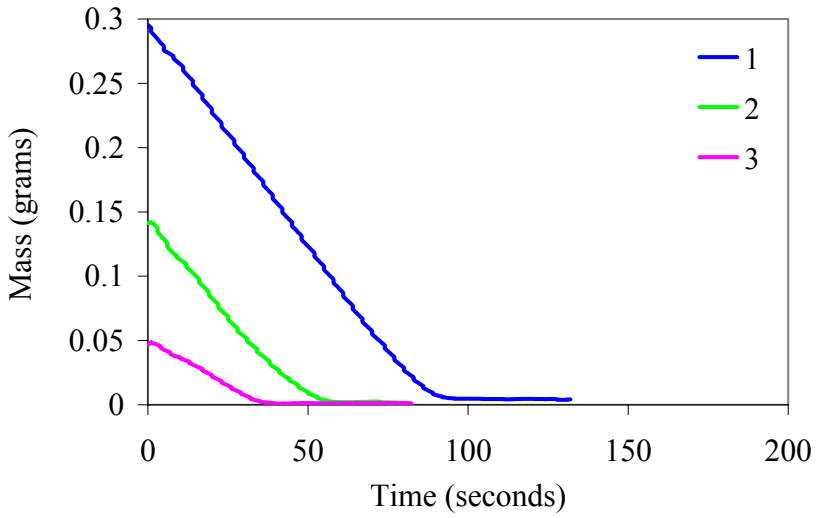

Figure 4.8 Mass versus time of a polystyrene (mono-carboxyl terminated, M_w = 50,000) solution in carbon disulfide at a concentration of 1 wt. % during evaporation. The three evaporation curves (1, 2 and 3) were obtained under the same experimental conditions with different loading amounts (as seen in the figure, it is about 0.3 g for Curve 1, 0.14 g for Curve 2 and 0.05 g for Curve 3). The detailed experimental conditions are described in the experimental section.

4.3.2 Effect of Polymer

4.3.2.1 Pure solvents vs. low-concentration polymer solutions

Comparative experiments on pure carbon disulfide and its low-concentration polymer solution (1 wt. % polystyrene) showed that, although they started from a similar mass-loss (i.e., evaporation) rate, the evaporation rate of pure carbon disulfide decreased gradually over time (Figures 4.3a and 4.4a) while the polystyrene solution evaporated in an almost straight line till a very late stage (Figures 4.3b and 4.4b). This was observed for different airflow speeds and for both moist and dry air. Similar results were observed for benzene and its polystyrene solution as well (Figure 4.7). To compare them more clearly, pairs of pure solvents and polymer solutions at the same experimental conditions (i.e., the content of moisture, the airflow speeds, the loading amounts, etc) are redrawn in Figures 4.9–4.12. Also, linear trendlines are drawn to show the linearity of the evaporation curves of the polymer solutions. The rate of mass loss in the linear part of an evaporation curve, i.e., the slope of the trendline, was obtained from the linearly fitted equation.

The reason for the different evaporation behavior of a pure solvent and its polymer solution was found by observing their evaporation processes. For a pure solvent, the liquid film shrank, i.e., the contact line moved towards the center of the liquid film during evaporation. The size of an evaporating solvent film can change from more than 2 centimeters in diameter at the beginning to only few millimeters at the end. However, almost no shrinking or only slight shrinking was observed for a polymer solution. The contact line was pinned at the original place so that the area of the evaporation surface was almost the same through the whole evaporation process. Therefore, the existence of a small amount of polymer in the solution significantly enhanced the contact-line pinning.

Since larger evaporating area results in larger mass-loss rates, mass-loss rates of pure solvents decreased with time (curved lines) and those of polymer solutions were almost constant with time (straight lines).

Pauchard and Allain [7] observed similar behavior of the contact-area evolution between pure water and its polymer solution during evaporation during the study on the buckling instability induced by polymer solution drying. In their experiments on water suspensions of polystyrene beads, Conway et al. [16], also observed curved evaporation lines of pure water versus more straight ones of polystyrene-bead suspensions in water (Figure 3b in Ref. 16). They attributed this to the rough liquid surfaces due to the suspended polystyrene beads, leading to larger evaporation area. Here, in our case, we obtained similar results both when moist airflow was applied and when dry airflow was applied. When moist airflow was applied, one may argue that the condensed water droplets might suspend on the evaporating solution surface and have the same effect as the polystyrene beads suspend in water as suggested by Conway et al. [16]. However, when dry airflow was applied, there were no condensed water droplets so that the evaporating solution surface was not roughened by any suspensions. Therefore, the explanation by Conway et al. [16] is not applicable to our case.

In addition to the effect of the contact-line pinning, the linearity of the evaporation curves of the polystyrene solution is worth some more discussion. Strictly speaking, the evaporation curves of the polystyrene solution are not exactly linear with time. The evaporation curves can be roughly divided into three regions. At the beginning, with some amount of liquid being suddenly loaded, the balance was reaching the correct reading coupled with fast evaporation (mass loss). The linear part is the second region,

when a steady state was reached. At a later stage (sometimes very late), the evaporation was slowed down gradually until no detectable mass loss. Intuitively, it was thought that the evaporation would slow down gradually with time [1] (contrary to the linear part) for a polymer solution because the concentration of the polymer solution would be increasing with more and more solvent evaporation. Diffusion of the solvent molecules in highly viscous polymer solutions would be slower [29]. Moreover, a layer of polymer aggregate may form at the surface of the solution in a fast evaporating process which can hinder the evaporation [9]. However, this did not seem to be the case for the polystyrene solution (1 wt. %) in the experiments. One possible explanation is that the initial concentration was so low (1 wt. %) that the concentration of polymer at the linear-evaporation range were low enough not to affect the transportation of the solvent molecules to the evaporation surface, i.e., the liquid-vapor interface. Plus, the surface tension of polystyrene is slightly higher than that of the solvents, so that there should be a polymer-depletion layer at the liquid surface [8]. As mentioned above, the evaporation plots of the polymer solution did curve at a very late stage when the concentration was high enough to slow down the evaporation of the solvents. From the mass-time data, simple calculations can be made to estimate the concentrations of the polystyrene solution at which the evaporation started to slow down, that is, at which the evaporation lines started to deviate from the linear trendlines. For example, in Figure 4.9a, the loading mass of the polystyrene solution was about 0.123 g, with a concentration of 1 wt. %, the dissolved polystyrene in the loaded solution was 0.00123 g. From the figure, we can estimate that the mass of the solution at which the evaporation line started to curve was around 0.02 g. So, at that point, the concentration of the polystyrene solution was about 0.00123/0.02 which is equal to 6.15

wt. %. Similarly, the concentrations at other points can be calculated and a plot of the solution concentration over time can be drawn. One example is given in Figure 4.12, which is re-plotted using the data in Figure 4.9a. It can be seen that the concentration of the polymer solution (the red curve) was quite low until the very late stage at which time the concentration rose sharply.

4.3.2.2 Concentration of polymer

As seen in Figure 4.5, when the concentration of polystyrene increased from 0.5 wt. % to 5 wt. %, the evaporation rates of the polystyrene solutions decreased gradually and the linear sections of the evaporation plots were shortened, that is, the evaporation started to slow down at an earlier time. As discussed above, a simple explanation of the shortening of the linear section of an evaporation curve is that the concentration of the evaporating polymer solution reached a critical value at which the diffusion of solvent was slowed down (probably after that point, the evaporation was dominated by the diffusion of solvent molecules in the solution).

4.3.2.3 Nature of polymer

In addition to mono-carboxyl terminated polystyrene, several of the polymers which were used to prepare macroporous films in Chapter 2 were used in the evaporation study. They were dissolved in carbon disulfide in the same concentrations as used in the preparation of the porous films. Generally, ordered macroporous films can be prepared from these polymer solutions except the one of PS1h10 (mono-hydroxyl terminated polystyrene, M_w = 10,000) (see Figure 2.14a). However, as seen in Figure 4.6, the

evaporation curves of the carbon-disulfide solutions of all these polymers almost fell into one line when blown with moist air. This result might suggest that these polymer solutions share the same evaporation mechanism and the evaporation is not the reason for the non-ordered macroporous films from PS1h10.

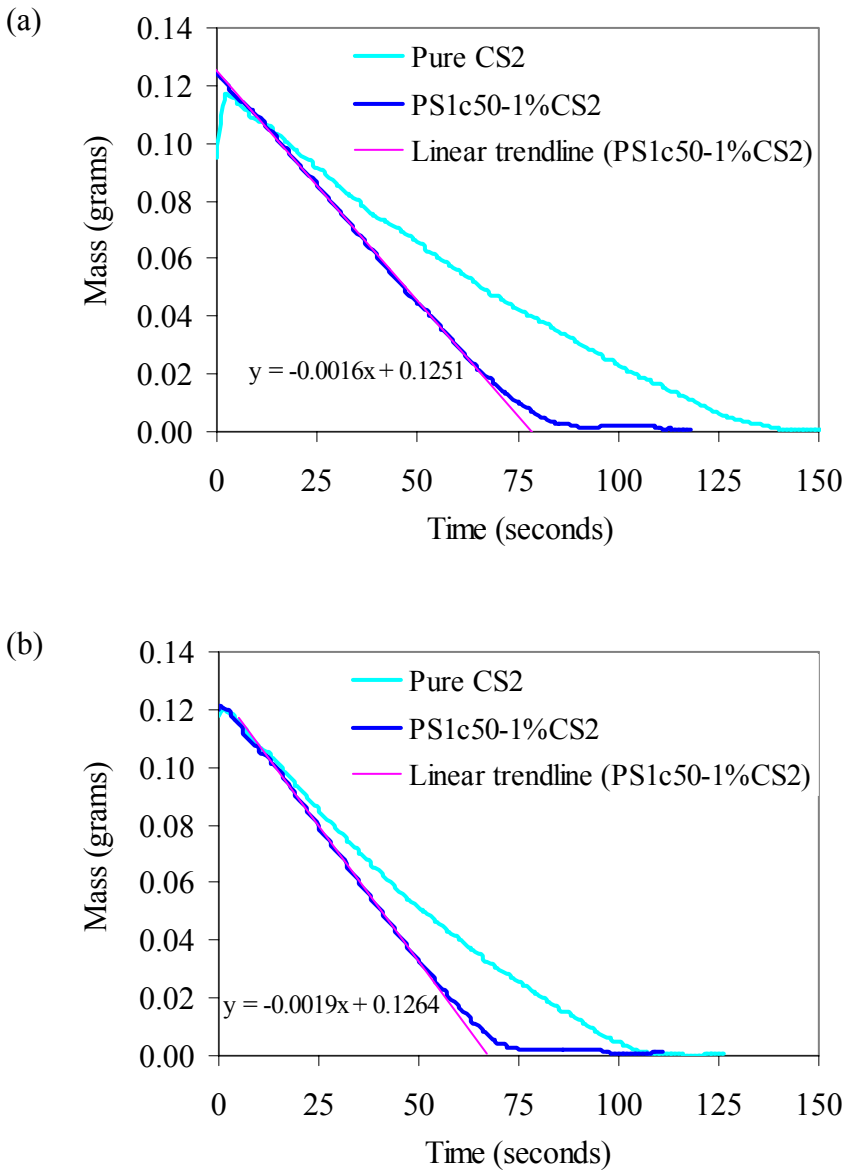

Figure 4.9 Mass versus time of pure carbon disulfide and its solution of polystyrene (mono-carboxyl terminated, M_w = 50,000, 1 wt. %), evaporating in the conditions described in the experimental section. Moisture was added into the airflow by passing it through distilled water. The flow rate in the glass chamber was (a) 13.7 m/min and (b) 29 m/min, respectively. The red lines are the linear trendlines of the evaporation curves of the polystyrene solution and the fitted equations are marked next to it.

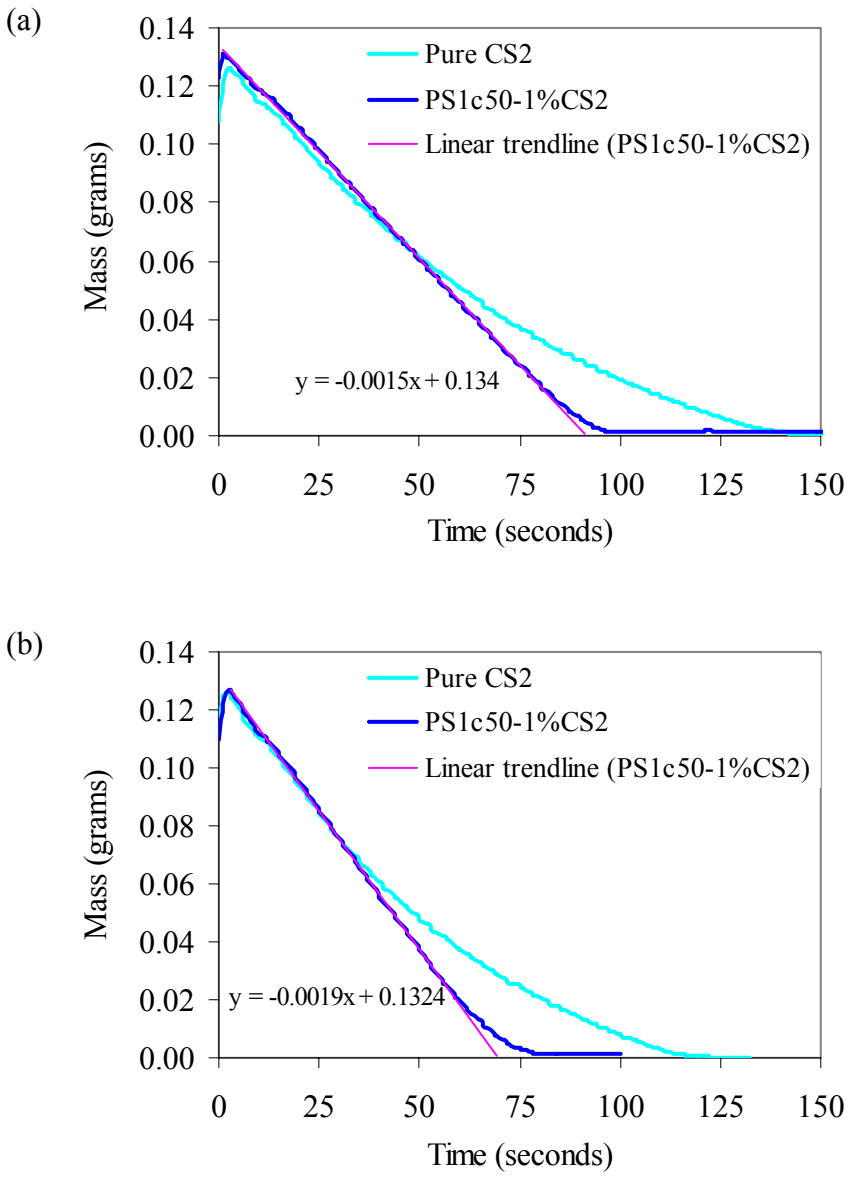

Figure 4.10 Mass data versus time of pure carbon disulfide and its solution of polystyrene (mono-carboxyl terminated, M_w = 50,000, 1 wt. %), evaporating in the conditions described in the experimental section. No moisture was added into the airflow. The flow rate in the glass chamber was (a) 13.7 m/min, (b) 29 m/min. The red lines are the linear trendlines of the evaporation curves of the polystyrene solution and the fitted equations are marked next to it.

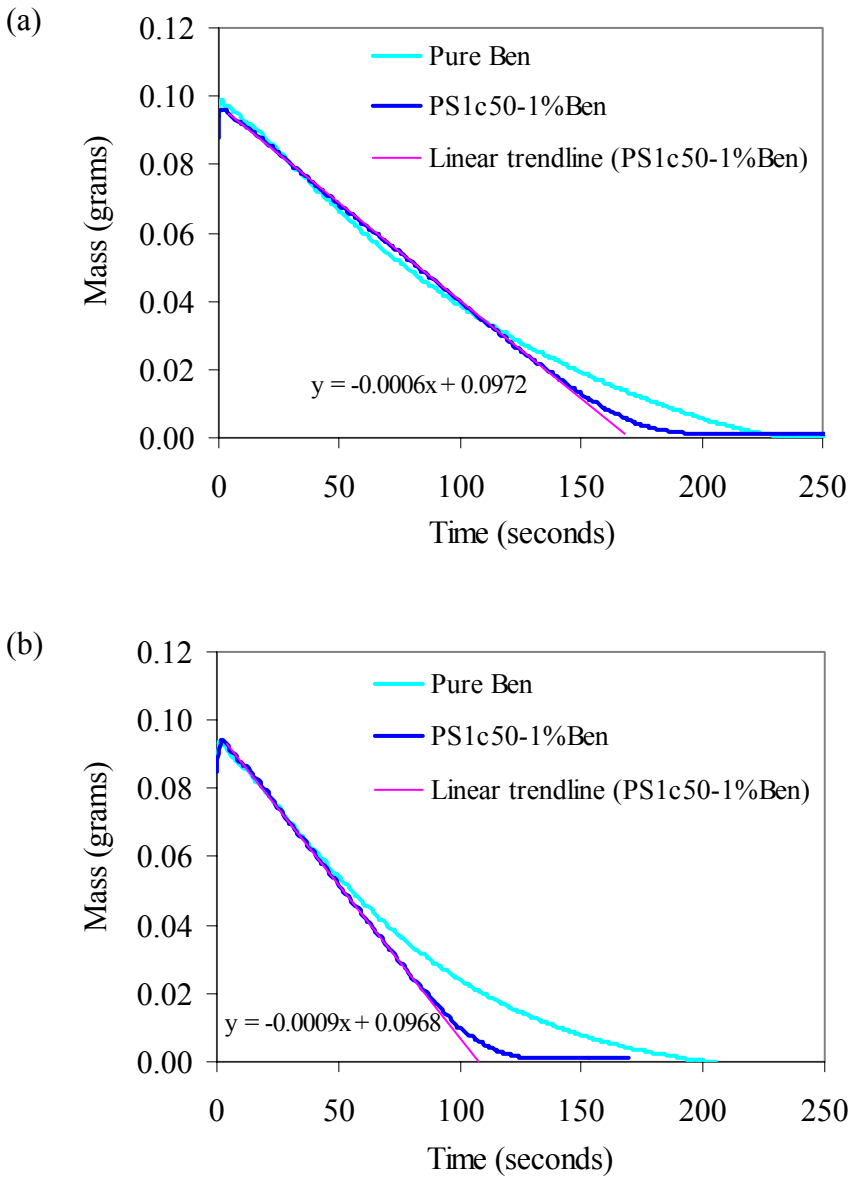

Figure 4.11 Mass data versus time of pure benzene and its solution of polystyrene (mono-carboxyl terminated, M_w = 50,000, 1 wt. %), evaporating in the conditions described in the experimental section. (a) Moist airflow with the flow rate in the glass chamber being 13.7 m/min. (b) Dry airflow with the flow rate in the glass chamber being 29 m/min. The red lines are the linear trendlines of the evaporation curves of the polystyrene solution and the fitted equations are marked next to it.

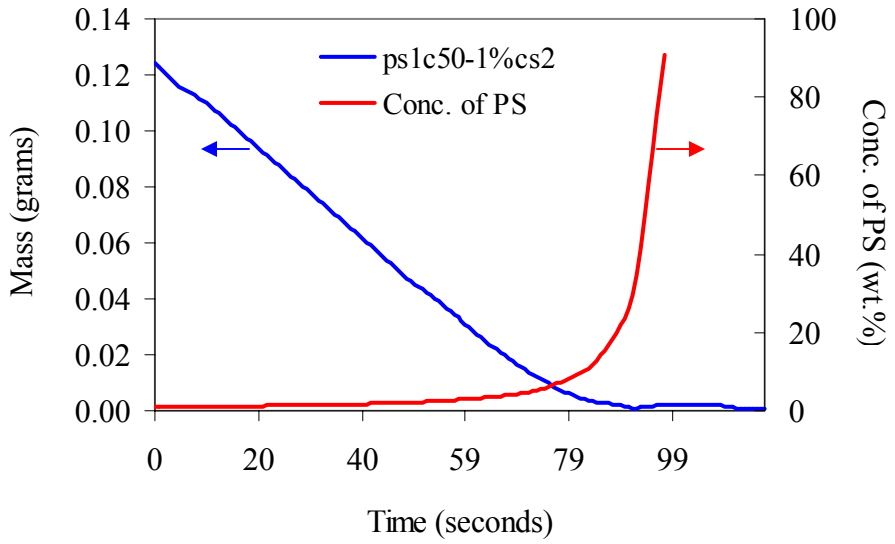

Figure 4.12 Comparison of the mass-time plot of a polystyrene solution (blue curve, the same to that in Fig. 4.9a) with the plot of the concentration of polystyrene in that solution versus time (red curve, calculated from the blue curve). The concentration is seen to be rather low until a very late stage when it rises sharply.

4.3.3 Effect of Moisture

Comparing the evaporation curves of pure solvents and their polymer solutions in moist airflow with those in dry airflow, we did not see very obvious effects of moisture on the evaporation curves, although the evaporation curves under dry airflow seemed to be more vulnerable to experimental errors. Theoretically, when a liquid film evaporates under moist airflow, condensation of water droplets adds both mass and heat to the evaporating system. We can do some simple calculations to estimate the mass of condensed water and subsequently the heat of condensation to see to what degree the condensed water affects the apparent evaporation rates.

On average, a liquid drop with a loading mass of 0.12 g gave a final film with a diameter of 1.8 cm. For simplicity, assume that the film was totally covered with a layer of closely packed water droplets which were uniform in a diameter of 4 μm right before

the film completely dried. Then, the total number of condensed water droplets, N, is given by

$$N = \frac{\text{Area of a polymer film} \times 90.6\,\%}{\text{Projected area of a water droplet}}$$

where 90.6% is the area fraction of circles in the same size which are most closely (i.e., hexagonally) packed in a plane area, i.e., the two-dimensional close-packing limit. With the data above, the calculated value of N is 1.8×10^7. Therefore, the total volume of the condensed water droplets is N times the volume of a single water droplet, which was about 6×10^{-4} cm^3. With density of 1 g/cm^3, the total amount of condensed water during the evaporation of the polymer solution was 0.6 mg. Based on the data in Figure 4.8b, the drying time of the liquid film was around 70 seconds. With an assumption of a constant condensation rate, there was 0.0086 mg water condensing on the evaporating polymer solution surface per second. Comparing with the 1.9-mg-per-second loss of carbon disulfide (data from the equation of the linear trend-line shown in Figure 4.9b), we can see that evaporation dominated the mass change over the condensation of water during the linear section of the evaporation curve. (The counter-effect of the condensation of water on the mass change of a layer of evaporating polymer solution may get more significant at very late stage when the evaporation of solvent was dramatically slowed down.) Furthermore, because the latent heat of condensation of water is 540 cal/g [25], the total heat given out due to the condensation of 0.6-mg water was estimated to be 0.324 cal. And the latent heat of evaporation of carbon disulfide is 85 cal/g [25], so the total heat consumed due to the evaporation of 0.12-g carbon disulfide is 10.2 cal, which is much larger than 0.324 cal. Therefore, the overall heating effect due to the condensation

of water is also negligible, although the local effect of the each water droplet is not known.

According to the literature, the specific heat of carbon disulfide is 18 cal/mol·°C [25], that is, around 0.24 cal/g·°C. For a layer of polystyrene solution in carbon disulfide which evaporates at 1.9 mg/sec (data from Figure 4.9b), the heat loss to the evaporation is 0.16 cal/sec so that the average temperature of the liquid film in a mass of 0.12 g decreases at a rate of 5.6 °C/sec if there is no heat transferred to the surrounding gas and the substrate. Considering the constant mass loss (representing a steady-state process) during the linear section of the evaporation curve and the sensitivity of the evaporation to temperature, there should be a balance between the heat loss due to the evaporation and the heat transported from the air flow and the substrate.

4.4 Conclusions

In conclusion, we have studied the evaporation behavior of pure solvents (carbon disulfide and benzene) and their polymer solutions under the same conditions for preparing ordered macroporous films. For comparison, the experiments were repeated with dry airflow (without bubbling through distilled water). It was found that higher airflow rates and lower polymer concentrations led to faster evaporation. At low polymer concentrations, the mass-time plots were almost straight lines (i.e., constant mass loss) until very late stages when the evaporation slowed down. With the increase of the concentration, the duration of constant mass-loss decreased, that is, the evaporation curves started to curve at earlier stages. However, when the polymer concentration reduced to zero, (i.e., pure solvents), the evaporation rate decreased gradually over time

again. The reason was found to be related to the contact-line-pinning effect due to the existence of small amounts of polymer.

When the mass-time curves of carbon-disulfide solutions of different polymers (including the ones that can form ordered macroporous films and the one that cannot), in the concentrations which were used in the preparation of macroporous films, were plotted in one figure, they were found to almost fall into one line. This might suggest that these solutions of different polymers share the same evaporation mechanism and the evaporation is not responsible for the different degree of order of the obtained porous structures.

No obvious effect of the moist airflow on the evaporation plots of pure solvents and their polymer solutions was seen, comparing with those evaporation processes under dry air flow. Some simple calculations showed that the added mass and heat to a evaporating liquid due to the condensation of water ("breath figures") were relatively small comparing with the mass and heat loss due to the evaporation of carbon disulfide.

4.5 Recommendations

Although much information on the evaporation process of polymer solution during film formation process was obtained from this experiment, there are still many details unclear. For example, what is the limiting factor for the evaporation of polymer solutions, and are they the same for the whole evaporation period and different conditions? Are there any convections and instabilities developed during the fast evaporation and how they affect the evaporation? Is there any polymer "crust" forming on the surface of the evaporating liquid? How do the condensed water droplets locally affect the

evaporation? To answer these questions, much more work, both experimentally and theoretically (by simulations), is to be done.

References:

[1] M. Srinivasarao, D. Collings, A. Philips and S. Patel, "Three-dimensionally ordered array of air bubbles in a polymer film", *Science* **292**, 79 (2001).

[2] V. P. Carey, *Liquid-vapor phase-change phenomena* (Hemisphere, Washington, DC, 1992), p19.

[3] M. F. Schatz and G. P. Neitzel, "Experiments on thermocapillary instabilities", *Annu. Rev. Fluid Mech.* **33**, 93 (2001).

[4] N. A. Fuchs, *Evaporation and droplet growth in gaseous media* (Pergamon, London, 1959), Ch.I and Ch.II.

[5] P. Colinet, J.C. Legros and M.G. Velarde, *Nonlinear Dynamics of Surface-Tension-Driven Instabilities* (Wiley, Berlin, 2001), p96.

[6] Y. S. Lou, "On nonlinear droplet condensation and evaporation problem", *J. Appl. Phys.* **49**, 2350 (1978).

[7] L. Pauchard and C. Allarn, "Buckling instability induced by polymer solution drying", *Europhys. Lett.* **62**, 897 (2003).

[8] P. G. de Gennes, "Instabilities during the evaporation of a film: Non-glassy polymer + volatile solvent", *Eur. Phys. J. E* **6**, 421 (2001).

[9] P. G. de Gennes, "Solvent evaporation of spin cast films: 'crust' effects", *Eur. Phys. J. E* **7**, 31 (2002).

[10] M. Tsige and G. S. Grest, "Molecular dynamics study of the evaporation process in polymer films", *Macromolecules* **37**, 4333 (2004).

[11] Th. Klupsch, P. Mühlig and R. Hilgenfeld, "The distribution of a macromolecular solute within an evaporating drop: an exact analytical solution", *Colloids and Surfaces A: Physicochem. Eng. Aspects* **231**, 85 (2003).

[12] C. C. Annarelli, J. Fornazero, J. Bert and J. Colombani, "Crack patterns in drying protein solution drops", *Eur. Phys. J. E* **5**, 599 (2001).

[13] R. D. Deegan, O. Bakajin, T. F. Dupont, G. Huber, S. R. Nagel and T. A. Witten, "Contact line deposits in an evaporating drop", *Phys. Rev. E* **62**, 756 (2000).

[14] R. D. Deegan, O. Bakajin, T. F. Dupont, G. Huber, S. R. Nagel and T. A. Witten, "Capillary flow as the cause of ring stains from dried liquid drops", *Nature* **62**, 756 (2000).

[15] R. D. Deegan, "Pattern formation in drying drops", *Phys. Rev. E* **61**, 475 (2000).

[16] J. Conway, H. Korns and M. R. Fisch, "Evaporation kinematics of polystyrene bead suspensions", *Langmuir* **13**, 426 (1997).

[17] E. Adachi, A. S. Dimitrov and K. Nagayama, "Stripe patterns formed on a glass surface during droplet evaporation", *Langmuir* **11**, 1057 (1995).

[18] L. Shmuylovich, A. Q. Shen and H. A. Stone, "Surface morphology of drying latex films: multiple ring formation", *Langmuir* **18**, 3441 (2002).

[19] N. D. Denlov, O. D. Velev, P. A. Kralchevsky, I. B. Ivanov, H. Yoshimura and K. Nagayama, "Observations of latex particle two-dimensional-crystal nucleation in wetting films on mercury, glass and mica", *Langmuir* **8**, 3183 (1992).

[20] E. R. Dufresne, E. I. Corwin, N. A. Greenblatt, J. Ashmore, D. Y. Wang, A. D. Dinsmore, J. X. Cheng, X. S. Xie, J.W. Hutchinson and D. A.Weitz, "Flow and fracture in drying nanoparticle suspensions", *Phys. Rev. Lett.* **91**, 224501 (2003).

[21] P. C. Ohara and W. M. Gelbart, "Interplay between hole instability and nanoparticle array formation in ultrathin liquid films", *Langmuir* **14**, 3418 (1998).

[22] V. X. Nguyen and K. J. Stebe, "Patterning of small particles by a surfactant enhanced Marangoni-Bénard instability", *Phys. Rev. Lett.* **88**, 164501 (2002).

[23] J. F. Joanny and P. G. de Gennes, "A model for contact angle hysteresis", *J. Phys. Chem.* **81**, 552 (1984).

[24] P. G. de Gennes, "Wetting: statics and dynamics", Rev. Mod. Phys. **57**, 827 (1985).

[25] J. F. Oliver, C. Huh and S. G. Mason, "Resistance to spreading of liquids by sharp edges", *J. Colloid Interface Sci.* **59**, 568 (1977).

[26] Y. H. Mori, T. G. M. van de Ven and S. G. Mason, "Resistance to spreading of liquids by sharp edged microsteps", *Colloid Surf.* **4**, 1 (1982).

[27] A. Tanguy and T. Vettorel, "From weak to strong pinning I: a finite size study", *Eur. Phys. J. B* **38**, 71 (2004).

[28] X. Noblin, A. Buguin and F. Brochard-wyart, “Vibrated sessile drops: transition between pinned and mobile contact line oscillations”, *Eur. Phys. J. E* **14**, 395 (2004).

[29] H. Richardson, M. Sferrazza and J. L. Keddie, “Influence of the glass transition on solvent loss from spin-cast glassy polymer thin films”, *Eur. Phys. J. E* **12**, s87 (2003).

[30] I. M. Smallwood, *Handbook of organic solvent properties* (Arnold, London, 1996).

CHAPTER 5

BREATH FIGURES ON EVAPORATING POLYMER SOLUTIONS

Breath figures (that is, patterns of condensed water droplets forming on partially wetted surfaces) have been studied by a number of researchers from Lord Rayleigh [1,2], Aitken [3] and Baker [4] in the early 1900's, to more recently by Beysens, Knobler and their coworkers [5-12], and Briscoe and Galvin [13,14]. Most of the experiments focused on water droplet patterns formed on a cold solid surface, while a liquid substrate (paraffin oil) has also been studied by Beysens and Knobler [5,8,12].

In their experiments, both on a solid surface and on a liquid one, Beysens and Knobler [5,6,9] found that the average droplet size (the droplet radius, R) over time, t, followed two power laws, one at early time with an exponent of around 1/3 ($R \sim t^{1/3}$) and another one at late time with an exponent close to unity ($R \sim t$). The increase of the power-law exponent from 1/3 to 1 was due to coalescence. At early time, droplets were separate and grew as isolated particles; while, at later times, the growth was dominated by coalescence so that water droplets can speed up their growth by coalescence. An expression has been deduced for the growth of a single drop of radius R, or a pattern of drops without interactions [11],

$$R \sim (\sqrt{U^*}\Delta T_s^{0.8} D_{12} t)^{1/3} \tag{5.1}$$

where, $U^* = U(\nu D_{12}^2)^{-1/3}$ is a reduced flow velocity with U being the average velocity of the gas (airflow), ν is the kinematic viscosity of the gas, D_{12} is the mutual diffusion coefficient of water in the carrier gas, and ΔT_s is the temperature difference between the gas mixture (moist air) and the surface where the breath figure forms. When U^*, ΔT_s and

D_{12} are independent of time, the radius of a single drop is proportional to the time, t, to the power of 1/3.

However, breath figures formed on a liquid substrate did show some unusual features compared with those on a solid surface. Beysens and Knobler [5,11] found that the first stage of growth was much longer on the liquid surface which they ascribed to the smoother liquid surface so that fewer nuclei formed. More importantly, a much more ordered structure, termed as the "hexatic phase", was observed on paraffin oil surface at the first stage of the breath-figure formation process [8,12], while only a local liquid-like order was seen on the solid substrate [11].

Here, we want to study the breath figures formed on our volatile polymer solutions since it is these breath figures that serve as templates for the formation of the macroporous films. Compared with the liquid substrate used by Beysens and Knobler [5,8], i.e., paraffin oil (non-volatile and highly viscous), the fast evaporation of solvent and the existence of polymer render many factors to change dynamically with time such as temperature and polymer concentration, and can introduce many new processes such as convection and diffusion of solvent/polymer within the liquid.

Experiments on breath figures formed on evaporating polymer solutions have been carried out by Limaye et al. [15] where a small amount of polystyrene was dissolved in benzene and chloroform (~ 5 wt. %). Their study was inspired by Beysens and Knobler's work, and focused on the evolution of breath figures on a volatile liquid (e.g., the crossover of single-droplet growth and coalescence-dominated growth). They did not try to prepare ordered macroporous films and did not obtain well-ordered breath figures for their experimental conditions. Pitois and François [16] studied the growth of breath

figures on a solution of PS-PPP and CS_2, under conditions that lead to a well-ordered macroporous film, by light scattering (they were not able to obtain high-quality recordings of these breath figures in the direct space). Karthaus et al. [17] did record some ordered breath figures formed on pure chloroform and its solution of an amphiphilic polyion complex. However, the recorded images are blurry and they also used the light-scattering method to measure the growth law. All of these studies found that the single-droplet growth followed a 1/3 power law.

Although the light-scattering experiment can provide average information of the size and packing of the breath figures, many details are missed. Therefore, in our experiments, we study the breath figures during the formation of ordered macroporous films in the real space, i.e., directly record the formation of well-ordered breath figures via a high-speed camera coupled with an optical microscope in high quality. Due to the limitation of the optical microscope resolution and the difficulty to focus on the breath figures at the initial stage, in this study, we will concentrate on the later stage when the condensed water droplets can be clearly differentiated. Many interesting features of the breath figures were revealed and their growth over time was measured from selected frames.

5.1 Experiments

A high-speed digital camera (Photron FASTCAM-DVR) was connected to an optical microscope (Leica DMLSP) with a long-work-distance objective (50× 0.5 L) to record the film forming process in transmission mode. Polystyrene (mono-carboxyl terminated, Mw = 50,000) and hexoxyl PPE solutions with carbon disulfide as a solvent

were used in the study. In the experiment, a microscope glass slide (purchased from Fisher Scientific, precleaned) was placed on the stage of the microscope and the microscope is focused on the top surface of the glass slide. Air from a compressed-air cylinder was first bubbled through distilled water and then blown through a rectangular glass tube across the slide surface (see Figure 4.1). With the position of the stage and airflow fixed, the slide was moved out of the optical path (vertical) and the airflow path (horizontal) and the camera was triggered to record. After an amount of polymer solution (~ 1.2 ml) was loaded on it, the slide was moved back and the stage of the microscope is lowered first to get into focus on the breath figures and then the stage is raised gradually to keep the condensed water droplets layer in focus since the solution surface lowered continuously during the evaporation of the solvents. All of the observations were made at the center regions of the liquid films. A recording speed of 125 frames per second was used in the experiments. Image analysis was then carried out by computer software (Image-Pro Plus) on selected recordings.

5.2 Results

Representative movies on film formation processes are given in Movies 5-1 to 5-3 (played at a speed of 30 frames per second, four times slower than the recording speed), where Movies 5-1 and 5-3 are two recordings of the evolution of breath figures on evaporating PS-CS_2 solutions with different airflow speed, and Movie 5-2 is on a hexoPPE-CS_2 solution. The velocity of moist airflow was estimated (volume flow rate read from the airflow meter multiplied by cross-sectional area of the glass chamber) to be 13.7 m/min in the glass chamber for Movie 5-1 and 29 m/min for Movies 5-2 and 5-3.

Figures 5.1 and 5.2 are image frames selected from Movie 5-1 and 5-2, respectively, and arranged according to time. The time corresponding to each frame is true relative to each other, not absolutely, because the start time when water nucleated is hard to tell.

Growth of the breath figures (average diameter of water droplets over time) in Movies 5-1 and 5-2 are plotted in Figure 5.3. Linear trendlines and fitted equations are given. The average diameter at a given time is an average of all of the water droplets in one recorded frame except for the extremely larger or smaller ones.

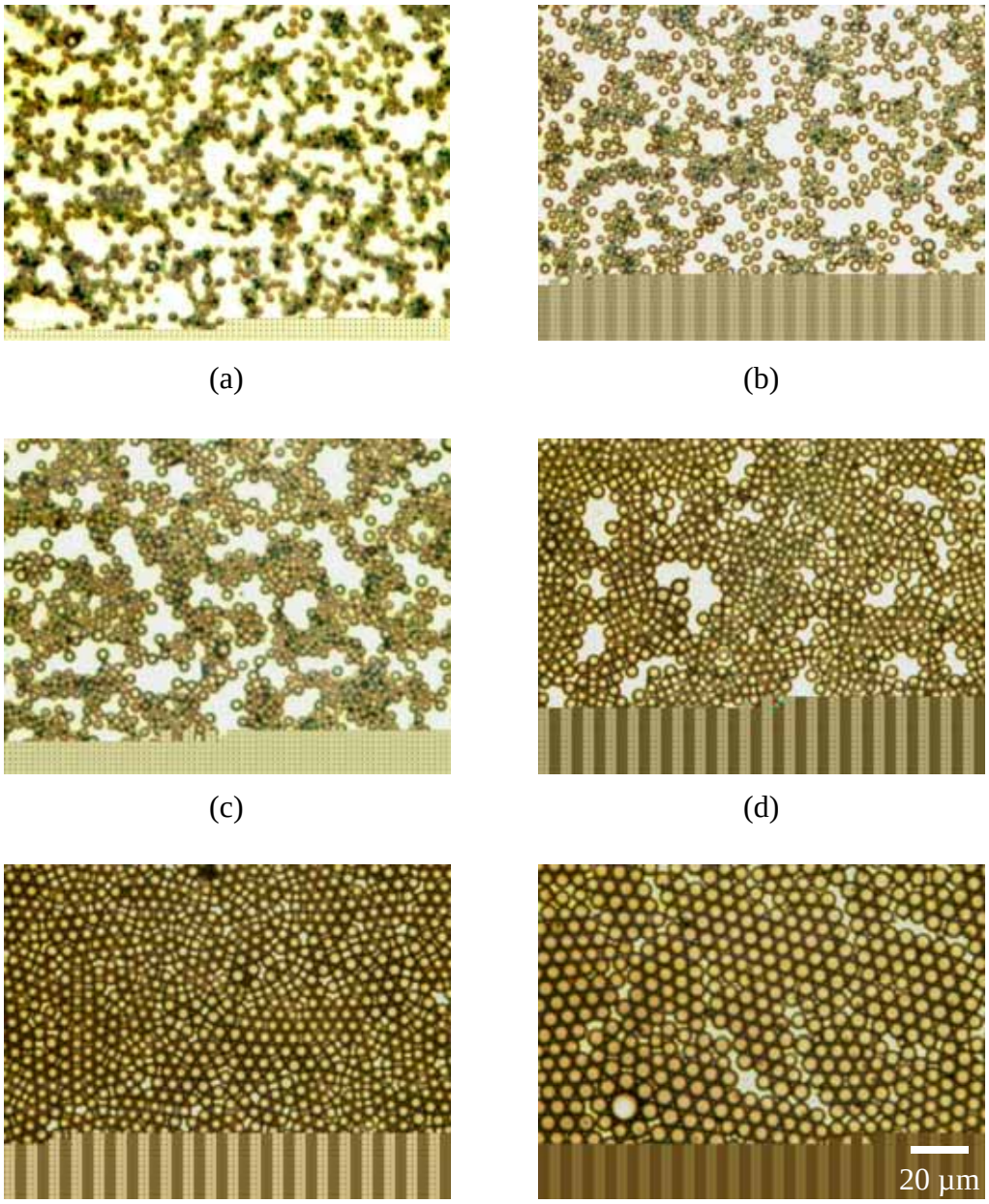

Figure 5.1 Evolution of breath figure formed on a layer of PS-CS_2 solution (~ 1 wt. %) under moist airflow (at a speed of about 13.7 m/min in the glass chamber), where (a) – (f) are in a time scale of 8.6 s, 11.0 s, 17.6 s, 29.3 s, 36.1 s and 59.8 s, respectively. Selected frames of Movie 5-1. Imaged by an optical microscope (Leica DMLSP, 50× 0.5 L) coupled with a high-speed digital camera (Photron FASTCAM-DVR).

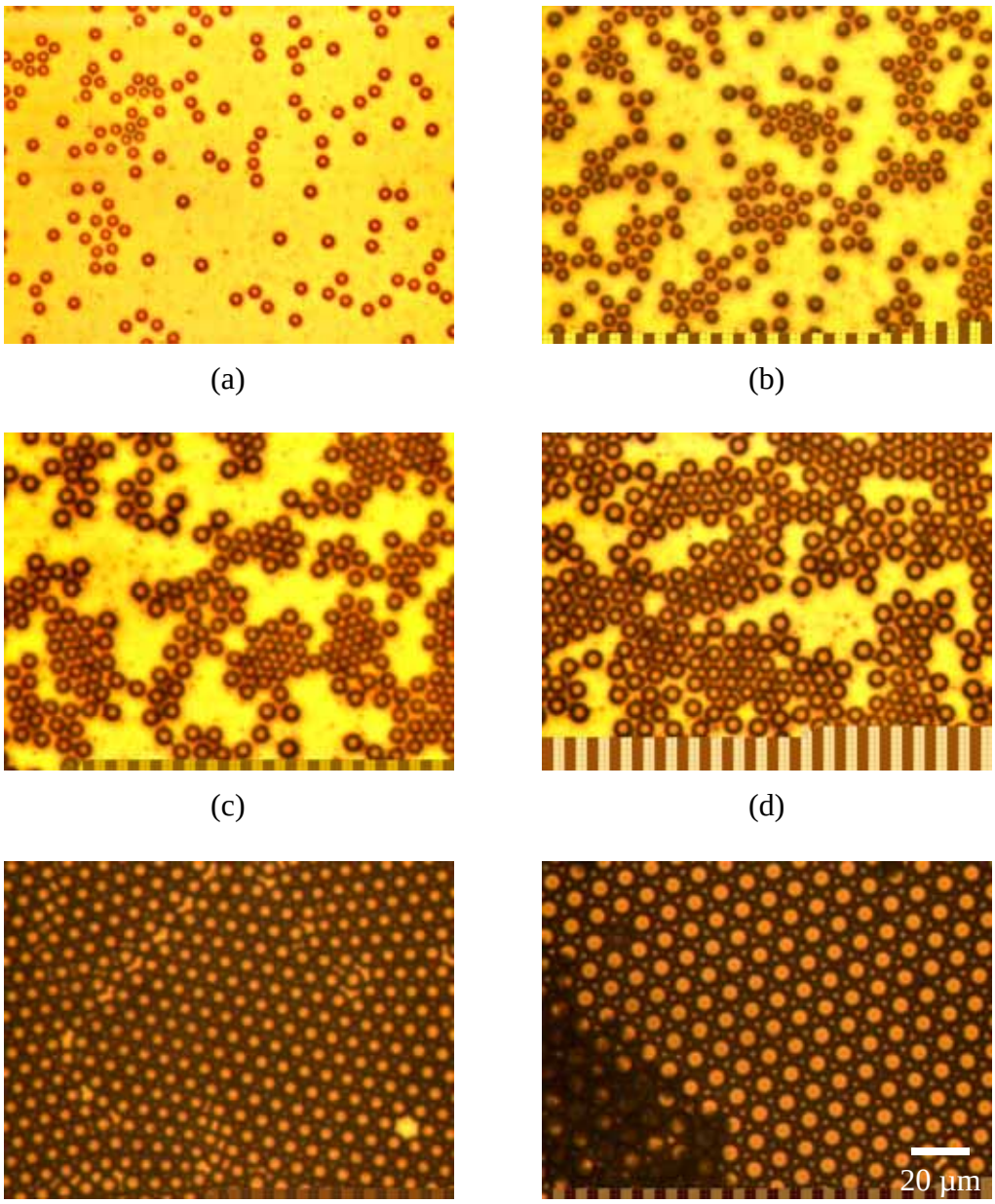

Figure 5.2 Evolution of breath figures formed on a layer of hexoPPE-CS_2 solution (~ 0.2 wt. %) under moist airflow (at a speed of about 13.7 m/min in the glass chamber), where (a) – (f) are in a time scale of 9.4 s, 15.3 s, 21.3 s, 25.8 s, 43.2 s and 74.9 s, respectively. Selected frames of Movie 5-2. Imaged by an optical microscope (Leica DMLSP, 50× 0.5 L) coupled with a high-speed digital camera (Photron FASTCAM-DVR).

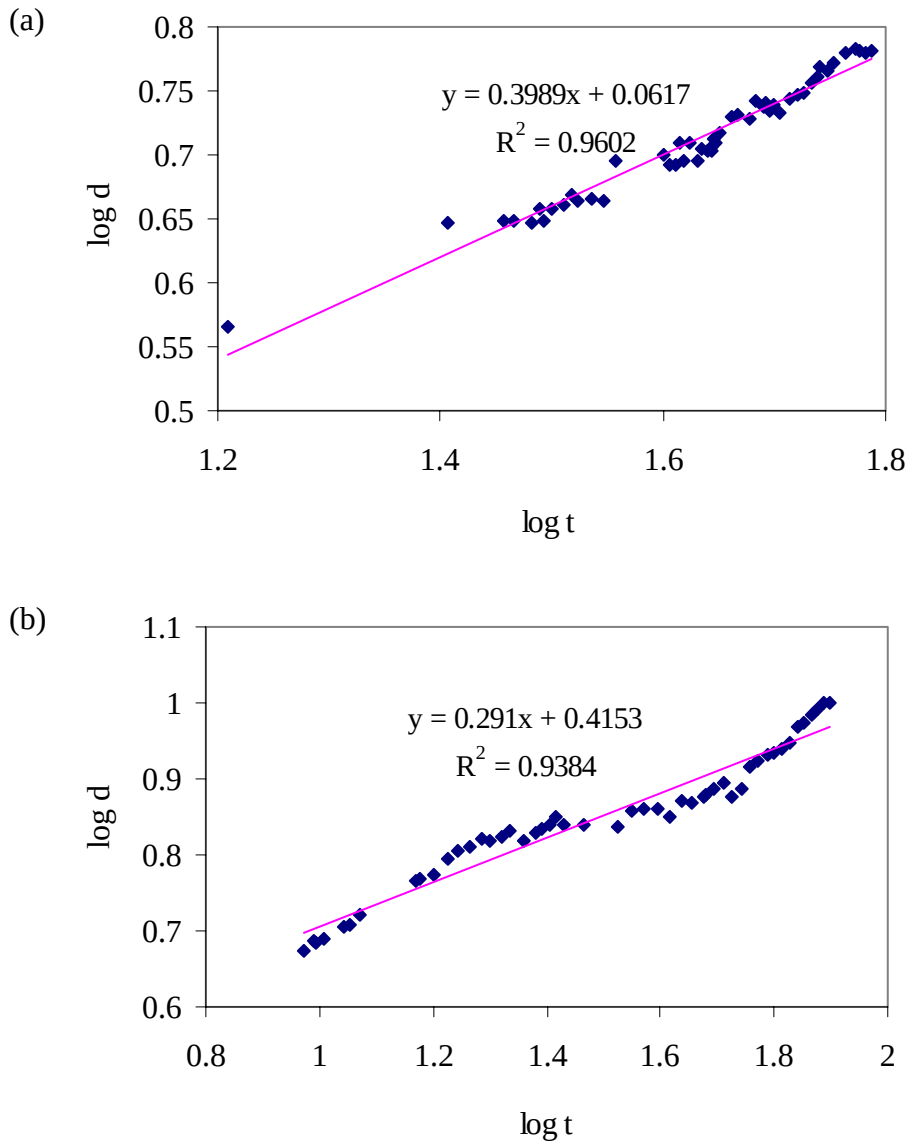

Figure 5.3 Log-Log plots of average diameter of water droplets, *d*, as a function of time, *t*. Linear trendlines (red lines) are drawn with the fitted equations. Breath figures were formed on a layer of (a) PS-CS_2 solution (Movie 5-1) and (b) hexoPPE-CS_2 solution (Movie 5-2). Here, the values of time are relative because it was hard to tell the exact time when water droplets nucleated.

5.3 Discussion

5.3.1 Packing of Water Droplets

As seen in the movies (or Figures 5.1 and 5.2), these breath figures share many similarities. At the beginning, tiny water droplets formed across the solution surface in a time, separate and very mobile. They grew as a function of time, almost to the same size. Although many of them were not in contact, they seemed to move as a whole, that is, they moved almost in the same direction and at the same velocity. Their positions relative to each other did change but at a much longer time scale. As time increased, several of them aggregated to form islands of droplets and the islands, in turn, accumulated to form larger ones. Meanwhile, their velocity as a whole reduced gradually with time. Later, with the droplets growing bigger and bigger, all islands merged and filled the whole field-of-view of the objective. Grain boundaries and packing defects were seen mostly between merged islands. Local rearrangements of some droplets were seen to reduce the defects and form larger grains. Almost no coalescence is observed even though they are closely-packed. Finally, the film dried up and water evaporated out of the pores through the top opening.

However, there are also differences. For the breath figure formed on an evaporating polystyrene solution (Figure 5.1), the water droplets in the islands were usually not very ordered (i.e., hexagonally packed) until all of the islands merged. By then, the water droplets rearranged themselves to get hexagonally packed so that all of the droplets could fit into the surface area of the solution, that is, two-dimensional close packing. Therefore, maximizing the packing density seemed to be more responsible for the final hexagonal-order of the array of water droplets (or later “air bubbles”) formed on

polystyrene solution. For the breath figure formed on an evaporating hexoPPE solution (Figure 5.2), however, the water droplets can rearrange themselves to form a hexagonal structure when there were more than two islands moving together. Most of the time, the droplets within isolated islands had already been in hexagonal packing, long before the islands merged, when they had enough empty space to fit in all of the droplets without the necessary of close packing.

If we assume that, at the stages in this study, the water droplets have already been in contact with the solution surfaces, capillary forces might be responsible for the close packing of water droplets on the hexoPPE solution before they occupied all of the two-dimensional space [12]. As discussed in Chapter 2, from the three-dimensional images of the macroporous films, we can infer that, when it was in contact with the polymer solution, a water droplet was in a lens shape suspended on the solution surface. Due to the very small size (on the order of several microns), it is reasonable to assume that the water lens consisted of two spherical segments with one below the solution surface and the other above, respectively in radius of R and R' as marked in Figure 5.4 [18]. Comparing the microscopic images of the porous films of polystyrene (Figure 5.5a) and hexoPPE (Figures 5.5b), we can see that the polymer wall between neighboring air pores is apparently thicker in the hexoPPE film than that in the polystyrene film. Similarly, apparently thicker polymer-solution wall can be seen between neighboring water droplets in a hexoPPE solution (Figure 5.6). Both of them indicate that a larger volume fraction of a water sphere was inside the solution. Therefore the water droplets (in the same diameter) bore larger buoyancy in a hexoPPE solution than in a PS solution.

Some simple calculations can be done to estimate the shape of the solution surface when there are water droplets suspending on it, by measuring the apparent radius (i.e., the radius of the bright spots) of the water droplets, *r*, and their real radius (i.e., half of the centre-to-centre distance of neighboring droplets), *R*, in Figure 5.6. Here we make an assumption that the neighboring water droplets are in close contact with each other. This assumption is good enough considering that there have already been some droplets pushed inside the solutions (the dark spots) as will be discussed later. In reality, there is probably a layer of solution in between but in a negligible thickness. The average values of *r* and *R* are measured to be 2.8 μm and 3.8 μm for the polystyrene-CS_2 solution (Figure 5.6a) and 2.7 μm and 4.4 μm for the hexoPPE-CS_2 solution (Figure 5.6b), respectively. Then the volume of the water droplets below the solution surface, V_{Low}, can be calculated using the geometrical relation for a spherical segment,

$$V_{\mathrm{Low}} = (\pi/3)\, h^2\, (3R - h), \tag{5.2}$$

where, *h* is the height of the segment,

$$h = \sqrt{R^2 - r^2} + R\,. \tag{5.3}$$

The calculated value of V_{Low} is 213.7 μm^3 for PS-CS_2 and 345.8 μm^3 for hexoPPE-CS_2. Using the density of CS_2 (ρ_{CS_2} = 1.26 g/cm^3) as that of the dilute polymer solutions, the buoyancy a water droplet experiences is about 2.6×10^{-12} N on the PS-CS_2 solution and 4.3×10^{-12} N on the hexoPPE-CS_2 solution. Comparing with the gravity, which are 2.25×10^{-12} N for a water sphere in a radius of 3.8 μm and 3.5×10^{-12} N for a water sphere in a radius of 4.4 μm (for rough estimation, assume that the water droplets are spheres although they should be lenses with the segments outside the solutions flattened depending on the interfacial tensions), we can see that, in both cases, the buoyancy is

only partially balanced by gravity so that the suspended water droplets protrude a little, which results in deformation of the solution surfaces as sketched in Figure 5.4. This protrusion is also kept in the final macroporous films (Figure 5.5b). In this way, a deformed solution surface exerts a downward force (i.e., the vertical vector of the surface tension force), combined with the gravity, to balance the upward buoyancy. Meanwhile, the horizontal vectors of the surface tension forces due to the deformation by the suspended water droplets tend to pull them together, causing attractive interactions so that they aggregated slowly. From the estimation above, we can see that the difference between buoyancy and gravity for a water droplet at the hexoPPE-CS_2 surface is 0.8×10^{-12} N, which is more than twice larger than that for a droplet at the PS-CS_2 surface (0.35×10^{-12} N). Therefore, the hexoPPE-CS_2 surface has to be more deformed to induce larger downward surface tension forces, which in turn leads to higher capillary forces (i.e., attractive interactions), so that the droplets pack themselves more compactly and faster.

Similar argument has been used by Steyer et al. [12] to explain the hexatic packing of water droplets formed on paraffin oil. In their case, water is denser than the substrate (i.e., paraffin oil) so that the liquid surface was curved by the suspended water droplets in an opposite direction.

As discussed in Chapter 1, about how water droplets get closely packed, one opinion (by Maruyama et al. [19]) is that, during a solvent-evaporation process, some of the condensed water droplets are dragged into the solution by convection and some float on the solution surface. With the solution drying from the edge to the center, water droplets are close packed by capillary forces generated at the solution front [19]. However, since our observations were performed at the center regions of the spread

liquid films (several centimeter square in area), and we observed the well-packed hexagonal arrays of the condensed water droplets before the films started to dry, the solution-front-packing mechanism proposed in Ref. 19 is not applicable to our case.

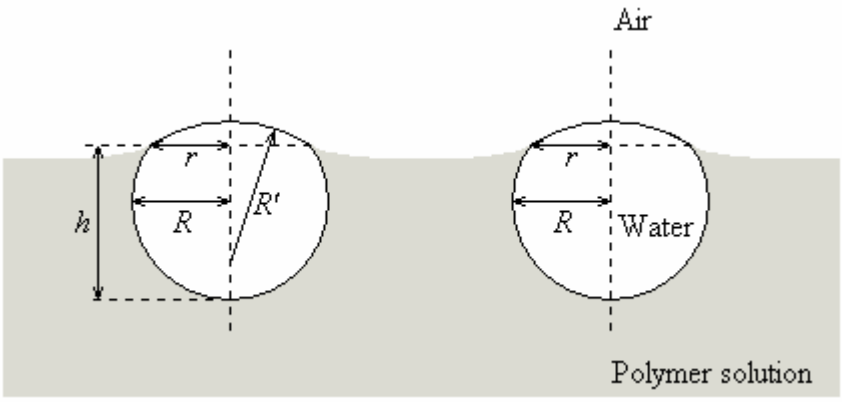

Figure 5.4 Equilibrium of water droplets suspended on a polymer solution with carbon disulfide as a solvent (the density of carbon disulfide is higher than that of water). Estimated based on the optical transmitted image of breath figures formed on the polymer solutions (Figure 5.6) and the consideration of a balance of buoyancy, gravity and capillary forces on the droplets as described in the text above. Due to the very small size (on the order of several microns), it is reasonable to assume that the water lenses are composed of two spherical segments (one is below the solution surface and the other above) in radius of R and R' as marked in the figure. The bending of the solution surface causes attractive interactions between the suspended water droplets so that they tend to form aggregates.

(a)

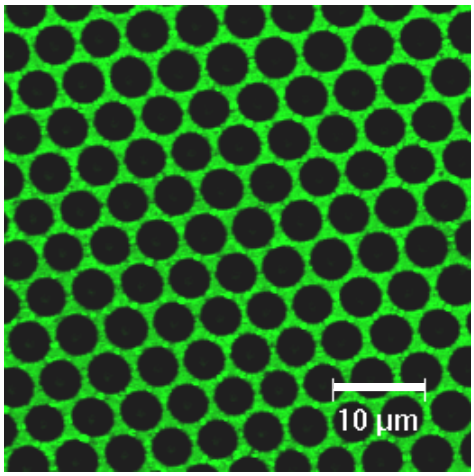

(b)

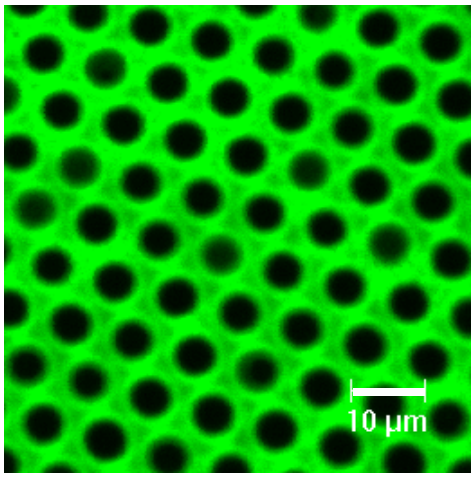

Figure 5.5 Top view of macroporous films cast from (a) polystyrene (~ 1 wt. %) and (b) hexoPPE (~ 0.2 wt. %) solution in carbon disulfide. The polymer wall between neighboring air pores is apparently thicker in the hexoPPE film. Imaged by a laser scanning confocal microscope (Leica TCS SP) in fluorescence mode with an objective of (a) 50× 0.75 dry and (b) 40× 0.75 dry, respectively. Scale bar: 10 µm.

(a)

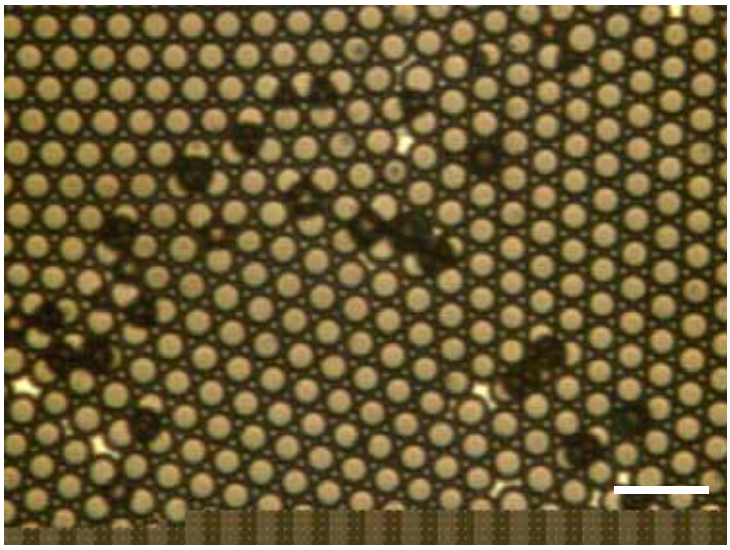

(b)

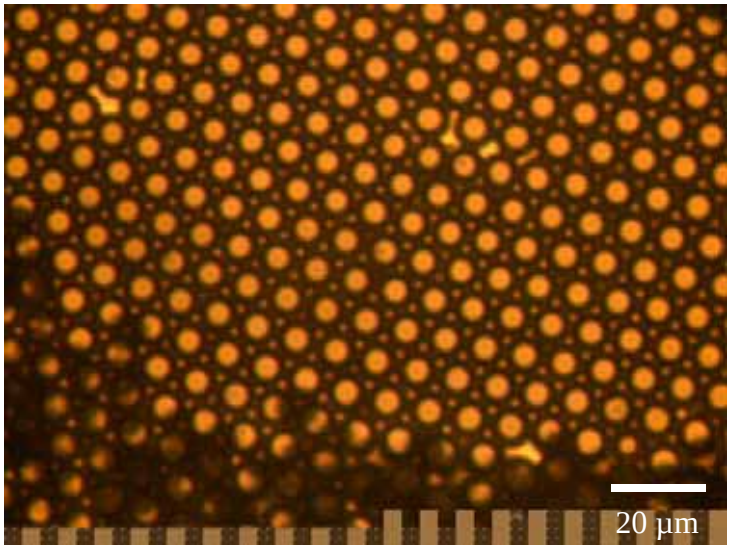

Figure 5.6 Selected frame of a recording of breath figure forming on a layer of (a) PS-CS_2 solution and (b) hexoPPE-CS_2 solution (Movie 5-2) by an optical microscope (Leica DMLSP, 50× 0.5 L) coupled with a high-speed digital camera (Photron FASTCAM-DVR). The polymer wall between neighboring water droplets is apparently thicker in the hexoPPE film. Scale bar: 20 μm.

5.3.2 Origin of Air Pores Underneath

As discussed in Sections 2.3.2.2 and 2.4.3, more or less, there are always some pores below the top ordered array of air bubbles in the macroporous films, leading to dark regions in the transmission microscopic images. Sometimes these pores are non-uniform and randomly dispersed, and sometimes relatively mono-sized and hexagonally packed. The origin of these air pores inside was revealed by observing the film forming process (see, for example, Movies 5-2 and 5-3).

In the movies, dark spots or small dark patches were seen to show up one by one or several by several after all of the islands merged, mostly along the borders of the merged islands. When we slightly over-raised the microscope stage so that the objective was focused on a plane slightly below the top array of water droplets, these dark areas were more focused and were clearly seen to be either dispersed or a cluster of several water spheres (Figure 5.7), which is similar to Figure 2.25b except that air bubbles replace water droplets there. After realizing these dark regions were water droplets underneath, the whole picture got clear. With the droplets continuously growing and the solution layer drying gradually from the edge to the center, the solution surface was not large enough to incorporate all of the droplets in the same horizontal plane. The droplets pushed against each other and rearranged themselves to try to utilize any possible space. Some water spheres occasionally lowered their positions, which can be due to convective currents or simply because of the pushing, so that they were rapidly punched inside the solution and, at the same time, the top layer of water droplets rearranged to occupy the evacuated space. These droplets can easily and quickly slide across each other (in less than 8 ms) and the solution layers in between may serve as lubricant. Figure 5.8 shows

that two water spheres were pushed inside (marked by a red circle) and the rest droplets finished their rearrangements within 16 ms.

Therefore, the pores below the top layer of air bubbles are, in principle, a result of dense packing of water droplets — the droplets can not fit all of themselves in one plane, i.e., two dimensions, so they expend to three dimensions.

For the multilayered macroporous films (with lower layers of pores being generally discontinuous and less ordered [20]) they sometimes obtained with carbon disulfide as a solvent, Pitois and François [20] suggested that the formation was due to the new water droplets nucleating and growing on the triangular solution-surfaces among closely-packed, earlier-condensed water droplets. However, in that case, the top layer of pores should be less ordered than the lower layers, which is opposite to the experimental observations. Besides, due to the condensation heat, the solution surface around the perimeter of a condensed water droplet is in higher temperature than the rest solution surface, which hinders the nucleation and growth of later-generation water droplets. Therefore, we suspect that the multilayered macroporous films sometimes obtained by Pitois and François and by other researchers [21-23] were formed in the same way as in our case.

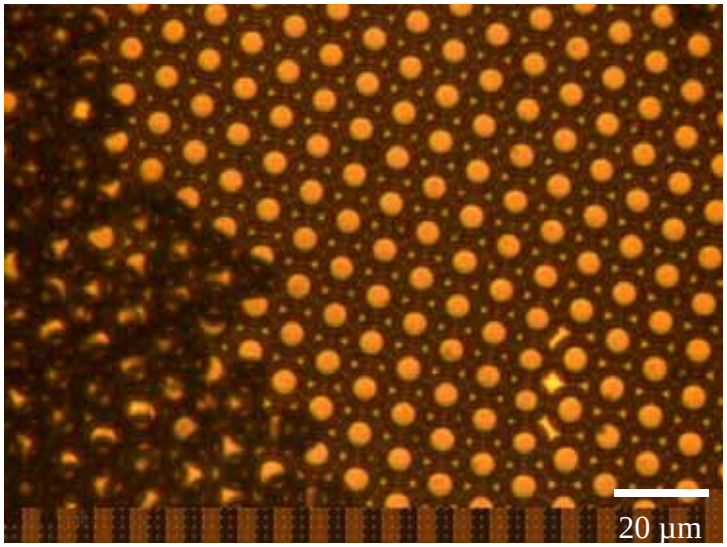

Figure 5.7 Water droplets underneath were seen more clearly when slightly raised the microscope stage so that the objective focused on a plane a little below the top array of water droplets. Selected frame of a recording of breath figure forming on a layer of hexoPPE-CS_2 solution (Movie 5-2) by an optical microscope (Leica DMLSP, 50× 0.5 L) coupled with a high-speed digital camera (Photron FASTCAM-DVR). They are comparable to Figure 2.3b where air bubbles replace water droplets.

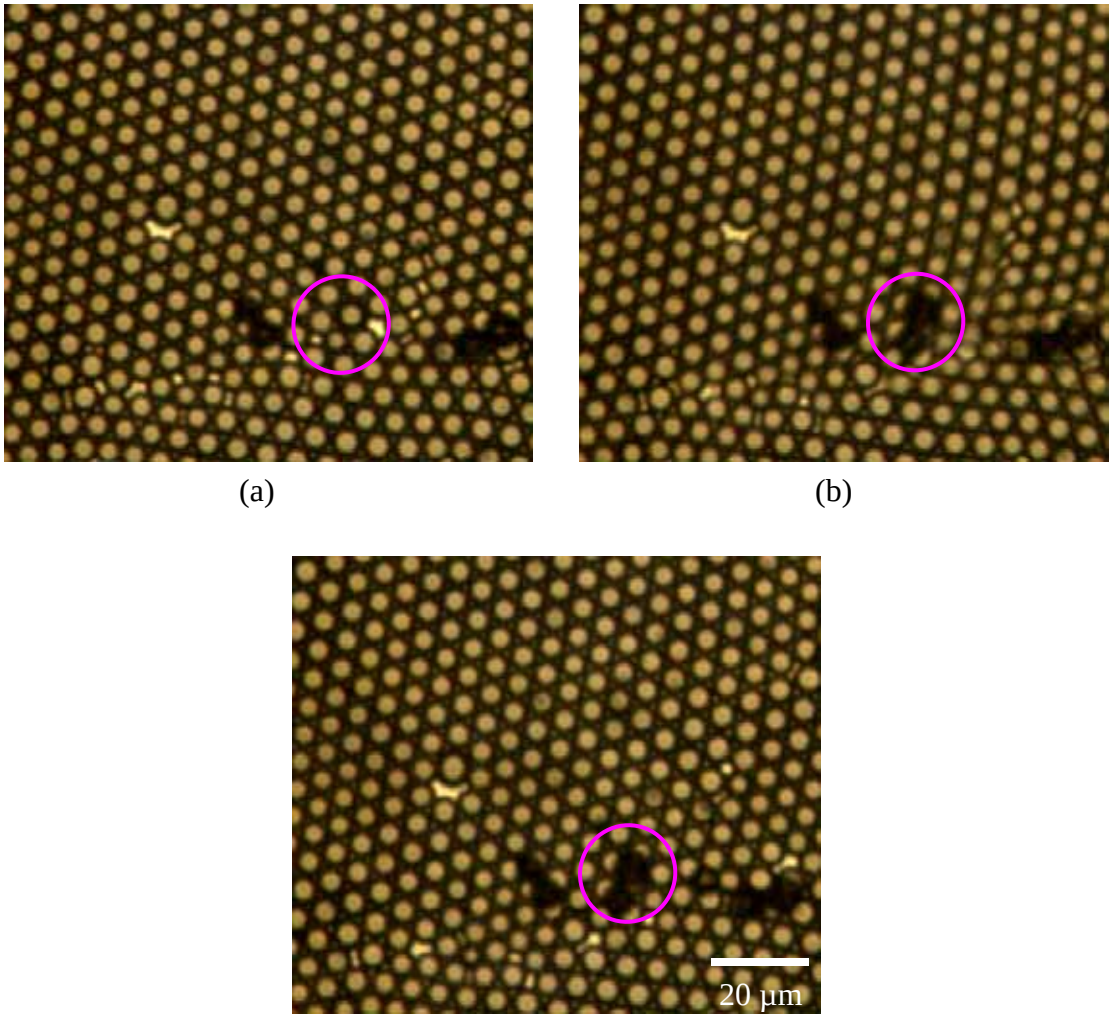

(a) (b)

(c)

Figure 5.8 Two water droplets (marked by a red circle) were pushed inside a solution during the packing of the droplet islands. Due to the buoyancy (the density of water is less than that of CS_2), they suspended right below the top layer of water droplets without sinking. Because they scatter light, those regions look darker when observed in transmission mode. Selected frames of a recording of breath figure forming on a layer of PS-CS_2 solution by an optical microscope (Leica DMLSP, 50× 0.5 L) coupled with a high-speed digital camera (Photron FASTCAM-DVR). The time duration between (a) and (b) and (b) and (c) is 8 ms. Frames were cropped to focus on regions of interest.

5.3.3 Merging of Water Droplets in Contact

As can be seen in the recordings, most of the time, water droplets did not coalesce even though they looked like in contact with each other and pushed against each other for more space. Coalescence did happen sometimes, however. Figure 5.9 shows two neighboring droplets merging in less than or equal to 16 ms. At the moment when Figure 5.9b was taken, the segments of the two water droplets below the solution surface had, probably, partially merged and, subsequently, the solution layer between the two were totally depleted and a bigger spherical droplet formed within 8 ms. By comparison, it took much longer time for the coalescence of two pairs of water droplets to complete in Figure 5.10. From Figure 5.10a to 5.10f, the time duration was 112 ms and there were still a polymer (or highly viscous polymer solution) bridge hung over the surface. This difference is reasonable because the merging shown in Figure 5.10 took place at a very late stage, right before the total drying (macroscopically) of the film, when the viscosity of the solution was much higher. In fact, merging of water droplets at late stages was very often seen in the recordings. Another example can be found by watching the end section of Movie 5-2; coalescence can be seen among those droplets underneath. The merging at the very late stage is probably responsible for the partially merged air pores we observed in some of the macroporous films (Figures 2.27-2.29) in Chapter 2. *All of these coalescence events seem to disagree with the conclusion by Pitois and François [20] that a layer of polymer precipitated at the water-solution interface so that the coalescence was prevented.*

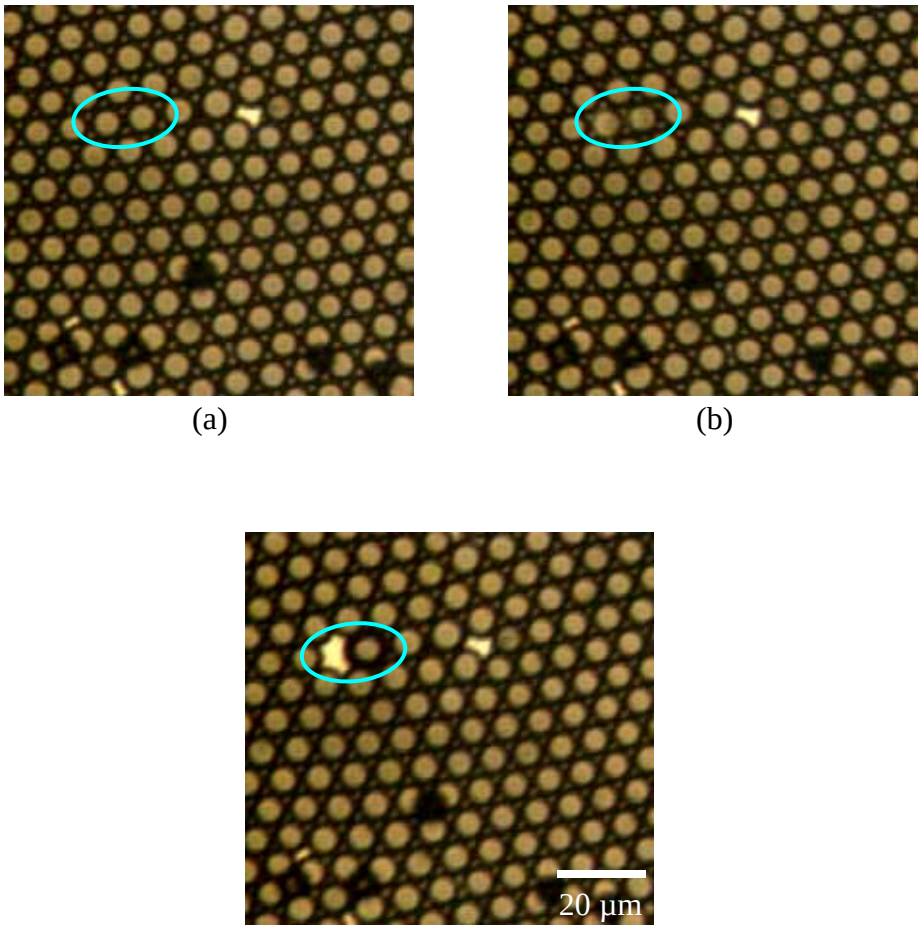

(a) (b) (c)

Figure 5.9 Coalescence of two water droplets (marked by a blue circle) during the film formation process. Comparing with the merging happened in Figure 5.10, it took a much shorter time here. Selected frames of a recording of breath figure forming on a layer of PS1c50-CS_2 solution by an optical microscope (Leica DMLSP, 50× 0.5 L) coupled with a high-speed digital camera (Photron FASTCAM-DVR). The time duration between consecutive frames is 8 ms from (a) to (c).

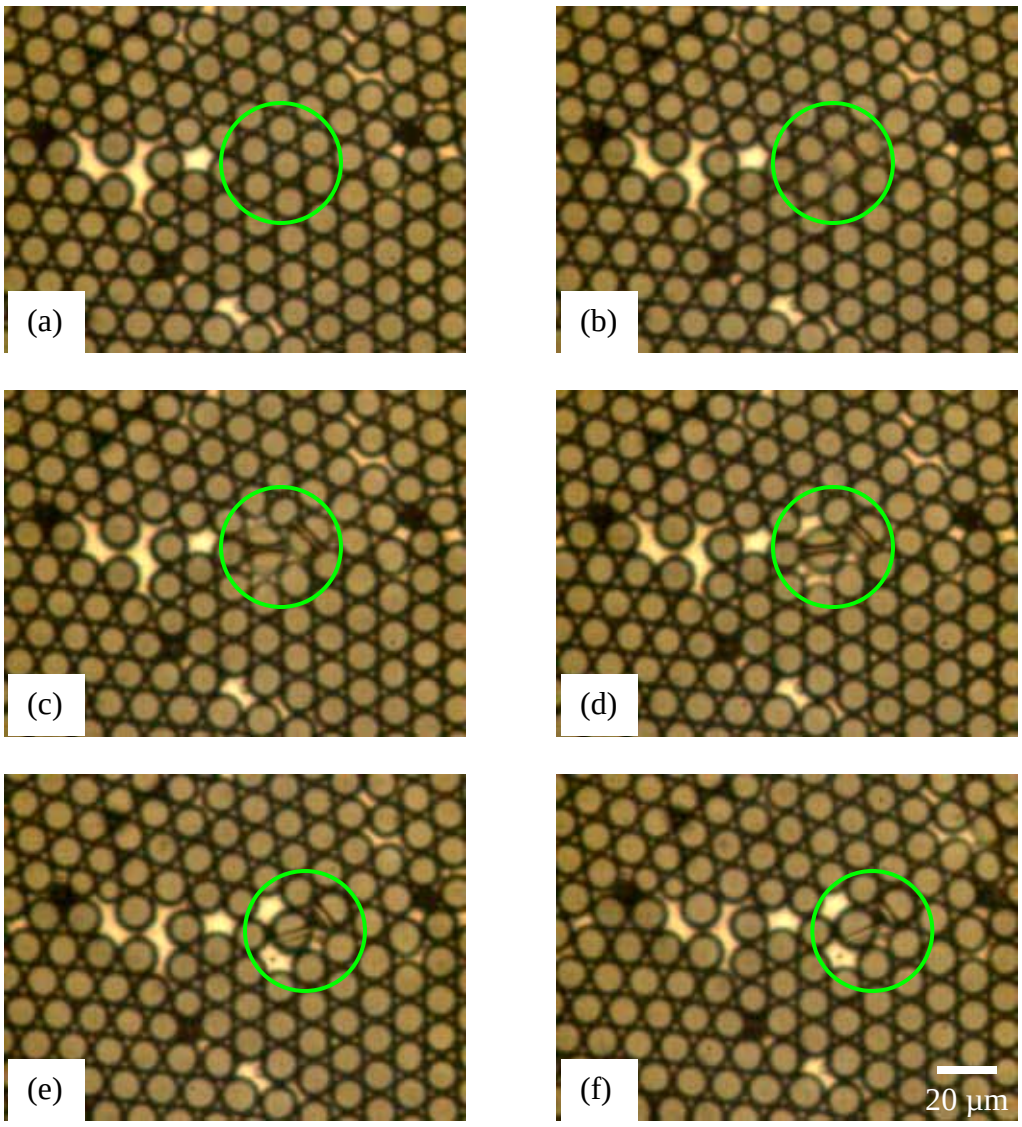

Figure 5.10 Coalescence of two pairs of water droplets (marked by a green circle) at a very late stage of the film formation process (right before it totally dried up). Comparing with the merging happened in Figure 5.9, it took a longer time here. Selected frames of a recording of breath figure forming on a layer of PS1c50-CS_2 solution by an optical microscope (Leica DMLSP, 50× 0.5 L) coupled with a high-speed digital camera (Photron FASTCAM-DVR). The time duration between consecutive frames is 8 ms from (a) to (d), 40 ms from (d) to (e) and 48 ms from (e) to (f).

5.3.4 Movement of Water Droplets at the Very Late Stage

Another noteworthy observation from the recorded movies of film formation process is that, right before the film dried up, the water droplets can still move, sometimes in a relatively high speed, without deformation, i.e., keeping the spherical shape without being elongated. This observation may serve as evidence that the concentration of the solution layer was still relatively low until it dried up so that an almost straight evaporation curve (mass vs. time) as discussed in Chapter 4.

5.3.5 Scaling of Breath Figures

In an effort to understand the growth laws that govern the growth of water droplets (and for comparison with the results obtained by other researchers [5-17]), we have measured the growth of the breath figures on our evaporating PS-CS_2 and hexoPPE-CS_2 solutions based on the recorded movies. Their log-log plots are given in Figure 5.3 with the linearly fitted trendlines (red lines). It can be seen, from the linearly fitted equations, that the growth of breath figure on PS-CS_2 can be fitted to a power law with an exponent of 0.4 (Figure 5.3a), while the log-log plot of breath figure on hexoPPE-CS_2 deviates from a straight line but the fitted exponent is around 0.3 which is close to the 1/3 law found by the other researchers [5-17].

In their experiments, Knobler and Beysens [5,6,9] assumed that the start of the nucleation of water droplets was the time when moisture was carried to the surface which was externally cooled to a stable working temperature by a Peltier element. That was reasonable since the temperature of the surface had already been below the dew point. In our case where the cooling of the substrate was via the solvent evaporation, however, the

substrate was in almost the same temperature (i.e., the room temperature) as the moist airflow at the beginning so that the nucleation should start some time later than the time when the moisture was blown onto the substrate. Also, because the position of the surface (so that the breath figure) changed continuously due to the fast evaporation of the solvent, coupled with the limitation of the resolution of an optical microscope, we were not able to get very clear images of the breath figures at the very early stage. Therefore, it is difficult for us to decide when the nucleation of the water droplets starts. However, the slope of the linear trendline (i.e., the exponent of the power law) is affected by the values of time, t. If $d = t^{\alpha}$ and $d = (t + \Delta t)^{\beta}$, α will not be equal to β except $\Delta t = 0$. Therefore, it is difficult to get the real information on the growth of the breath figures, in our case, from the log-log plot of the average diameters of the water droplets vs. time.

Theoretically, the 1/3-power relation between the diameter of a growing water droplet and time is equivalent to the case when the volume changing rate of a water droplet is a constant, that is, dV/dt is a constant [11,14]. Thus, the volume of a droplet, V, is a linear function of time, t, so that the choice of the starting time will not affect the profile of V as a function t. Following this thought, we re-plotted our data in the values of d^3 vs. t (Figure 5.11). It can be seen that, the volume increase of water droplets on the PS-CS_2 solution was almost a constant so that there was a constant volumetric flux of moisture condensing on the surface over time. By comparison, the volume growth of breath figure on the hexoPPE-CS_2 solution seemed to be slower in an intermediate stage than the earlier and later stage.

According to the expression by Beysens et al. [11] (or Eq. 5.1),

$$dV/dt \sim D_{12} \Delta T_s^{0.8} \delta^{-1} \tag{5.4}$$

where δ is the thickness of the boundary layer of moisture concentration. For the time changing rate of volume of condensed water to be independent of time (or the 1/3-power law of diameter over time), the condensation process should be at a steady state, that is, D_{12}, ΔT_s and δ are independent of time. Here, in our case, the solvent evaporates throughout the whole film-formation process. Since the cooling of the substrate is caused by the evaporation, the temperature difference between the moisture in the airflow and the substrate, ΔT_s, should not be a constant at the initial stage. However, the heat loss due to evaporation, different heat transfer processes (including diffusion and convections), especially those speeded up by the fresh airflow and the heat gain due to the condensation (which is a minor effect as discussed in Chapter 4), the system heat may reach equilibrium so that ΔT_s is almost a constant at some stage. The linearity of the weight loss curve in the evaporation rate measurement seems to suggest this equilibrium. Due to the multi-processes involved in a film-forming process, it is difficult to theoretically predict the temperature profile on the solution surface. Experimental measurement may be needed to further understand the whole process.

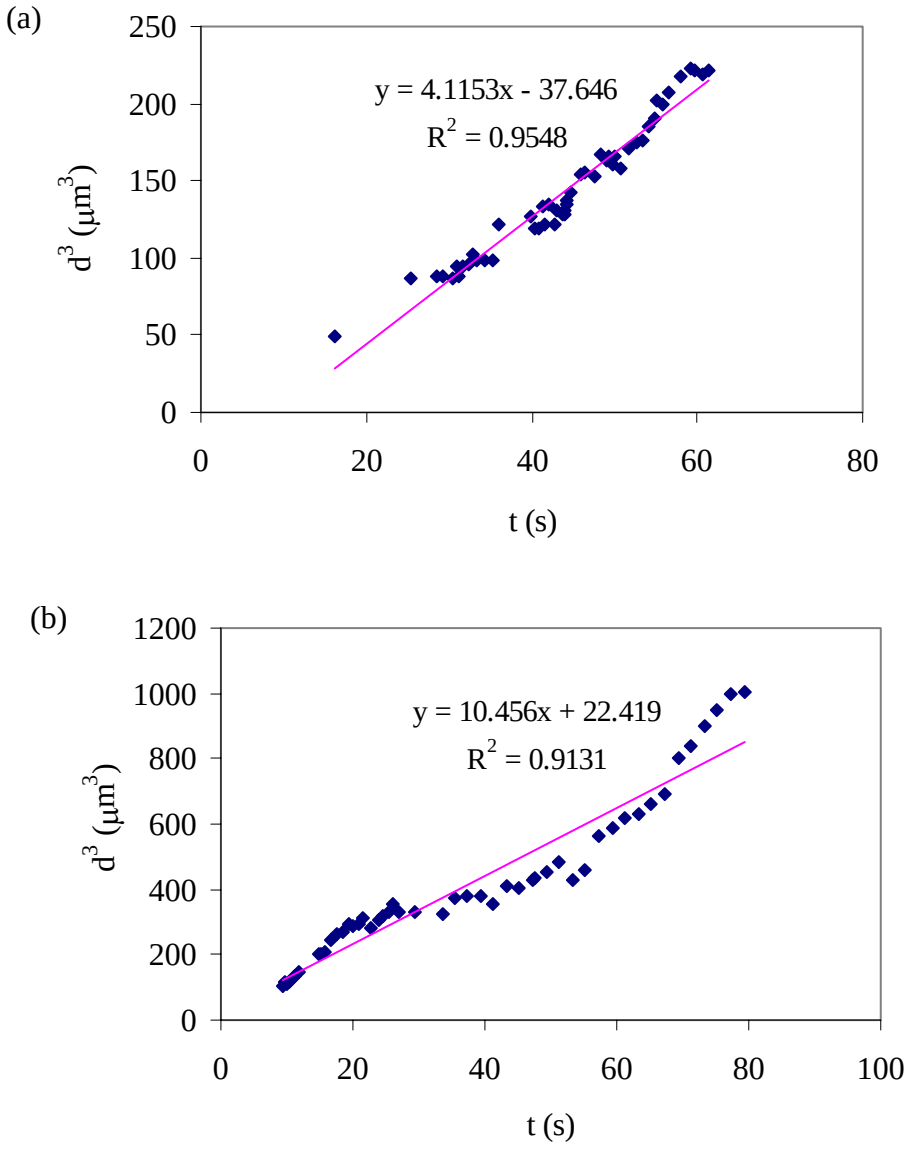

Figure 5.11 Average volume (normalized by $\pi/6$) of water droplets, d^3, as a function of time, t. Linear trendlines (red lines) are drawn with the fitted equations post next to the lines. Breath figures were formed on a layer of (a) PS-CS_2 solution (Movie 5-1) and (b) hexoPPE-CS_2 solution (Movie 5-2). Here, the values of time are relative because it was hard to tell the exact time when water vapor nucleated.

5.3.6 Track of a Water Droplet

As mentioned above, at the earlier stages of the macroporous film forming process, the pattern of the condensed water droplets was often seen to move as a whole, i.e., the positions of condensed droplets were relatively fixed relative to the surrounding droplets during a short period. Therefore, we can mark a single droplet based on the features of its neighbors and follow its position frame by frame to quantitatively characterize its motion, and its motion should be able to represent the motions of other droplets within the patterns. Figures 5.12 and 5.14 are two examples of the droplet-tracking analyses with Figures 5.13 and 5.15, respectively. In both cases, droplets were moving from left to right of the field-of-view of the objective and finally went beyond. As can be seen from Figures 5.12a and 5.14a, the direction and moving distance in each step (8 ms between each measurement) can be very different from time to time. Although the first one (Figure 5.12a) seemed to move in the vertical direction during its motion from left to right, the second one (Figure 5.14a) was almost moving in a straight line from left to right at the beginning and then started to hang around at the right of the field-of-view of the objective for quite a while. Actually, the frames used for the particle-motion study in Figures 5.12 and 5.14 are selected from the same recordings and they are connected in the time scale (Figure 5.12 ended at t = 10.2 s and Figure 5.14 started at t = 10.2 s). The only difference between the two is that the droplet under tracking — the first droplet under tracking moved out of field-of-view at the end of Figure 5.12 so the second droplet was used to continue tracking the motion of the breath figure in Figure 5.14.

Another interesting phenomenon to notice is that the maps of their shift distance (every 8 ms) over time are wavelike (see Figures 5.12b and 5.14b), reminiscent of

propagation of sound in air (longitudinal waves). By finding out whether a particle suspended on an evaporating polymer-solution surface with airflow across the solution surface has this kind of signature movement or not, useful information can be conjectured on whether these water droplets are suspended on the solution surface or levitated above it.

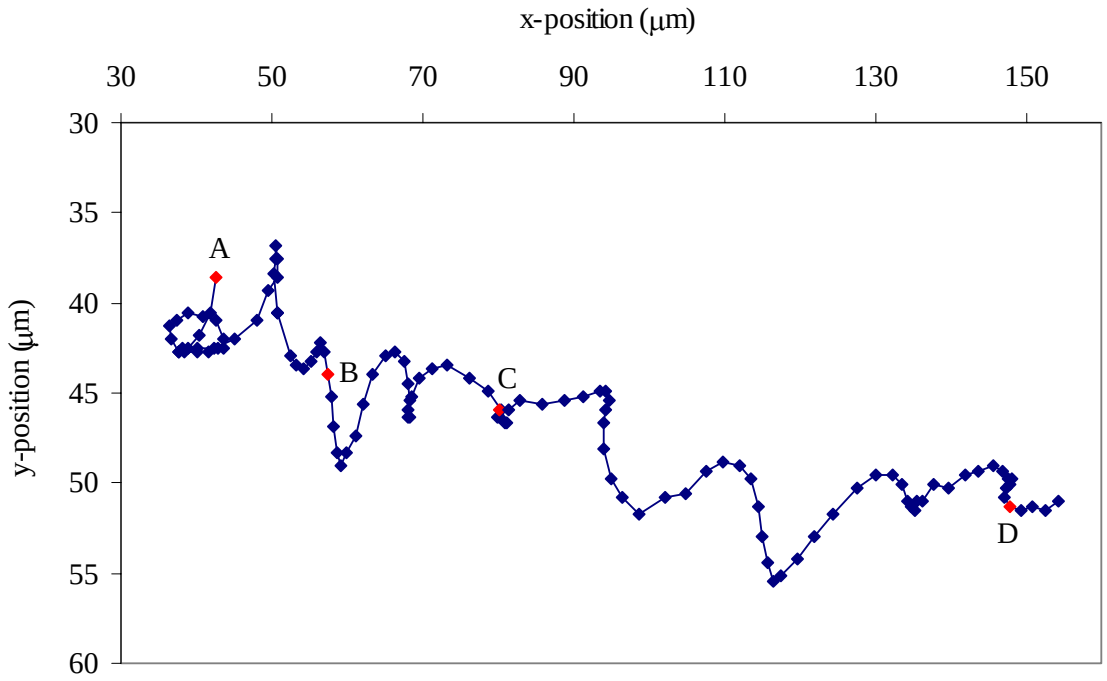

(a)

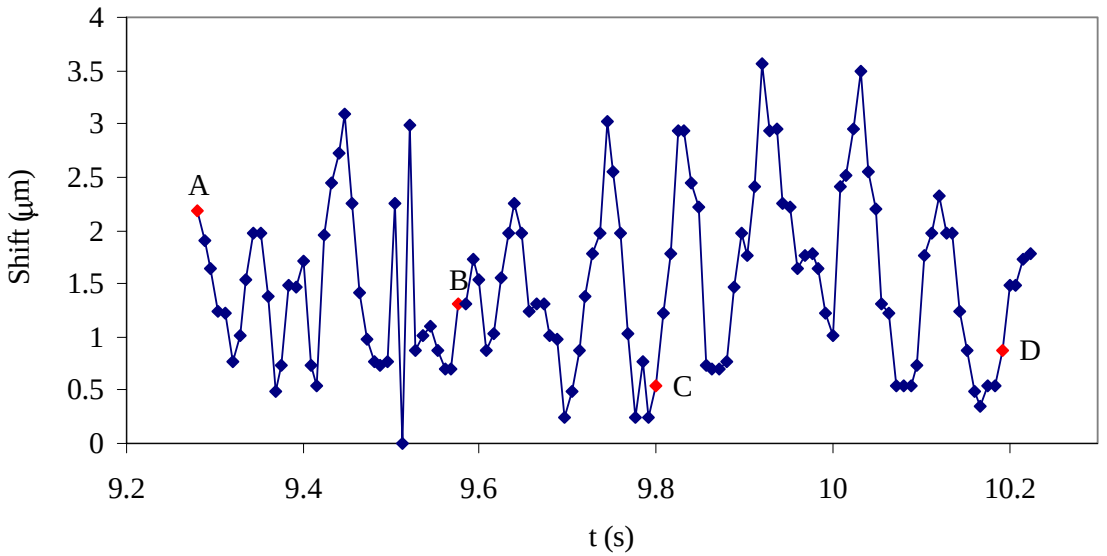

(b)

Figure 5.12 (a) Track of a water droplet on a layer of hexoPPE-CS_2 solution (based on selected frames of Movie 5-2). The time duration between consecutive steps is 8 ms. (b) Shift distance of every step of the water droplet as a function of time. A, B, C and D are randomly selected moments with their corresponding images given in Figure 5.13.

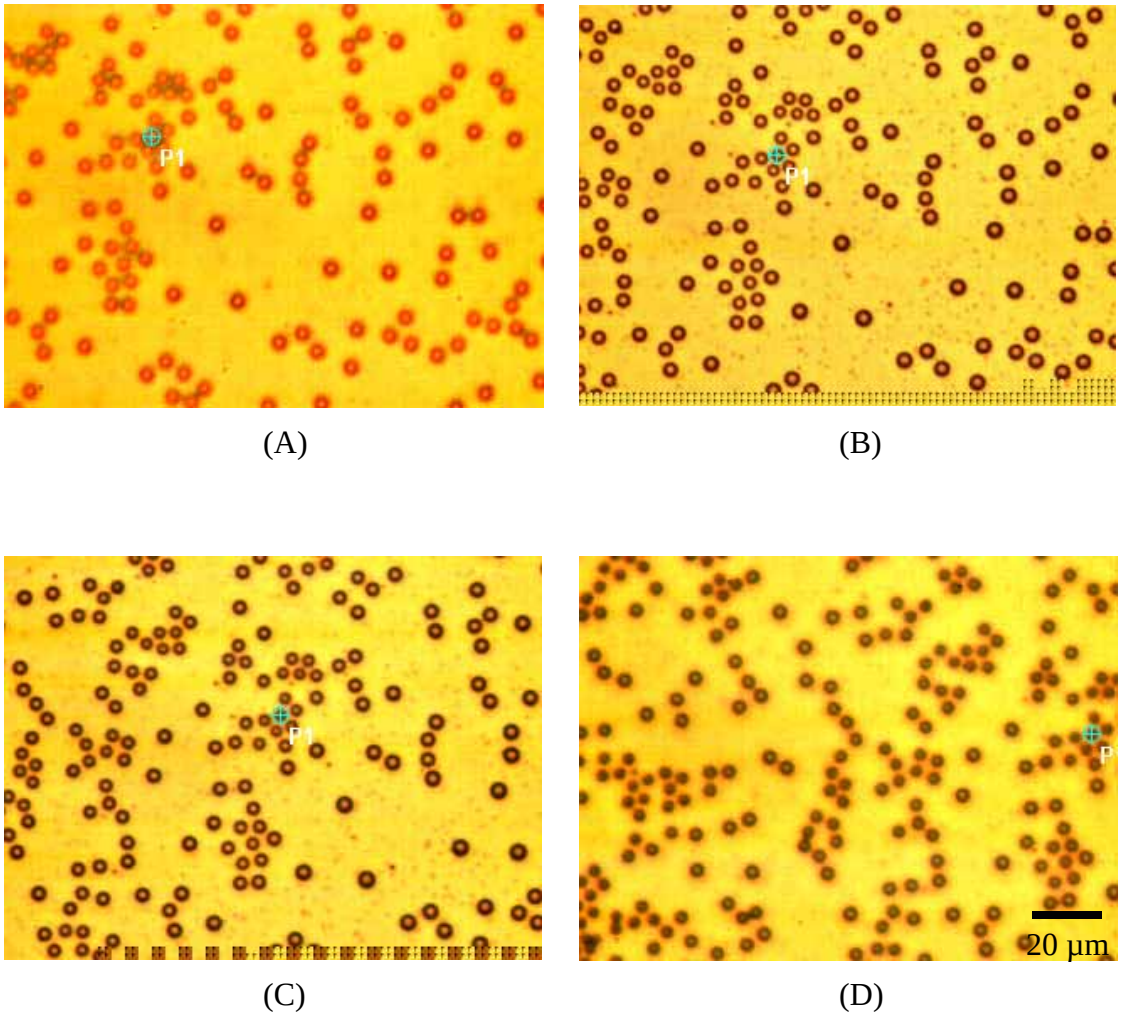

(A) (B)

(C) (D)

Figure 5.13 Breath figure formed on a layer of evaporating polymer solution (hexoPPE-CS_2). Selected image frames of Movie 5-2 for a particle-tracking analysis with the water droplet that was tracked in Figure 5.12 marked with a blue cross. The A, B, C and D images here correspond to the A, B, C and D points marked in Figure 5.12, respectively. Scale bar: 20 µm.

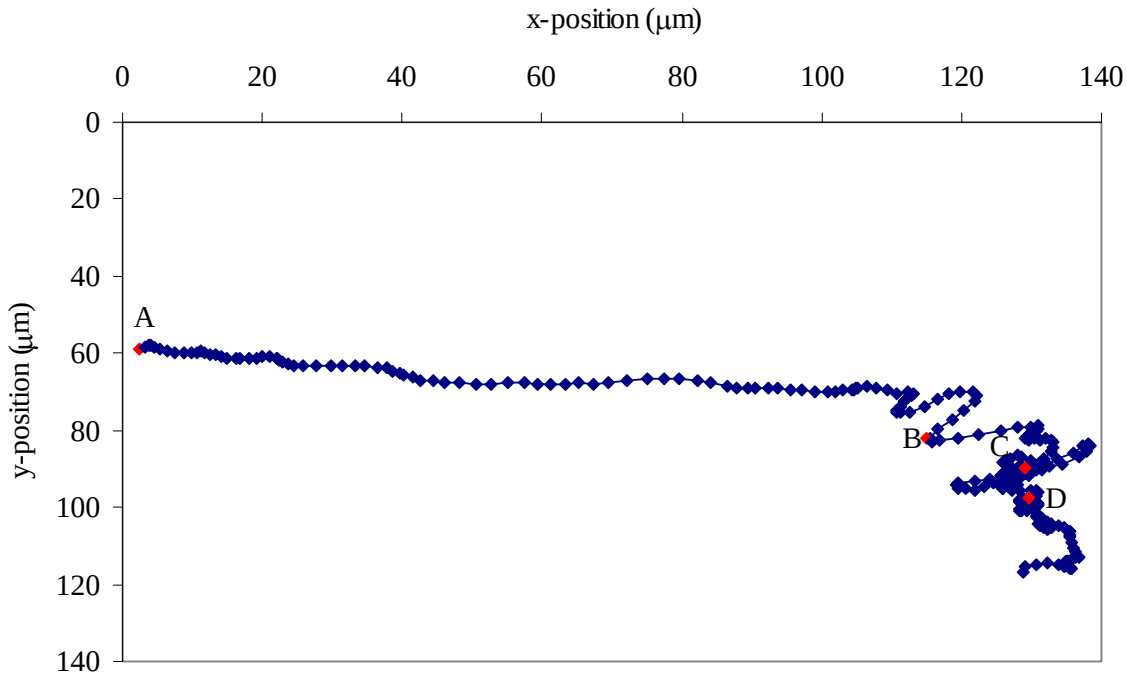

(a)

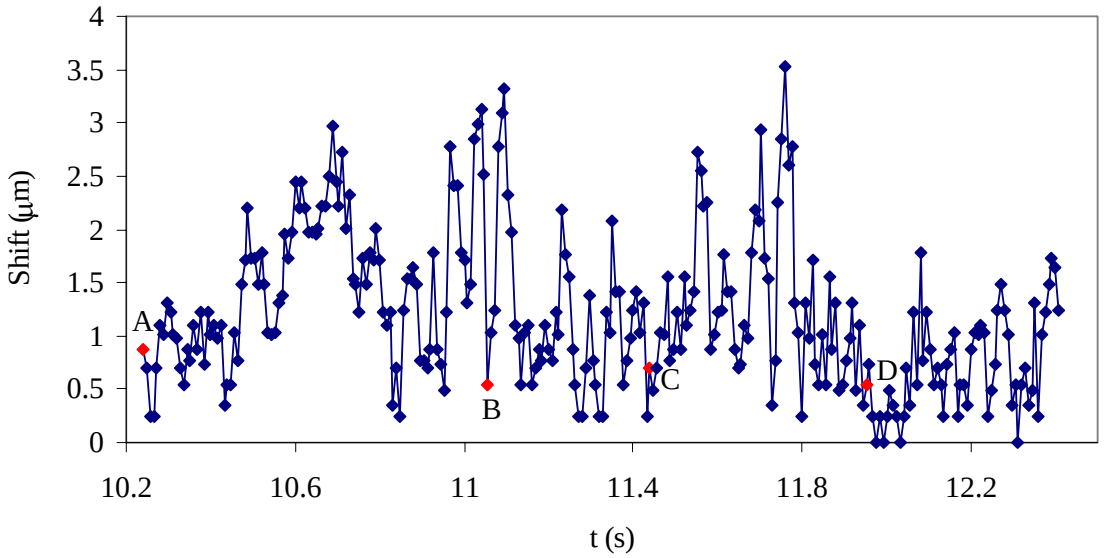

(b)

Figure 5.14 (a) Track of a water droplet on a layer of hexoPPE-CS_2 solution (based on selected frames of Movie 5-2). The time duration between consecutive steps is 8 ms. (b) Shift distance of every step of the water droplet as a function of time. A, B, C and D are randomly selected points with their corresponding images given in Figure 5.15.

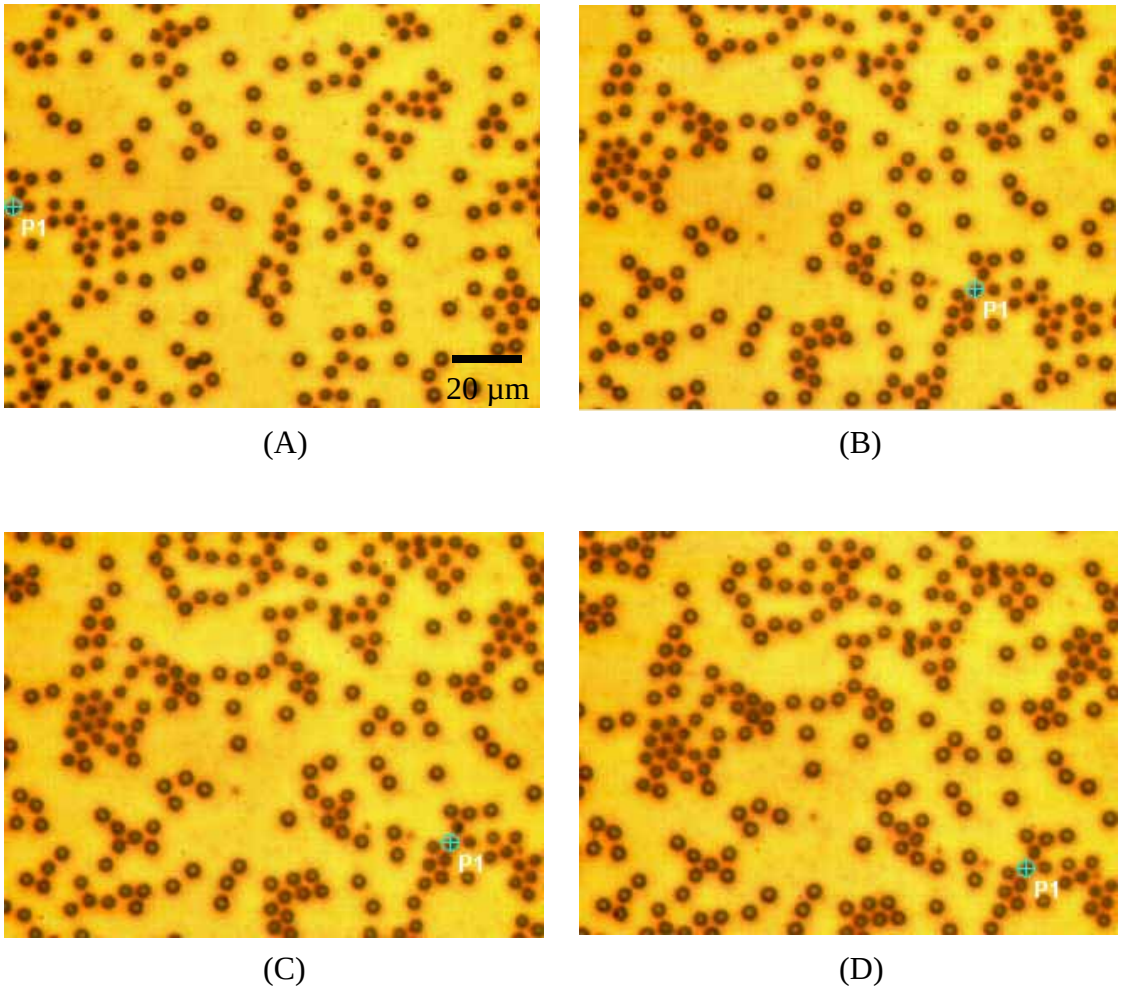

Figure 5.15 Breath figure formed on a layer of evaporating polymer solution (hexoPPE-CS_2). Selected image frames of Movie 5-2 for a particle-tracking analysis with the water droplet that was tracked in Figure 5.14 marked with a blue cross. The A, B, C and D images here correspond to the A, B, C and D points marked in Figure 5.14, respectively. Scale bar: 20 µm.

5.4 Conclusions

In conclusion, we have recorded breath figures formed on evaporating polymer solutions under the conditions at which ordered macroporous films were prepared. Replaying these recordings at lower speeds revealed many interesting features. Especially, the air bubbles below the top arrays as seen in many of our macroporous films were found to be from the water droplets which were pushed inside the solution as a result of over-packing, that is, more droplets than which can be packed in a two-dimensional surface. Our observations of well-ordered hexagonal patterns of water droplets at the center regions of the solution films before the films started to dry preclude the mechanism of hexagonal packing by capillary forces generated at the drying fronts. We did occasionally see some neighboring water droplets coalesce, sometimes at the very late stage, which seems to disagree with the suggestion that precipitated polymer layers at the water-solution interfaces prevented the coalescence of breath figures. Breath figure on a hexoPPE-CS_2 solution was found to form a more compact structure (i.e., hexagonal packing) than that on PS-CS_2 before the droplet islands totally merged. An explanation for it based on capillary forces induced by deformed solution surfaces has been attempted. Also, direct measurements on the movie frames via computer software showed that the growth of these breath figures more or less followed the 1/3 scaling law.

5.5 Recommendations

As discussed in Section 5.3.6, the consecutive movements (shift distances) of a water droplet within the same duration are wavelike. Further experiments and simulations can be done to figure out whether a particle levitated above an evaporating liquid

substrate or suspended on the surface of the liquid substrate shows this kind of movement, when airflow is blown across the liquid surface. By comparing the data with the results on condensed water droplets we obtained here, useful information can be conjectured on these water droplets are suspended on the solution surface or levitated above it.

References:

[1] Lord Rayleigh, "Breath figures", *Nature* **86**, 416 (1911).

[2] Lord Rayleigh, "Breath figures", *Nature* **90**, 436 (1912).

[3] J. Aitken, "Breath figures", *Nature* **86**, 516 (1911).

[4] J. T. Baker, "Breath figures", *Phil. Mag.* **S. 6. 44**, 752 (1922).

[5] C. M. Knobler and D. Beysens, "Growth of breath figures on fluid surfaces", *Europhys. Lett.* **6**, 707 (1988).

[6] D. Beysens and C. M. Knobler, "Growth of breath figures", *Phys. Rev. Lett.* **57**, 1433 (1986).

[7] J. L. Viovy, D. Beysens and C. M. Knobler, "Scaling description for the growth of condensation patterns on surfaces", *Phys. Rev. A* **37**, 4965 (1988).

[8] A. Steyer, P. Guenoun, D. Beysens and C. M. Knobler, "Two-dimensional ordering during droplet growth on a liquid surface", *Phys. Rev. B* **42**, 1086 (1990).

[9] D. Fritter, C. M. Knobler and D. A. Beysens, "Experiments and simulation of the growth of droplets on a surface (breath figures)", *Phys. Rev. A* **43**, 2858 (1991).

[10] A. Steyer, P. Guenoun, D. Beysens and C. M. Knobler, "Growth of droplets on a substrate by diffusion and coalescence", *Phys. Rev. A* **44**, 8271 (1991).

[11] D. Beysens, A. Steyer, P. Guenoun, D. Fritter and C. M. Knobler, "How does dew form", *Phase Transitions* **31**, 219 (1991).

[12] A. Steyer, P. Guenoun and D. Beysens, "Hexatic and fat-fractal structures for water droplets condensing on oil", *Phys. Rev. E* **48**, 428 (1993).

[13] B. J. Briscoe and K. P. Galvin, "The evolution of a 2D constrained growth system of droplets — breath figures", *J. Phys: D* **23**, 422 (1990).

[14] B. J. Briscoe and K. P. Galvin, "An experimental study of the growth of breath figures", *Colloids and Surfaces* **56**, 263 (1991).

[15] A. V. Limaye, R.D.Narhe, A. M. Dhote and S. B. Ogale, "Evidence for convective effects in breath figure formation on volatile fluid surfaces", *Phys. Rev. Lett.* **76**, 3762 (1996).

[16] O. Pitois and B. François, "Crystallization of condensation droplets on a liquid surface", *Colloid. Polym. Sci*. **277**, 574 (1999).

[17] O. Karthaus, M. Shimomura, X. Cieren, M. Shimomura, H. Hasegawa and T. Hashimoto, "Water-assisted formation of micrometer-size honeycomb patterns of polymers", *Langmuir* **16**, 6071 (2000).

[18] H. M. Princen, "The equilibrium shape of interfaces, drops, and bubbles. Rigid and deformable particles at interfaces", in *Surface and Colloid Science*, edited by E. matijevic, Vol. 2, (Wiley-Interscience, New York, N. Y.) 1969.

[19] N. Maruyama, T. Koito, J. Nishida, T. Sawadaishi, X. Cieren, K. Ijiro, O. Karthaus and M. Shimomura, "Mesoscopic patterns of molecular aggregates on solid substrates", *Thin Solid Films* **327-329**, 854 (1998).

[20] O. Pitois and B. Françis, "Formation of ordered micro-porous membranes", *Eur. Phys. J. B* **8**, 225 (1999).

[21] G. Widawski, M. Rawiso and B. François, "Self-organized honeycomb morphology of star-polymer polystyrene films", *Nature* **369**, 387 (1994).

[22] T. Hayakawa and S. Horiuchi, "From angstroms to micrometers: self-organized hierarchical structure within a polymer film", *Angew. Chem. Int. Ed.* **42**, 2285 (2003).

[23] P. S. Shah, M. B. Sigman, Jr., C. A. Stowell, K. T. Lim, K. P. Johnston and B. A. Korgel, "Single-step self-organization of ordered macroporous nanocrystal thin films", *Adv. Mater.* **15**, 971 (2003).

CHAPTER 6

STRUCTURE EFFECT ON WETTING PROPERTIES

Wetting phenomena have been studied for a long time, and is important in many practical applications. One example is the coating/painting process [1], where complete wetting is desired. Recently, roughness-induced non-wetting (especially of water) has received increased attention, which may be utilized to control motion of fluids in microfluidic devices [2] as well as to fabricate water-repelling surfaces. Also, it was found that the structure-induced super-hydrophobic surfaces in nature (such as insect wings [3] and lotus leaves [4]) is highly effective in the removal of particulate contaminates by rain — water drops can easily pick up tiny particles and roll off the surfaces, which is sometimes called "lotus effect" or "self-cleaning effect" [4]. This further extends the applications of these non-wetting surfaces to the ones where contamination is an issue and water can be applied for cleaning. Self-cleaning windows [5] and decorative surfaces [6] have been suggested.

To study the wetting properties of rough surfaces, especially roughness-induced non-wetting surfaces, several model surfaces with controlled microscopic structures have been prepared and studied. (i) Bico et al. [7] prepared surfaces with three kinds of micro-structures (regularly spaced shallow cavities, stripes and spikes, typical size is one micron) by molding sol-gel silicate on silicon wafers using elastomeric molds with reversed patterns. Monolayers of fluorosilane were grafted to make the surfaces hydrophobic. (ii) Öner et al. [8] prepared a series of silicon oxide surfaces with hexagonally-arrayed square posts varying in size (2×2 μm^2 to 128×128 μm^2) and height (20 μm to 140 μm) using

photolithographic techniques. They also made surfaces with array of posts which have shapes other than square to adjust contact lines. The surfaces were made hydrophobic by reaction with silanization reagents. (iii) Nakae et al. [9] made a hemispherical close-packed model surface and a hemiround-rod closed-packed one by coating small steel ball bearings and fine glass round rods on glass plates with an ether solution. (iv) Shiu et al. [10] prepared a series of surfaces of hexagonally arrayed polystyrene beads (monodisperse, 190 nm - 440 nm) by spin-coating followed by nanosphere lithography. They also modified the surfaces by coating a gold film (20 nm thick) followed by reaction with octadecanethiol to render the surfaces hydrophobic.

We have also studied the wetting properties of our macroporous polymer films. On one hand, since our macroporous films have highly ordered micro-structures, it can serve as another kind of model surfaces to study effect of roughness on wetting. It is impossible to make such a model surface (close-packed arrays of segments of spherical pores) by lithographic methods described above. On the other hand, it is important to study wetting properties of the films for their future applications. One example is related to the application in biology such as cell culturing and tissue engineering [11,12]. We may want to ask whether water goes into the pores if we put a drop of water solution with viruses in it, or whether the air pores can serve as micron-sized reservoirs of water solutions.

6.1 Basic Theories on Wetting

Contact angle θ is the most widely used and a convenient parameter to characterize wetting. Complete wetting happens when $\theta = 0°$, partial wetting when $0° < \theta < 90°$, partial non-wetting when $90° < \theta < 180°$, and complete non-wetting when $\theta = 180°$.

When a drop of liquid is placed on an ideal flat, smooth and homogeneous solid surface, the contact angle is given by the well-known Young's equation [13]

$$\cos\theta = \frac{\gamma_{SV} - \gamma_{SL}}{\gamma_{LV}}, \tag{6.1}$$

where, the contact angle θ is considered as the result of the mechanical equilibrium of three interfacial tensions, γ_{SV}, γ_{SL} and γ_{LV} (Figure 6.1); and the subscripts SV, SL, LV represent the solid-vapor, solid-liquid and liquid-vapor interfaces, respectively [13].

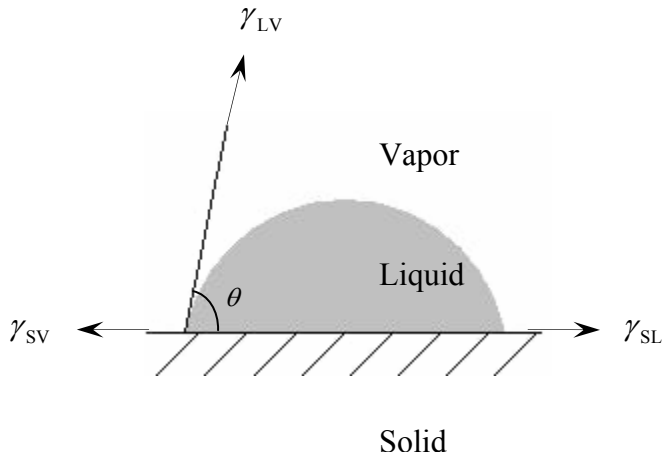

Figure 6.1 A liquid drop makes a contact angle θ on an ideal solid surface, as a result of the mechanical equilibrium of three interfacial tensions, γ_{SV}, γ_{SL} and γ_{LV}. The relation of them is expressed by Young's equation.

When a liquid drop is deposited on a rough surface, depending on the wetting properties of a flat surface of the same material and the roughness, there are typically three possibilities [14].

(i) Air is enclosed inside the roughness so that the liquid drop is actually sitting on a composite surface of solid and air (Figure 6.2a). Cassie and Baxter [15] have studied this case and derived the following expression [15]

$$\cos\theta^{c} = f_{s}\cos\theta^{*} - f_{air}, \tag{6.2}$$

where, θ^{c} is the apparent contact angle the liquid makes on the porous surface in Cassie's case, θ^{*} is the intrinsic contact angle of the liquid on a flat surface, f_{s} and f_{air} are areas of solid-liquid interface and liquid-air interface, respectively, normalized by total projected area on the surface.

(ii) Liquid fills the roughness below the sessile drop (i.e., the solid is dry outside the contact line, see Figure 6.2b). In this case, the apparent and intrinsic contact angles are related by Wenzel's equation [16]

$$\cos\theta^{w} = r\cos\theta^{*}, \tag{6.3}$$

where, θ^{w} is the apparent contact angle the liquid makes on a rough surface in Wenzel's case, r is the roughness of the surface, defined as the ratio of the actual solid-liquid area to the projected area on the surfaces.

(iii) Liquid not only fills the roughness below the sessile drop, but also impregnates outside the contact area the sessile drop makes on the solid (Figure 6.2c), this is sometimes called "surface wicking" [17] or "semi-wicking" [14]. In this case, again, the sessile drop can be considered to sit on a composite surface as in case (i), while here the surface is composed of solid and liquid (the same as the sessile drop), instead of

solid and air. Therefore, the apparent contact angle can be expressed as area-averaged cosines of contact angle of the two components [14]

$$\cos\theta^{s} = f_s \cos\theta^{*} - f_l \cos 0^{\circ} = f_s \cos\theta^{*} + f_l, \tag{6.4}$$

where, θ^{s} is the apparent contact angle the liquid makes on the composite surface in the surface-wicking case, f_s and f_l are, respectively, areas of solid-liquid interface and liquid-liquid interface (with a contact angle of 0°) normalized by total projected area on the surface.

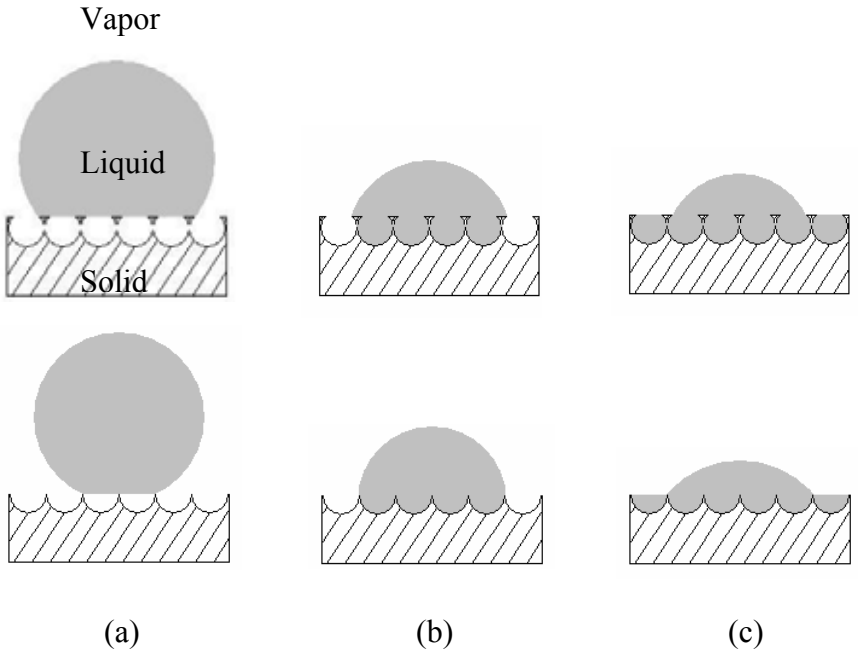

Figure 6.2 Three scenarios when a drop of liquid is placed on a rough surface. (a) Air is trapped inside the roughness so that the sessile drop is sitting on a composite surface of solid and air. (b) Liquid fills up the roughness below the drop only, without wetting the solid outside the contact line. (c) Liquid impregnates the solid outside the contact line as well as fills up the roughness below the drop ("surface wicking").

6.2 Experiments

Macroporous films with hexagonally-ordered arrays of air bubbles were prepared on microscope glass slides and cover glasses using the method described before (see Chapter 2.1). Here, polystyrene (Mono-carboxyl-terminated, M_w = 50,000; Scientific Polymer Products, New York) and carbon disulfide (Reagent A.C.S., Fisher Scientific) were used. Then the glass slides with macroporous as-cast films were cut in half. While one half was kept intact, the top of the other half film was carefully peeled off by a Scotch tape to prepare a surface with closely-packed hemispherical pores (Figure 6.3). For comparison, flat, smooth, solid films were prepared by casting the same polymer solutions in dry air flow.

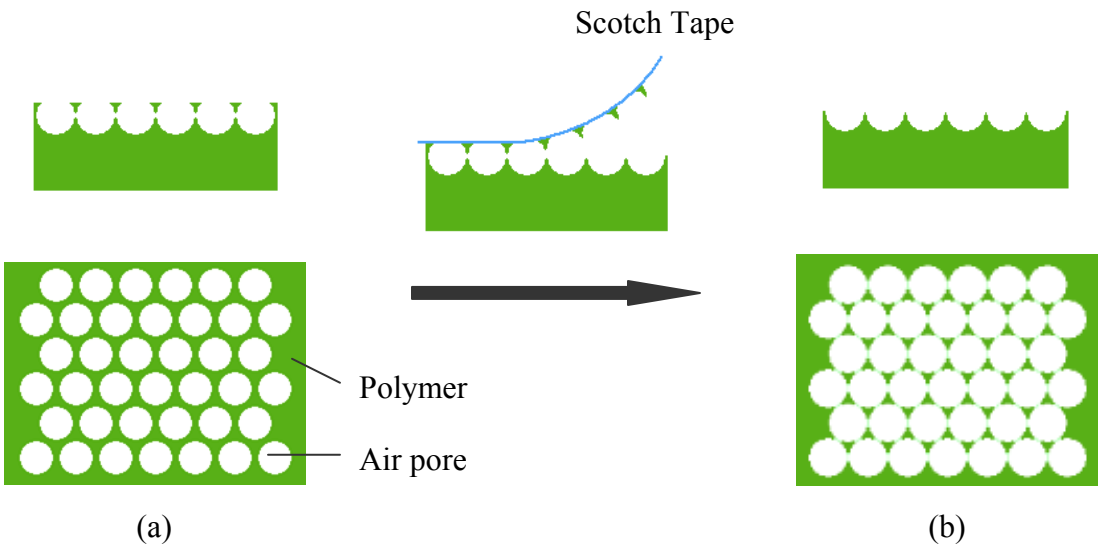

Figure 6.3 Schematics of macroporous films as cast (left) and peeled by a Scotch Tape (right). The upper sketches are side view and the lower ones are top view.

Contact angles (advancing and receding) of distilled water on the macroporous as-cast films, the top-peeled films and the flat solid films made of the same polymers were measured by a contact angle goniometer (Model 200, Ramè-Hart, Inc.) coupled with an automated dispenser. For the measurement of advancing contact angle, a drop of water was placed on the surface of a film, then a small amount (0.8 μL) of water was rapidly injected into the water drop and the contact angle was measured. This injecting and measuring procedure was repeated several times until the reading of the contact angle reached a maximum and reproducible value. Similarly, receding contact angle was measured by rapidly withdrawing a small amount (0.8 μL) of water out of the sessile drop and measuring the contact angle each time until it reached a minimum and reproducible value.

Three-phase contact lines of water on macroporous polystyrene films (prepared on microscope cover glasses) were observed under an inverted optical microscope (Olympus IX70 Inverted, 100× oil objective). With a drop of water on top, films were illuminated from the bottom and reflection images were obtained via a color CCD camera (Cooke Co.). For better imaging, a small amount of Fluorescein dye was added to the water and fluorescence images were taken. A mercury arc lamp with blue excitation (~ 440 nm) was used for illumination.

6.3 Results and Discussion

6.3.1 Structure-induced Large Contact Angles

Our measurements show that water contact angles of the cast macroporous polystyrene films are much larger than those of the flat, solid films, and further increase

when the tops of the macroporous films are peeled off (see Figure 6.4 and Table 6.1). As described above, the wetting behavior of a liquid on a rough surface depends not only on the intrinsic wetting properties of the material (i.e., wettability of the flat surface) but also on the morphology of the surface. The geometric factors (r, f_s) of our films are listed in Table 6.1, which are calculated as follows.

$$f_{air} = \frac{\text{opening area of pores}}{\text{total projected area}} = \frac{\pi a^2}{6R^2/\sqrt{3}}, \tag{6.5}$$

$$f_s = 1 - f_{air}, \tag{6.6}$$

r = (total solid-water interfacial area)/(total projected area)

$$= \frac{\text{surface area of pore} + \text{flat surface area between pores}}{\text{total projected area}}$$

$$= \frac{\text{surface area of pores}}{\text{opening area of pores}} \times \frac{\text{opening area of pores}}{\text{total projected area}} + f_s$$

$$= \frac{2\pi R^2(1+\sin\varphi)}{\pi a^2} \times f_{air} + f_s, \tag{6.7}$$

$$\sin\varphi = \sqrt{1-(\frac{a}{R})^2}\ , \tag{6.8}$$

where, R and a are respectively the radii of the pores and of the top opening of the pores (Figure 6.5), which can be directly measured from the microscopic images of the films. In the case of top-peeled films, we made an assumption that the surfaces are composed of close-packed hemispherical air pores, so that a equals R, then r and f_s are independent of a (or R). The values of r and f_s of real surfaces of top-peeled films should be slightly different from the estimated values because two pores in contact are in fact connected by

a small hole in our macroporous films, and because the simple process of peeling-off by a Scotch tape brings non-uniformity (defects) across the top-peeled surface.

Comparing the calculated values of advancing contact angles (θ_a^c in Cassie's case and θ_a^w in Wenzel's case, calculated according to Eq. (6.2) and Eq. (6.3), respectively) with the experimental measurements (θ_a^m) listed in Table 6.1, we can see that the measured advancing contact angles are in good agreement with the calculated θ_a^c, both for the macroporous films as cast and for the top-peeled films. Therefore our system of water drops on macroporous films is in composite configuration (Cassie's scenario) during the advancing contact angle measurements, where water does not wet the pores and air is trapped inside instead. Thus, from flat surfaces to macroporous as-cast surfaces and further to top-peeled macroporous surfaces (Figure 6.4, column (a) to column (b) to column (c)), the fractions of air-water interfacial area ($f_{air} = 1 - f_s$) increase, leading to higher apparent water contact angles.

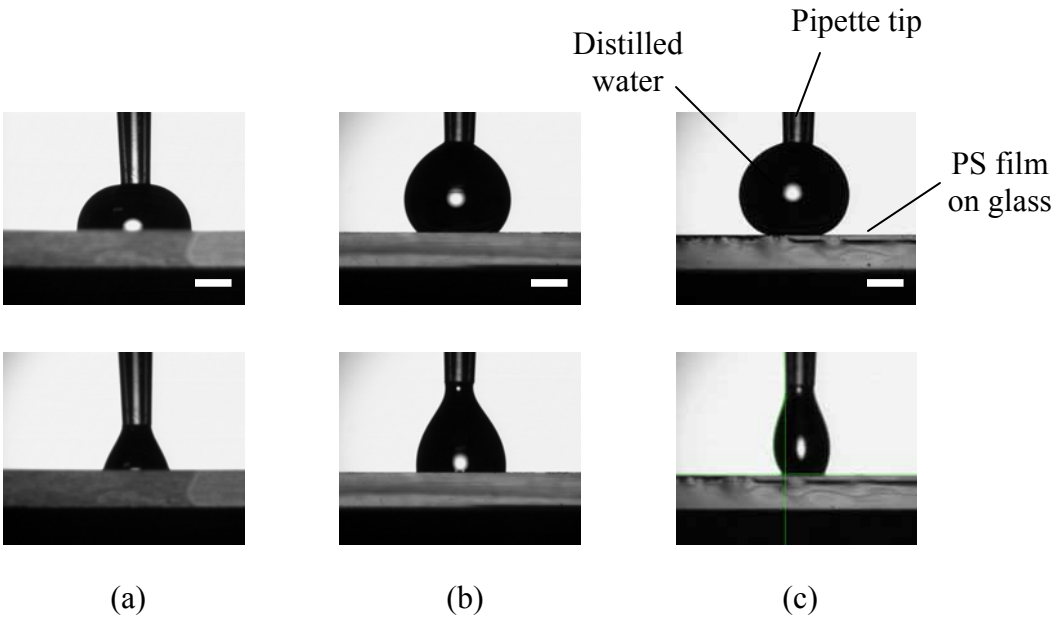

Figure 6.4 Increase of water contact angles with increase of fractions of water-air interfacial area underneath the water drops. Column (a), flat surface; Column (b), macroporous surface as cast (Figure 6.3a); Column (c), top-peeled macroporous surface (i.e., rough surface with closely-packed hemispherical pores) (Figure 6.3b). In each column, water is added into the sessile drop through the pipette tip (advancing contact angle measurement) in the top image, and withdrawn from the sessile drop through the pipette tip (receding contact angle measurement) in the bottom image. Measurements were done via a contact angle goniometer (Model 200, Ramè-Hart, Inc.) coupled with an automated dispenser. The films are made of polystyrene (mono-carboxyl terminated, M_w = 50,000). Scale bar: 1 mm.

Table 6.1 Comparison of measured water contact angles (θ^m) with calculated values (θ^c and θ^w according to Eq. (6.2) and Eq. (6.3), respectively) on structured polystyrene films. The geometric factors of the structured surfaces (r and f_s) are calculated from their optical images.

Surface	r	f_s	θ_a^m (deg)	θ_r^m (deg)	θ_a^w (deg)	θ_r^w (deg)	θ_a^c (deg)	θ_r^c (deg)
Flat	1	1	91	71	/	/	/	/
Macroporous as cast	3.1	0.35	132	95	93	0	131	122
Macroporous top-peeled	1.9	0.09	161	116	92	52	156	152

* Subscripts a represents the advancing angle and r the receding angle.
* Measurements were done via a contact angle goniometer (Model 200, Ramè-Hart, Inc.) coupled with an automated dispenser and the correspondent water-droplet profiles are shown in Figure 6.4.
* θ_a^m of the flat surface was used as θ^* in the calculation of θ_a^w and θ_a^c, while θ_r^m of the flat surface was used as θ^* in the calculation of θ_r^w and θ_r^c.

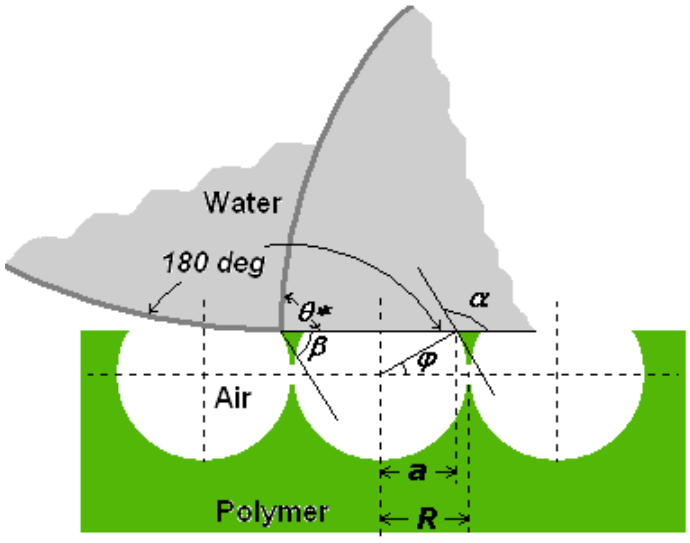

Figure 6.5 Schematic of a drop of water at the sharp edge of a macroporous film as cast. Angle α is the slope angle in Eq. (6.9), and β the edge angle in Eq. (6.10). The apparent contact angle θ at the edge can vary from θ^* to (180° - β + θ^*).

Here, the contact angle of water on a flat polystyrene film is worthy of mentioning. In our measurements, although the advancing angles can be above 90° (91° in average) when suddenly adding water into the sessile drop, it reduced to around 87° right after. According to the literature, the equilibrium advancing contact angle is 91° by Ellison and Zisman [18] and 86° by Craig et al. [19]. Here we used θ^* = 91° in the calculation of θ_a^w and θ_a^c. Comparing with the other four surfaces with controlled designs mentioned in the introduction part, our structured surface has the smallest intrinsic contact angle of water (Young's contact angle on a flat surface) — θ_a^* is fluctuating around 90° (87° ~ 91°) and θ_r^* is around 70°; all of the other four surfaces were chemically modified to render their intrinsic contact angles above 100° or even above 110° (θ_a^*/θ_r^* = 118°/100° in Bico et al.'s case [7]; θ_a^*/θ_r^* = 107°/102°, θ_a^*/θ_r^* = 102°/94°, and θ_a^*/θ_r^* = 119°/110° in Öner et al.'s three surfaces [8]; θ^* = 107° by Nakae et al. [9] and θ^* = 114° by Shiu, J. et al. [10]). However, the apparent water contact angles of our macroporous films are quite high. The increase of contact angle (contact angle differences between rough surfaces and flat surface) is more than 40° for macroporous as-cast films and around 70° for top-peeled films.

Generally, it is agreed that, for air to be trapped underneath the liquid drop on a rough surface, the roughness needs to be steep and deep enough [17,20]. As pointed out by Johnson and Dettre [17], it is geometrically possible for the system of a sessile drop on a rough surface to form a composite configuration as long as there is a local slope of the rough surface, α, satisfying

$$\theta^* = 180° - |\alpha|. \tag{6.9}$$

Further, their numerical calculations of an idealized sinusoidal surface showed that, for very deep troughs, the composite configuration was also energetically favorable — free energy of the system was lower when air was trapped under the drop. In reality, for most rough surfaces, the maximum local slope ($|\alpha_{max}|$) is less than 90°, so that the intrinsic contact angle (θ^*) of the material has to be larger than 90° [14]. In our case, for the macroporours surfaces as cast, because the pores are in the shape of a large segment of a sphere, $|\alpha_{max}|$ is larger than 90° (around 122° at the top opening and decreases gradually with height, see Figure 6.5), Eq. (6.9) is satisfied when the intrinsic contact angle is larger than 58°. For the top-peeled macroporous surfaces, $|\alpha_{max}|$ is around 90°, with θ_a^* fluctuating around 90° (87° ~ 91°), both a composite configuration and a non-composite configuration are possible if we only consider Eq. (6.9). However, for freshly peeled surfaces, there are many sharp edges which can lead to air trapping.

Edge effect on spreading of liquid has been studied in detail by Mason's group [21,22]. Their experiments confirmed the Gibbs inequality condition [22] — the apparent contact angle θ at the edge can vary from θ^* to (180° - β + θ^*)

$$\theta^* \leq \theta \leq \theta^* + 180° - \beta \tag{6.10}$$

where, β is the angle between the two surfaces of the edge ($\beta < 180°$). Here, β is around 58° for the macroporours surfaces as cast, so that the contact line at the edge can be stabilized with a contact angle as high as 180°. Because the size of water drops used in our measurements (R < 2 mm) is less than the capillary length of water (κ^{-1} ~ 2.7 mm), deformation of drop shape due to gravity can be neglected. Thus, we are in the case A regime described in Ref. [21], so that water surface just spans the opening of air pores with air trapped inside. For the top-peeled macroporous surfaces, there should be many

sharp edges which are less than 90° due to the breakage, resulting in air-trapping. This is in agreement with the experimental observation. In general, water drops showed very large apparent contact angles and were unstable on freshly peeled surfaces; while after several cycles of depositing and withdrawing of water drops, sharp edges were blunted so that the apparent contact angle decreased and residue of water was seen left on the surfaces when removing the sessile drop by an absorbing paper.

Comparing the measured values of receding contact angle (θ_r^m) with the calculated ones (θ_r^w and θ_r^c), however, we can see that the measured receding contact angles are not predicted by either of the equations (Wenzel's and Cassie's) — the calculated values are much larger than those predicted by Wenzel's equation and smaller than those by Cassie's equation. It is generally found that receding contact angles are hard to explain and predict. Contact line can be easily pinned by a defect on the surface, especially on a rough surface with many sharp edges. For the air-solid composite surface during advancing, water may retain in the roughness during receding. Further, according to the non-slip assumption in fluid mechanics, there should be a thin layer of liquid left on the solid [23].

6.3.2 Large Hysteresis

It is agreed that [3,24], contact angle as described by Young's equation is for ideal surfaces: chemically homogeneous, rigid, and flat at an atomic scale. In reality, contact angle hysteresis, H, defined as the difference between θ_a and θ_r, always exists, due to chemical heterogeneity and roughness. For our films made of polystyrene, the hysteresis of water contact angles is around 20° for flat surfaces and 40° (macroporous films as cast)

or even higher (top-peeled macroporous films) for rough surfaces. The hysteresis of flat polystyrene films we measured is similar to the experimental data reported by Ellison and Zisman (θ_a*/θ_r* = 91°/71.6°) [18] and by Craig et al. (θ_a*/θ_r* = 86°/64°) [19]. Here, such large hysteresis of our macroporous films is also due to the roughness, which is well-known for inducing hysteresis. By analyzing an idealized rough surface numerically, Johnson and Dettre [17] have shown that roughness induces a large amount of metastable states which are separated by energy barriers. A liquid drop in different contact angles can be easily stabilized in local energy minima during advancing or receding, which results in hysteresis. Also, sharp edges pin contact lines, which further increase the hysteresis for top-peeled films.

As pointed out by Öner et al. [8], it is the hysteresis not the absolute values of the contact angles that is important to hydrophobicity. This is from the consideration that large hysteresis will make water drops stick on a surface even when the surface is inclined at a high angle. By balancing the capillary force and the gravity force on a liquid drop on a tilted surface, it can be derived [25] that

$$mg \sin\phi / w = \gamma_{LV} (\cos\theta_r - \cos\theta_a) \tag{6.11}$$

where, m is the mass of the drop, g is the gravitational acceleration, ϕ is the minimum tilting angle of the surface to produce sliding of the drop and w is the width of the drop perpendicular to the direction of sliding motion. By approximation of a spherical non-wetting drop, $m \approx (4/3)\pi R^3 \rho$, where R is the radius of the spherical drop and ρ is the liquid density. Substituting $m = (4/3)\pi R^3 \rho$ into Eq. (6.11) and rearranging it lead to

$$R^2 (4\pi R/3w) \sin\phi = (\gamma_{LV}/\rho g) (\cos\theta_r - \cos\theta_a) \tag{6.12a}$$

$$(4\pi R/3w) \sin\phi = (\kappa^{-1}/R)^2 (\cos\theta_r - \cos\theta_a) \tag{6.12b}$$

where, $(\gamma_{LV}/\rho g)^{1/2}$ is equal to capillary length κ^{-1} by definition [26]. Thus, for small drops ($R < \kappa^{-1}$), sticking can easily happen on a surface with large hysteresis resulting in large value of ($\cos\theta_r - \cos\theta_a$). This is also observed in our case. Tiny water drops can stick to the surface of the macroporous films even with the films upside down. However, when the size of the water drops is larger than the capillary length (> 2.7 mm), they can easily move off the surfaces when tilted.

6.3.3 Observation of Microscopic Contact Line

Contact line is the line where three phases (water drop, solid surface and air) meet. It is also a disputable subject in the research area of wetting. Many studies have been done both theoretically and experimentally, but it is still not well understood. Here we do not want to worry about the effect of line tension since the size of the drops we used were on the order of millimeter [15]. It was argued that contact lines on rough surfaces are different (continuous or discontinuous [7]) depending on the surface topology when liquid drops adopt composite configuration. It was found that discontinuous contact lines destabilized water drops so that they easily rolled off those surfaces when the surfaces were slightly tilted [7]. Here, solid surfaces are continuous for the macroporous films as cast and discontinuous for the top-peeled films (Figure 6.3). Also, as pointed out by Quéré [15], in the composite configurations, there should be many pieces of liquid-air (in the case of continuous solid surfaces) or liquid-solid (in the case of continuous air surfaces) interfaces and three-phase contact lines under the sessile drop. Thus, it would be interesting if we can look at how the contact lines and the interfaces arrange themselves below the liquid drop. Since amorphous polystyrene is transparent (surface

roughness may induce scattering, making it opaque), we were trying to look at the contact lines from the bottom of the films with sessile drops on top by an inverted optical microscope (Figure 6.6). It would be interesting if we can use confocal technology to focus on the interface between the sessile drop and rough surface.

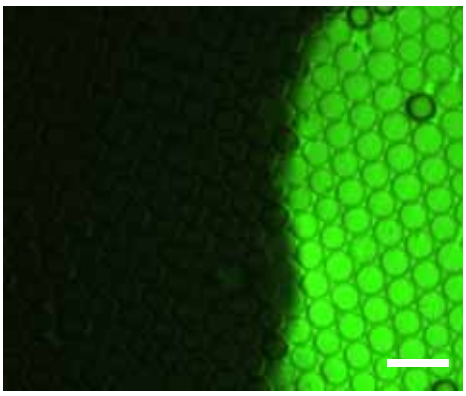

Figure 6.6 Bottom view of a macroporous polystyrene film with a drop of water residing on the top, imaged by an inverted fluorescence microscope (Olympus IX70 Inverted, 100× oil objective). A small amount of fluorescein was added into water for imaging. The bright region is with a water drop residing on the top of the film and the border between the bright part and the dark is the three-phase contact line. Scale bar: 10 μm.

6.3.4 Temperature Effect

When we were looking at the contact lines of the system by an optical microscope, we found that water spread into the micron pores when we moved the macroporous film to find areas of interest. This spreading was done pore by pore and only took place after that area was moved into the viewing field. We suspected that it was due to the local heating by the illumination. Surface tension of water decreases with temperature so that the intrinsic contact angle of hot water on polystyrene decrease, which induces a

transition from composite configuration (Cassie's case) to wet configuration (Wenzel's case). Also, hot water has higher vibrational energy so that water can overcome the energy barriers to fill the pores [17]. To confirm this, we did a simple experiment by looking at the contact angles of hot water on our films (Fig. 6.7). The temperature of the water was 90°C in the reservoir, but after several experiment procedures (withdrawing water into syringe and depositing it onto films, focusing the drop) the temperature should be lower than 90°C. The results showed that although the contact angle of hot water on flat polystyrene surface was only lowered around 10°, the contact angle of hot water on macroporous surface was lowered more than 60°, a transition from apparent hydrophobic to apparent hydrophilic. In the hot water case, roughness of surface lowered the contact angle, which qualitatively showed that the system were in the Wenzel's regime. Applying Wenzel's equation, i.e., Eq. (6.3), the calculated value is 61° matching the measured value of 66° quite well, which further confirmed our conjecture — water filled the roughness.

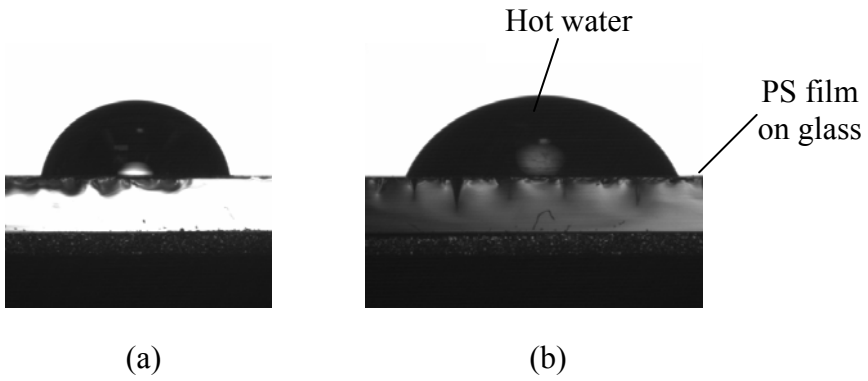

Figure 6.7 A drop of hot water on (a) a flat polystyrene film and (b) a macroporous as-cast polystyrene film. The static contact angles are (a) 81° and (b) 66°, respectively. The measurements were done via a contact angle goniometer (Model 200, Ramè-Hart, Inc.) coupled with an automated dispenser. Scale bar: 1 mm.

6.4 Conclusions

To conclude, we have investigated the wetting properties of water on macroporous polystyrene films with closely packed, spherical pores open on the surfaces. It was found that the advancing water contact angles were increased by more than 40° for macroporous polystyrene films as cast and around 70° for top-peeled films, compared with those for flat polystyrene films. These structured films also showed increased contact angle hysteresis, which was ascribed to the effects of roughness and sharp edges. It was found that local heating due to the illumination can reduce the surface tension of water so that the pores were filled with water locally. It was proved by putting a drop of hot water on a macroporous film which adopted a contact angle matching Wenzel's equation.

This kind of lotus-effect surfaces might be used as car surfaces which also show brilliant color. However, the microstructures on the surfaces of the polystyrene films are fragile. For application, more processes such as crosslinking are required to make the structures more stable (mechanically strong and solvent-resistant).

References:

[1] P. G. de Gennes, "Wetting: statics and dynamics", *Rev. Mod. Phys.* **57**, 827 (1985).

[2] H. Song, J. D. Tice and R. F. Ismagilov, "A microfluidic system for controlling reaction networks in time", *Angew. Chem. Int. Ed.* **42**, 768 (2003).

[3] T. Wagner, C. Neinhuis and W. Barthlott, "Wettability and contaminability of insect wings as a surface of their surface sculptures", *Acta Zool.* **77**, 213 (1996).

[4] W. Barthlott and C. Neinhuis, "Purity of the sacred lotus, or escape from contamination in biological surfaces", *Planta* **202**, 1 (1997).

[5] A. Marmur, "The lotus effect: superhydrophobicity and metastability", *Langmuir* **20**, 3517 (2004).

[6] Z. Z. Gu, H. Uetsuka, K. Takahashi, R. Nakajima, H. Onishi, A. Fujishima and O. Sato, "Structural color and the lotus effect", *Angew. Chem. Int. Ed.* **42**, 894 (2003).

[7] J. Bico, C. Marzolin and D. Quéré, "Pearl drops", *Europhys. Lett.* **47**, 220 (1999).

[8] D. Öner and T. J. McCarthy, "Ultrahydrophobic surfaces. Effects of topography length scales on wettability", *Langmuir* **16**, 7777 (2000).

[9] H. Nakae, R. Inui, Y. Hirata and H. Saito, "Effects of surface roughness on wettability", *Acta Mater.* **46**, 2313 (1998).

[10] J. Shiu, C. Kuo, P. Chen and C. Mou, "Fabrication of tunable superhydrophobic surfaces by nanosphere lithography", *Chem. Mater.* **16**, 561 (2004).

[11] T. Nishikawa, J. Nishida, R. Ookura, S. I. Nishimura, S. Wada, T. Karino and M. Shimomura, "Honeycomb-patterned thin films of amphiphilic polymers as cell culture substrates", *Mater. Sci. Eng. C* **8-9**, 495 (1999).

[12] T. Nishikawa, J. Nishida, R. Ookura, S. I. Nishimura, S. Wada, T. Karino and M. Shimomura, "Mesoscopic patterning of cell adhesive substrates as novel biofunctional interfaces", *Mater. Sci. Eng. C* **10**, 141 (1999).

[13] See, e.g., R. J. Good, "Contact angle, wetting, and adhesion: a critical review", in *Contact angle, wettability and adhension*, edited by Mittal, K. L. (VSP: Utrecht, The Netherlands), 1993, p3.

[14] D. Quéré, "Rough ideas on wetting", *Physica A* **313**, 32 (2002).

[15] A. B. D. Cassie, and S. Baxter, "Wettability of porous surfaces", *Trans. Faraday Soc.* **40**, 546 (1944).

[16] R. N. Wenzel, "Resistance of solid surfaces to wetting by water", *Ind. Eng. Chem.* **28**, 988 (1936).

[17] R. E., Jr. Johnson and R. H. Dettre, "Contact angle hysteresis 1. Study of an idealized rough surface", *Advan. Chem. Ser.* **43**, 112 (1963).

[18] A. H. Ellison and W. A. Zisman, "Wettability studies of nylon, polyethylene terephthalate and polystyrene", *J. Phys. Chem.* **58**, 503 (1954).

[19] R. G. Craig, G. C. Berry and F. A. Peyton, "Wetting of poly-(methyl methacrylate) and polystyrene by water and saliva", *J. Phys. Chem.* **64**, 541 (1960).

[20] S. Herminghaus, “Roughness-induced non-wetting”, *Europhys. Lett.* **52**, 165 (2000).

[21] J. F. Oliver, C. Huh and S. G. Mason, “Resistance to spreading of liquids by sharp edges", *J. Colloid Interface Sci.* **59**, 568 (1977).

[22] Y. H. Mori, T. G. M. van de Ven and S. G. Mason, “Resistance to spreading of liquids by sharp edged microsteps”, *Colloid Surf.* **4**, 1 (1982).

[23] N. A. Patankar, “On the modeling of hydrophobic contact angles on rough surfaces”, *Langmuir* **19**, 1249 (2003).

[24] J. F. Joanny and P. G. de Gennes, “A model for contact angle hysteresis”, *J. Chem. Phys.* **81**, 552 (1984).

[25] See, e.g., C. G. L. Furmidge, “Studies at phase interfaces 1. The sliding of liquid drops on solid surfaces and a theory for spray retention”, *J. Colloid Sci.* **17**, 309 (1962).

[26] D. Richard and D. Quéré, “Viscous drops rolling on a tilted non-wettable solid”, *Europhys. Lett.* **48**, 286 (1999).

CHAPTER 7

STABLIZING STRUCTURES BY CROSSLINK

As discussed in the introduction chapter, many applications have been proposed for this kind of macroporous, honeycomb-like film. For these applications to be realized, very often, the films are required to have good mechanical properties and solvent stability. For the films prepared by this casting method, however, many of them are very brittle and easily dissolved by organic solvents. To improve their properties, one way is to crosslink (via UV, e-beam or heat) these polymer films. Yabu et al. [1] have prepared macroporous polyimide films by first casting films from polyion-complexed polyamic acid in moisture and then converting them into polyimide films by chemical treatment. We have started to exploit this crosslinking method and, here, I will focus on the crosslinked films by heat. By adjusting the heating temperature, we were able to tune the porous structure to prepare “Pico- to femto-liter beakers”, which are of practical interest for small-quantity analysis [2].

7.1 Experiments

Ordered macroporous films of azidePPE prepared as described in Chapter 2 were heated from room temperature (~ 25 °C) to 300 °C at a speed of 5 °C per minute (with the temperature held for several minutes at ~ 180 °C) and then cooled down to room temperature in air. A microscope hot stage (LINKAM TMS90/THM 600) was used to control the heating process and the morphology of the film upon heating was monitored via a polarized optical microscope (Leica DMRX) coupled with a long-working-distance

objective (50× 0.5 L dry). 3D structures of the processed films (heated to 300 °C and then cooled down to room temperature) were then imaged via a laser scanning confocal microscope (Leica TCS SP, 100× 1.4 oil objective). To test their solvent stability, the processed films were soaked in different organic solvent such as carbon disulfide and chloroform for 30 minutes and then checked by the LSCM again.

7.2 Results

Comparing the structure of an azidePPE film as cast (Figures 7.1a and 7.1c) with that of a thermally crosslinked one (Figures 7.1b and 7.1d), the shape change of the air bubbles in the azidePPE film upon heating can be clearly seen — from spherical layers to cone-like segments. Accompanying that, the height of the pores decreased (i.e., the thickness of the film decreased) and the interconnecting holes between neighbor pores disappeared.

After a heated film was placed in an organic solvent such as carbon disulfide (the solvent used to prepare the original azidePPE films) and chloroform (unheated azidePPE films can be dissolved in chloroform) for a while (~ 30 min), no obvious change of the cone-like structure of the film was seen from its LSCM images.

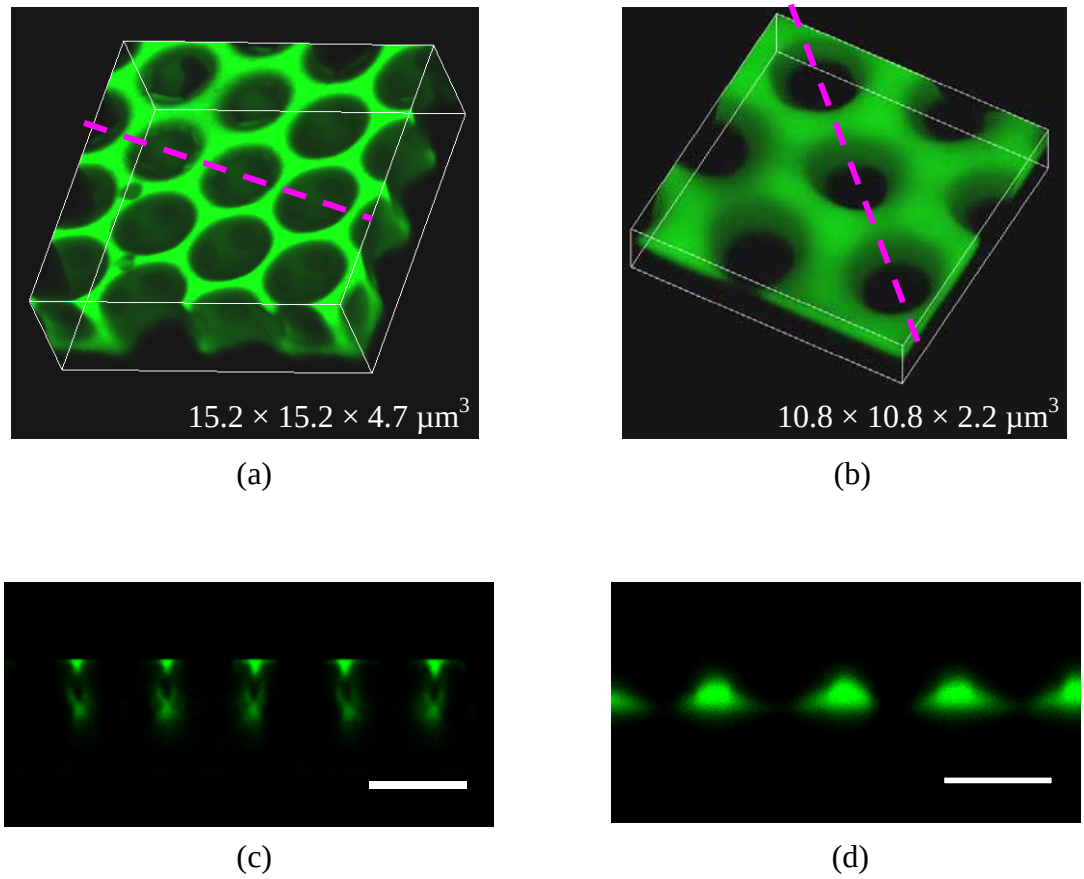

Figure 7.1 Microscopic images of azidePPE films. (a) 3D view of a film as cast. (b) 3D view of a similar film after crosslinked by heating. (c) Cross-sectional view of a film as cast. (d) Cross-sectional view of a similar film after crosslinked by heating. All images are by a laser scanning confocal microscope (Leica TCS SP, 100× 1.4 oil objective). The cross-sections are optically sectioned along the direction marked by red dashed lines on the correspondent 3D images. The size of each 3D cube is marked on the image. Scale bar: 5 μm.

7.3 Discussion

As discussed in Ref. 2, the azide groups in the side chains of azidePPE (the chemical structure of azidePPE is given in Figure 2.3 in Chapter 2) are expected to react via multiple cycloadditions ("3+2") at high temperatures [2] and IR measurements of the unheated and heated azidePPE films showed that the peak corresponding to the azide groups almost disappeared after heated to 300 °C [2]. Combining with the fact that the heated films did not dissolve in carbon disulfide and chloroform any more, it is reasonable to conclude that the heated films have been crosslinked.

When we heated the macroporous films at a higher heating rate or without holding temperature for several minutes at about 160 °C to 200 °C, only featureless films were obtained. Furthermore, it was found that the remained porous structures were affected by the detailed heating procedures; a slower heating rate, a longer holding period and a lower final heating temperature (i.e., heated to a temperature somewhat below 300 °C) led to a more remained structure. Therefore, the remained structures upon heating are the result of the competition between crosslinking (which try to keep the porous structure as it is) and the softening (from a glassy solid to a rubbery liquid) of the azidePPE. When in the liquid state at high temperatures, the original porous structures relaxed (because of the fast evaporation, there should be residue stress in the films) and flattened (rubbery flow due to gravity) slowly because of the high viscosity of the liquid semi-rigid polymer. The images of heated films in Figures 7.1b and 7.1d clearly show the smoothing-out of the sharp edges in the unheated films (Figures 7.1a and 7.1c).

7.4 Conclusions

In conclusion, we have used a simple heating method to crosslink macroporous azidePPE films and it was found that the final structures can be tuned by adjusting the detailed heating profiles, based on the competition between the crosslinking and the softening of the polymer upon heating. These crosslinked films with cone-like structures are promising for the applications in small-quantity analysis.

References:

[1] H. Yabu, M. Tanaka, K. Ijiro and M. Shimomura, "Preparation of honeycomb-patterned polyamide films by self-organization", *Langmuir* **19**, 6297 (2003).

[2] B. Erdogan, L. Song, J. N. Wilson, J. O. Park, M. Srinivasarao and U. H. F. Bunz, "Permanent bubble arrays from a cross-linked poly(para-phenoleneethynylene): picoliter holes without microfabrication", *J. Am. Chem. Soc* **126**, 3678 (2004).

APPENDIX

CALCULATION OF ORIENTATIONAL CORRELATION FUNCTION

The following programs were written for the calculation of bond-orientational correlation function (see Chapter 3) using Matlab. The values of the bar_length, the Tol, and the bond_length need to be adjusted according to the feature of the samples.

A.1 Calculation of Bond Positions and Bond Angles

```
bar_length = 1.6;

Length = length(data);
Cal_Data = [];

for i = 1:Length-1
   temp_dist = sqrt((data(i,1)-data(i+1:end,1)).^2+(data(i,2)-data(i+1:end,2)).^2);
   I = find(temp_dist <= bar_length);

   temp1 = data(I+i,:);
   A = ones(length(I),2);
   A(:,1) = A(:,1)*data(i,1);
   A(:,2) = A(:,2)*data(i,2);

   center = (A+temp1)/2;

   temp2 = temp1(:,1) - data(i,1);
   I = find(temp2 = 0);
   Angle = atan((temp1(:,2) - data(i,2))./(temp1(:,1) - data(i,1)));
   Agnle(I) = 90*pi/180;
   x = [Angle center];
   Cal_Data = [Cal_Data; x];
end

Length = length(Cal_Data);
Pt_data = Cal_Data(:,2:3);
Angle_data = Cal_Data(:,1);
```

A.2 Calculation of Bond-Orientational Correlation Function

```
Length = length(data);
Pt_data = data(:,2:3);
Angle_data = data(:,1);

for i = 1:Length

   Ref = Pt_data(i,:);
   temp{i} = sqrt((Ref(1)-Pt_data(:,1)).^2+(Ref(2)-Pt_data(:,2)).^2);
   [Dist{i},I] = sort(temp{i});
   Angle{i} = Angle_data(I);
end

Tol = 0.2;

bond_length = 3.75;

for j = 1:40
   num_target(i) = 0;
   sum_target(i)= 0;
 for i = 1:length(Dist)

   I = find(Dist{i} >=j*bond_length-Tol &  Dist{i}<=j*bond_length+Tol);
   num_target(j) = num_target(j) + length(I);
   temp{i} = abs(cos(6*(Angle{i}(I)-Angle{i}(1))));
   sum_target(j) = sum_target(j) + sum(temp{i});
end
   A(j) = sum_target(j)./num_target(j);
end

plot (A, 'rx')
```